

Reactive collisions with conformationally controlled molecules

Inauguraldissertation

zur

Erlangung der Würde eines Doktors der Philosophie

vorgelegt der

Philosophisch-Naturwissenschaftlichen Fakultät

der Universität Basel

von

Daniel Rösch

aus

Lörrach, Deutschland

Basel, 2016

Originaldokument gespeichert auf dem Dokumentenserver der Universität Basel

edoc.unibas.ch

Genehmigt von der Philosophisch-Naturwissenschaftlichen Fakultät
auf Antrag von

Prof. Dr. Stefan Willitsch und Prof. Dr. Markus Meuwly.

Basel, den 21. Juni 2016

Prof. Dr. Jörg Schibler
Dekan

Abstract

A new method to study conformer-specific effects in gas-phase ion-molecule reactions was developed. The *cis*- and *trans*-conformers of 3-aminophenol were spatially separated in a molecular beam and reacted with a Coulomb crystal of laser cooled Ca^+ ions. The reaction of the *cis*-conformer was found to be twice as fast as the reaction of the *trans*-conformer. The difference in the rates could be explained by differences in the long-range ion-dipole interaction potential and the results of adiabatic-capture-theory calculations agreed well with the experiment.

A new experimental apparatus dedicated to conformer-specific ion-molecule experiments was designed and characterised. The new apparatus incorporates a time-of-flight mass spectrometer coupled to a linear quadrupole ion trap. The new mass spectrometer performs well and enables high resolution mass spectra of the trapped ions. The molecular beam machine in the new apparatus was tested and characterised by measuring OCS deflection profiles. A theoretical feasibility study for rotationally quantum-state selected ion-molecule reactions was performed and a new experiment was suggested and simulated.

Acknowledgements

If I have seen further it is by standing on the shoulders of giants.

Isaac Newton, 1676

This thesis would not exist without the help and contributions of many great people. I am grateful I had the chance to work with and learn from every single one of them.

I first want to acknowledge Stefan Willitsch for giving me the opportunity to work on this extremely exciting project. His counsel and guidance was highly appreciated and I am grateful for the friendly working atmosphere and the fact that his office door was always open for me.

I would like to gratefully acknowledge the fruitful collaboration with Jochen Küpper and Yuan-Pin Chang. Yuan-Pin did the analysis and fitting of the 3-aminophenol experimental data, as well as simulations of deflection curves of 3-aminophenol. He also determined the 3-aminophenol density in the molecular beam and measured and analysed the dependence of the reaction rate constant on the Ca^+ electronic state. I enjoyed the time I spent in Hamburg very much and am very thankful for this great experience.

I want to acknowledge the contributions of Hong Gao and Ardita Kilaj. Hong helped with the setup of the new apparatus and together with Ardita helped in the data acquisition of the TOF-MS characterization. All experimental data of chapter 4 were acquired and analysed by Hong and Ardita.

I would like to acknowledge the contributions of the Master and project students that were involved in this project. Mikko Johannes Väärämäki did Simion simulations on ion extraction from a quadrupol ion trap, which acted as a basis for the development of the new ion trap. Dominik Hass helped in setting up the ion trap chamber and the laser cooling.

I would like to acknowledge the great work of the mechanical workshop. Only the high precision and reliability of every mechanical part they provided made the success of this project possible. Thanks to Dieter Wild, Grischa Martin, Philip Knöpfel and Simon Rufener.

I would like to acknowledge the help of Georg Holderied with all the electronics involved in the experiment. I also want to acknowledge help with electronics from Andreas Tonin. I want to thank Anatoly Johnson for assistance with lasers.

I would like to acknowledge Xin Tong and Felix Hall for teaching me the art of ion trapping and laser cooling.

I want to thank all members of the group for a lot of useful discussions and also a lot of fun. I enjoyed the time with all of you.

I would like to thank Markus Meuwly for kindly agreeing to co-examine my thesis.

I would like to gratefully acknowledge funding for this project from Swiss National Science Foundation grant numbers PP00P2_140834 and BSCGI0_157874, European Commission under the Seventh Framework Programme FP7 GA 607491 COMIQ, the University of Basel and the excellence cluster “The Hamburg Center for Ultrafast Imaging – Structure, Dynamics and Control of Matter at the Atomic Scale” of the Deutsche Forschungsgemeinschaft.

Finally, I want to thank Deborah for all her love, support and encouragement. The happiness provided at home by her and our great son Linus Paul enabled

me to fully focus on this project.

Contents

1	Introduction and concepts	1
1.1	Introduction	1
1.2	Controlling and manipulating molecular beams	2
1.2.1	Generation of cold molecular beams	3
1.2.2	Field free rotating molecules	4
1.2.2.1	Linear top	5
1.2.2.2	Symmetric top	5
1.2.2.3	Asymmetric top	6
1.2.3	Molecules in electric fields	7
1.2.3.1	Stark Effect	7
1.2.3.2	Deceleration and Deflection	8
1.3	Ion trapping and laser cooling	9
1.3.1	Laser cooling	12
1.3.2	Molecular dynamics simulations	14
1.4	Ion - molecule reactions	15
1.4.1	Adiabatic dipole capture theory	16
1.4.2	Monte-Carlo trajectory simulations	18
1.5	Mass spectrometry	19
1.5.1	Resonant excitation mass spectrometry	20
1.5.2	Time of flight mass spectrometry	20
2	Reactions of spatially separated conformers of 3-Aminophenol with Ca⁺	24
2.1	Introduction	24

CONTENTS

2.2	Experimental Setup	25
2.2.1	Conformer deflection setup	25
2.2.2	Ion trap setup	27
2.2.3	Reaction rate measurements	28
2.2.4	Mass spectrometry of trapped ions	29
2.2.5	Molecular beam profile measurements	30
2.3	Theoretical and computational methods	30
2.3.1	DFT calculations of reaction paths on the ground-state potential energy surface	30
2.3.2	Adiabatic capture theory	31
2.3.3	Molecular-dynamics simulations of Coulomb crystals	32
2.3.4	Monte-Carlo simulations of molecular beam profiles	32
2.4	Experimental Results	34
2.4.1	Deflection curves of 3AP	34
2.4.2	Number density of 3AP	36
2.4.3	Reaction profiles and conformer-specific rate constants of $\text{Ca}^+ + 3\text{AP}$	37
2.4.4	Variation of Ca^+ electronic state populations	39
2.4.5	Mass spectra of reaction products	40
2.5	Reaction mechanisms and kinetics	41
2.5.1	Reaction pathways on the ground-state potential energy surface	41
2.5.2	Capture dynamics in the $\text{Ca}^+ (4p) + 3\text{AP}$ excited channel	44
2.6	Summary and conclusions	46
3	A new setup for conformer dependent ion-molecule reactions with an ion trap coupled to a time-of-flight mass spectrometer	48
3.1	Introduction	48
3.2	TOF experiments with trapping RF turned off during ion ejection	50
3.2.1	Experimental setup	50
3.2.2	Experimental results and discussion	53
3.3	TOF experiments with trapping RF turned on during ion ejection	63
3.3.1	Experimental setup	64

3.3.2	Experimental results and discussion	65
3.3.2.1	Ion extraction dynamics	70
3.3.2.2	Post-ejection-acceleration using a lift-TOF-MS	76
3.4	Summary	82
4	Rotationally state selected ion-molecule reactions	84
4.1	Introduction	84
4.2	Experimental setup	86
4.3	Results and discussion	88
4.3.1	Measurement of OCS deflection profiles	88
4.3.2	Estimation of OCS density in the molecular beam	92
4.3.3	Theoretical investigation of rotational state specific capture rates	94
4.4	Summary	99
5	Outlook and Summary	101
	Bibliography	103

Chapter 1

Introduction and concepts

1.1 Introduction

Most molecules possess several different conformations, these are rotational structural isomers that can easily interconvert into each other, provided, there is enough energy available to overcome the energy barrier of bond rotation. With increasing molecule size, the number of possible conformations increases rapidly. For example, a short peptide consisting of 7 amino acids can already have on the order of 7^{12} energetically accessible conformations since the backbone torsion angles of each amino acid can be in one of 11 to 12 specific states [1]. Different conformations can exhibit different chemical reactivities [2–4], and to fully understand the chemistry and reactivity of molecules it is necessary to investigate their conformer-specific reactivities. While it is certainly impossible at the moment to investigate the conformationally resolved chemical reactivity of such a peptide, a few methods have been developed to study conformeric effects of simple systems.

Conformer-specific spectroscopy studies have been done in the gas phase and cryogenic matrices for several molecules [5–15]. Photoinduced interconversions of one conformer into another can be used to study conformational dynamics and act as a probe for the landscape of the underlying potential energy surface [16–19]. Conformational effects in photodissociation of cations and neutral small organic molecules have been observed [20–25]. So far, only little data is

1. Introduction and concepts

available on conformational effects in bimolecular reactions. The Criegee intermediate CH_3CHOO has two conformations with substantial different reaction rates with water or SO_2 . Criegee intermediates are formed from ozonolysis of organic compounds and play an important role in atmospheric chemistry [26]. Conformer-dependent reactions have also been observed for formic acid embedded in a cryogenic matrix reacting with oxygen atoms [27].

This work presents a novel method to study bimolecular reaction rates of molecules in selected conformational states with cold ions. An apparatus was built to spatially separate different conformers in a molecular beam and study their reactions with a stationary target of laser cooled ions in an ion trap.

The outline of this work is as follows: This introduction gives an overview over the concepts and methods used in this work. In chapter 2, experimental and theoretical results of the conformer-dependent reaction of 3-aminophenol with Coulomb crystals of Ca^+ ions are given. Chapter 3 describes the setup and characterization of a new experiment that incorporates a novel time-of-flight mass spectrometer coupled to an ion trap. In chapter 4, the experimental validation of the molecular-beam machine in the new setup is presented, as well as a theoretical feasibility study of using this machine for rotationally state-resolved ion-molecule reactions. A short outlook into possible future developments for conformer and rotationally state selected chemistry is given in chapter 5.

1.2 Controlling and manipulating molecular beams

To generate ensembles of molecules with a certain molecular conformation, one needs to "freeze" the conformation and suppress thermal conversion into other conformers through rotation around molecular bonds.

Molecular beams provide an efficient way of preparing internally cold molecules and have made possible exciting experiments in the realm of gas-phase chemical dynamics. For example, the low collision energies in the center of mass frame inside a molecular beam lead to the formation of weakly bound complexes [28]. High resolution spectroscopy gives an insight into the dynamics of such van der Waals complexes [29]. Crossed and merged molecular beam experiments en-

abled the study of collisions with very low collision energies, which rendered the observation of partial wave resonances possible [30–32].

In the following sections, cooling by supersonic expansion, the molecular rotational energy structure in the absence and presence of electric fields, and some experimental techniques to manipulate molecular beams with electric fields will be discussed.

1.2.1 Generation of cold molecular beams

In a supersonic expansion, a gas is expanded from a high pressure reservoir into vacuum through a small nozzle with a diameter much larger than the mean free path of the gas molecules in the reservoir. The escaping molecules experience many collisions during the expansion process. If the pressure in the reservoir is high, the gas flow can be treated as an adiabatic isentropic expansion [33]. This means that the sum of the molecular enthalpy and the kinetic energy is constant.

$$U_0 + p_0V_0 + \frac{1}{2}mv_0^2 = U_1 + p_1V_1 + \frac{1}{2}mv_1^2. \quad (1.1)$$

Here the indices 0 and 1 denote a quantity before and after the expansion. U is the internal energy, i.e., the sum of the translational, rotational and vibrational energy of the molecule, p is the pressure, V is the volume of the gas, m is the mass of the molecule and v is the velocity of the molecular beam. Since $p_0 \gg p_1$ and $V_0 \ll V_1$, the term $pV \approx 0$ before and after the expansion. The beam velocity in the source is $v_0 = 0$. Therefore, equation 1.1 can be rewritten as:

$$U_0 = U_1 + \frac{1}{2}mv_1^2, \quad (1.2)$$

from which it is immediately evident that the internal energy is reduced during the collisions in the expansion process and is converted into kinetic energy of the molecules traveling at supersonic velocities.

To "freeze" molecules in their conformation, they can be seeded in an atomic beam of a noble gas which results in the seeded molecules gaining the same velocity as the noble gas atoms and therefore very efficient cooling of their internal energy can be achieved. The beam is usually skimmed by small circular

1. Introduction and concepts

skimmers to separate the beam generation and detection regions. This is done to reduce the pressure in the detection vacuum chamber by differential pumping and for "transversal cooling" by cutting out only the central part of the beam. Several different molecular beam sources have been developed [34–36]. In the CRESU (cinétique de réactions en écoulement supersonique uniforme) technique a continuous, cold and uniform molecular beam is formed by a laval nozzle. The final velocity and temperature of the beam are determined by the shape of the nozzle [34]. Continuous molecular beams have certain disadvantages, mainly that they require very large and expensive vacuum pumps, since the beam quality is diminished if the background pressure is too high in the source chamber. Also, the skimmer positions have to be adjusted carefully to avoid barrel and Mach shock waves [36]. To reduce the required pumping capacity, several types of pulsed valves have been developed. In the experiments described in this work, a high temperature version of the Even-Lavie valve [36] and a cantilever piezovalve [35] have been used. Both valves can be operated at high repetition rates and generate short ($\sim 50 - 200 \mu\text{s}$), dense gas pulses. All molecules are in the vibrational ground state and only the lowest rotational quantum states are populated after the supersonic expansion. The rotational temperatures achieved in our experiments were around 1 K.

1.2.2 Field free rotating molecules

The rotational energy of a molecule in the absence of electric fields can be calculated by solving the Schrödinger equation:

$$\mathcal{H}_R \Psi_{JM}(\phi, \theta, \chi) = E \Psi_{JM}(\phi, \theta, \chi). \quad (1.3)$$

The Hamiltonian for a rigid rotor is:

$$\mathcal{H}_R = \frac{J_a^2}{2I_a} + \frac{J_b^2}{2I_b} + \frac{J_c^2}{2I_c} = AJ_a^2 + BJ_b^2 + CJ_c^2 \quad (1.4)$$

with

$$A = \frac{\hbar}{4\pi I_a}; B = \frac{\hbar}{4\pi I_b}; C = \frac{\hbar}{4\pi I_c}. \quad (1.5)$$

1.2 Controlling and manipulating molecular beams

I_a, I_b and I_c denote the principal moments of inertia [37]. The rotation of a

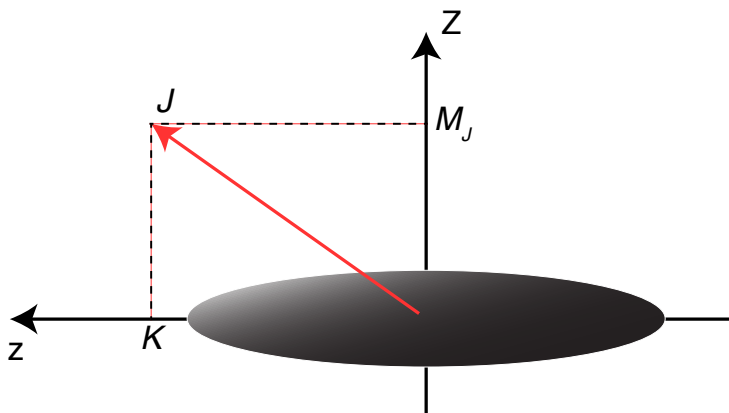


Figure 1.1: Illustration of the quantum numbers J, K and M_J for a rotating molecule.

molecule can be described by three quantum numbers, J denotes the total angular momentum, K is the projection of J onto the principal axis of the molecule and M_J is the projection of J onto the laboratory fixed Z -axis. In the absence of electric fields, the orientation of the molecule in space does not influence its rotational energy and states that only differ in M_J are degenerate [38].

1.2.2.1 Linear top

In a linear top (e.g. OCS), $I_b = I_c$ and the angular momentum vector is oriented perpendicular to the principal axis. Therefore, $K = 0$ and the energy levels are given by:

$$E(J, M_J) = BJ(J + 1). \quad (1.6)$$

1.2.2.2 Symmetric top

In symmetric top molecules, two moments of inertia are identical, in disc shaped (oblate) tops $I_a = I_b < I_c$, football shaped (prolate) tops have $I_a < I_b = I_c$. The energy levels of the prolate symmetric top are:

$$E(J, K, M_J) = BJ(J + 1) + (A - B)K^2. \quad (1.7)$$

1. Introduction and concepts

Analogous, the energy levels of the oblate symmetric top are given by:

$$E(J, K, M_J) = BJ(J + 1) + (C - B)K^2. \quad (1.8)$$

Each level with $K \neq 0$ is $2(2J + 1)$ degenerate since K can have positive or negative values and there are $2J + 1$ M_J states for each K value. If the molecule is subjected to an electric or magnetic field, the M_J degeneracy is lifted but the twofold degeneracy in K remains.

1.2.2.3 Asymmetric top

Asymmetric top molecules have three different moments of inertia and the Schrödinger equation can not be solved analytically. The asymmetric top wave functions can be expressed by a linear combination of symmetric top wave functions:

$$\Psi_{JM}(\phi, \theta, \chi) = \sum_K A_K |JKM\rangle, \quad (1.9)$$

where A_K are numerical constants. The energy levels of the asymmetric rotor are then calculated by setting up Hamilton matrices for each J level in the basis of the symmetric top. The required matrix elements are [39]:

$$\langle J, K, M | \mathcal{H} | J, K, M \rangle = h \left[\frac{B + C}{2} (J(J + 1) - K^2) + AK^2 \right], \quad (1.10)$$

$$\begin{aligned} \langle J, K + 2, M | \mathcal{H} | J, K, M \rangle &= \langle J, K, M | \mathcal{H} | J, K + 2, M \rangle \\ &= \frac{h(B - C)}{4} \sqrt{J(J + 1) - K(K + 1)} \sqrt{J(J + 1) - (K + 1)(K + 2)}, \end{aligned} \quad (1.11)$$

where h is the Planck constant. Diagonalization of these matrices yields the asymmetric top energy levels as $E(J_\tau M_J)$. The index τ is not a real quantum number, it takes values of $-J$ to J and indicates the relative energy of a state within its J manifold.

1.2.3 Molecules in electric fields

If a molecule is subjected to an electric field, the M_J degeneracy is lifted since the internal energy is now dependent on the orientation of the molecule inside the field. The orientation dependency is caused by the Stark effect, that is the interaction of the dipole moment with the external electric field.

1.2.3.1 Stark Effect

The Hamiltonian of a molecule in an electric field ε is:

$$\mathcal{H}_{\mathcal{R},\varepsilon} = \mathcal{H}_{\mathcal{R}} + \mathcal{H}_{\text{Stark}}, \quad (1.12)$$

with

$$\mathcal{H}_{\text{Stark}} = -\varepsilon \sum_{g=x,y,z} \mu_g \phi_{Zg}. \quad (1.13)$$

x, y and z denote a molecule-fixed coordinate system, X, Y and Z are space-fixed axes with Z aligned with the electric field direction. μ_g denotes the dipole moment components along x, y and z . ϕ_{Zg} are direction cosines of x, y, z with reference to X, Y, Z [39]. By solving the Schrödinger equation of $\mathcal{H}_{\mathcal{R},\varepsilon}$ for different field strengths, Stark energy curves can be calculated. In this work, the Stark curves ($W_{\text{Stark}}(\varepsilon)$) and the effective dipole moments (μ_{eff}) were calculated using CMlStark [39]. The effective dipole moment depends on the rotational quantum state of the molecule and is given by the slope of the corresponding Stark energy curve [39, 40]:

$$\mu_{\text{eff}} = -\frac{\partial W_{\text{Stark}}(\varepsilon)}{\partial \varepsilon}. \quad (1.14)$$

Depending on the rotational quantum state of the molecule, the interaction with the electric field either lowers the internal energy of the molecule or raises it. Molecules in quantum states that experience a reduction in energy are called high-field seeking. Consequently, states that raise the internal energy of the molecule are called low-field seeking. Molecules in the rotational ground state are always high field seeking since the dipole moment will be aligned with the field. For rotationally excited molecules, the average orientation of the dipole

1. Introduction and concepts

moment will determine if it is in a high or low field seeking state.

1.2.3.2 Deceleration and Deflection

In the 1920s, Stern and Gerlach provided experimental proof for the quantization of the spatial orientation of angular momentum. They deflected a beam of silver atoms using an inhomogeneous magnetic field [41, 42]. Silver has a single electron in the 5s orbital and the atoms were deflected up or downwards depending on the spin orientation of the 5s electron.

It was realized that similar techniques can be used to manipulate polar molecules with inhomogeneous electric fields. Kallmann and Reiche described the theory for a polar molecule that is deflected by an inhomogeneous electric field in 1921 [43]. The first experimental deflection of polar molecules was done 1927 by Erwin Wrede who deflected a molecular beam of KI molecules to determine the order of magnitude of the dipole moment [44].

In recent years, the Stark effect has been exploited to deflect and decelerate polar molecules in many applications. In a Stark decelerator a packet of molecules in low-field seeking quantum states is slowed down by letting the molecules fly through several electrode stages that produce an inhomogeneous electric field. The electrodes are switched on and off, so that the molecules always fly in a strong electric field and continuously have to "climb" a potential hill [45, 46]. An alternating gradient decelerator enabled the deceleration of molecules in high field seeking quantum states [46]. A bent quadrupole guide can be used to generate a beam of slow molecules by setting the potential so that only the slowest molecules from the tail of the Maxwell-Boltzmann distribution are guided around the bend. Faster molecules are lost from the guide since the potential is too weak to confine them [47, 48].

Most relevant to this work is the spatial separation of specific conformers, achieved recently by Filsinger *et al.* [49–51]. Different conformations of a molecule usually exhibit different dipole moments and will therefore be deflected differently if they are subjected to an inhomogeneous electric field. If the dipole moment difference between the conformers is sufficiently large, conformationally pure molecular beams can be prepared. The conformer selector intrinsically is

also a rotational state selector and a molecular beam of OCS molecules in the rotational ground state could be prepared [52].

For the experiments reported in the following chapters, the electrostatic deflector design of Filsinger *et al.* was used to separate conformers or rotational states in molecular beams.

1.3 Ion trapping and laser cooling

Linear quadrupole radiofrequency ion traps are widely used instruments for the trapping and cooling of atomic and molecular ions. Cold, trapped ions are of interest for a variety of topics, ranging from precision spectroscopy [53] and quantum information [54] to the dynamics of ion-molecule reactions [55–57]. Laser- and sympathetically-cooled ions in traps form ordered structures termed Coulomb crystals [58]. Rate constants for molecules reacting with the laser or sympathetically-cooled ions can be determined by observing changes in the crystal structure.

Trapping ions can be easily realized through their Coulomb interaction with electric fields. For trapping, one needs to generate a three dimensional electric potential minimum. This is not possible with only static electric fields since the Laplace equation

$$\nabla^2\Phi = \frac{\partial^2\Phi}{\partial x^2} + \frac{\partial^2\Phi}{\partial y^2} + \frac{\partial^2\Phi}{\partial z^2} = 0 \quad (1.15)$$

has to be fulfilled. If the potential Φ has a minimum in the x and y dimension, that is the first two terms are positive, the last term has to be negative and the potential will be non-confining along the z -dimension. To generate a three dimensional confining potential, dynamic trapping fields have to be employed. In 1989 W. Paul was awarded the Nobel prize for the development of the radiofrequency ion trapping technique [59]. In a Paul trap, the ions are confined by a dynamic quadrupole field in two dimensions and by a static DC field that is superimposed along the third dimension. The spherical Paul trap consists of a ring electrode and two parabolic endcap electrodes. In many modern cold chemistry and physics experiments a linear version of this ion trap is used [60–64]. A schematic drawing of a linear Paul trap is given in Figure 1.2. The advantage of

1. Introduction and concepts

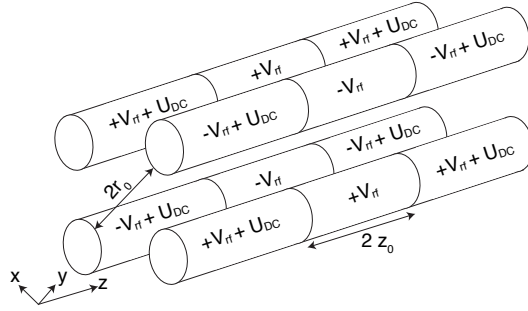


Figure 1.2: Schematic drawing of a linear quadrupole ion trap.

the linear design is good optical access for addressing the trapped ionic species with lasers, allowing for laser-cooling and spectroscopy of the ions. Also, the trapping volume is larger and the linear quadrupole ion trap has a line instead of a point of zero rf field. A radiofrequency (rf) potential is applied to the electrodes with a π -phase shift on adjacent rods. This generates a quadrupole field and the ions are confined along the z axis by applying a static DC offset to the "endcap" electrodes (see Figure 1.2). The time-dependent trapping potential is described by:

$$V(x, y, t) = V_{\text{rf}} \left(\frac{x^2 - y^2}{r_0^2} \right) \cos(\Omega_{\text{rf}} t), \quad (1.16)$$

where V_{rf} is the rf amplitude and Ω_{rf} is the angular rf frequency. This potential generates a confining force in the radial dimension by creating a rotating saddle shape potential. The static potential along z is given by:

$$U(x, y, z,) = \frac{\kappa U_{\text{DC}}}{z_0^2} \left[z^2 - \frac{1}{2}(x^2 + y^2) \right], \quad (1.17)$$

where κ is a geometrical factor. The equations of motion of the ions in the trap are given by the Mathieu equations:

$$\ddot{u} + (a_u - 2q_u \cos(\Omega_{\text{rf}} t))u = 0, \quad (1.18)$$

1.3 Ion trapping and laser cooling

where u denotes x, y or z . The a_u and q_u are dimensionless Mathieu stability parameters [60, 64, 65]:

$$a_x = a_y = -\frac{1}{2}a_z = -\frac{4q\kappa U_{\text{DC}}}{mz_0^2\Omega_{\text{rf}}^2}, \quad (1.19)$$

$$q_x = -q_y = \frac{4qV_{\text{rf}}}{m\Omega_{\text{rf}}^2 r_0^2}, \quad q_z = 0. \quad (1.20)$$

The trajectories of an ion inside the trap look like Lissajous curves that are composed of two frequency components. These secular frequencies are given by:

$$\omega_u = \frac{\Omega_{\text{rf}}}{2} \sqrt{a_u + \frac{q_u^2}{2}}. \quad (1.21)$$

In the ion traps used in this work, the radial secular frequencies for Ca^+ ions are on the order of ≈ 100 kHz for typical operating conditions of $V_{\text{rf}} = 300$ V, $\Omega_{\text{rf}} = 2\pi \times 3$ MHz and $U_{\text{DC}} = 5$ V. On top of the slow secular motion, the ions move in a fast periodic motion driven by the rf field. This micromotion is zero for ions at the central line of the trap since the two rf phases with opposite sign cancel each other. With increasing distance to the center line, the micromotion amplitude becomes stronger due to the larger fields experienced by the ion. In the adiabatic approximation [66], the motion of the ions can be described by a time-averaged effective pseudopotential Φ_{pseudo} . For a harmonic potential Φ_{pseudo} is given by:

$$\Phi_{\text{pseudo}}(r, z) = \frac{1}{2}\omega_r^2 r^2 + \frac{1}{2}\omega_z^2 z^2 \quad (1.22)$$

with $r^2 = x^2 + y^2$ [60, 61].

In chapter 3, a new linear ion trap with additional electrodes is described. The stability parameters were obtained from the diagonal elements of A_{ij} and Q_{ij} , the multidimensional generalizations of the Mathieu stability parameters [67, 68],

$$A_{ij} = \frac{4q}{m\Omega_{\text{rf}}^2} \left(\frac{\partial^2 \Phi_{\text{dc}}}{\partial x_i \partial x_j} \right), \quad (1.23)$$

$$Q_{ij} = \frac{2q}{m\Omega_{\text{rf}}^2} \left(\frac{\partial^2 \Phi_{\text{rf}}}{\partial x_i \partial x_j} \right). \quad (1.24)$$

1. Introduction and concepts

The total trapping potential was calculated from the sum of the time-averaged pseudopotential and the static potential:

$$\Psi_{\text{tot}} = \frac{q^2 V_{\text{rf}}^2}{4m\Omega_{\text{rf}}^2} \|\nabla \Phi_{\text{rf}}\|^2 + qU_{\text{dc}} \Phi_{\text{dc}} \quad (1.25)$$

where Φ_{rf} and Φ_{dc} denote the electrode potential basis functions which were obtained from solving the Laplace equation for 1 V applied to the respective electrodes [68] using the Simion software [69].

1.3.1 Laser cooling

The thermal motion of the ions can be slowed down by Doppler laser cooling. Doppler laser cooling is applicable to atomic and ionic species with electronic level structures that enable closed optical cycles [61]. Here it will be discussed for $^{40}\text{Ca}^+$ ions since this is the species used in this work. Figure 1.3.1 shows a schematic of the relevant electronic levels involved in laser cooling of Ca^+ . The ions are cooled by exciting a closed optical cycle of absorption and spontaneous emission at 397 nm. The 4s electron is excited from the electronic ground state $^2S_{1/2}$ to the first excited state (4p) $^2P_{1/2}$, from where it relaxes back to the ground state. Some of the excited electrons do not relax back to the ground state, but to the (3d) $^2D_{3/2}$ state. To close the cooling cycling transition, a second laser at 866 nm has to be used to repump population from the $^2D_{3/2}$ state back to the $^2P_{1/2}$ state. The cooling laser is red detuned from the transition frequency by a few tens of MHz. To ions on counter-propagating trajectories with respect to the cooling laser, the light is blue-shifted by the Doppler effect and they absorb photons. The momentum of the photon is transferred to the ion and the ion is slowed down. On spontaneous emission the ion regains a momentum kick of equal magnitude to the absorption, but the emission process is isotropic and over many absorption and emission cycles the ion is slowed down. The ion is only cooled along one axis, but the Coulomb interaction with the other ions couples all translational degrees of freedom. Therefore, slowing down all three velocity components is possible with only one cooling laser. The theoretical minimum

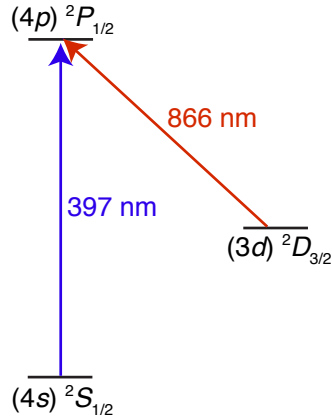


Figure 1.3: Ca⁺ energy level scheme of electronic levels relevant for Doppler laser cooling.

temperature that can be reached by Doppler cooling is:

$$T_{\min} = \frac{\hbar\Gamma}{2k_{\text{B}}}, \quad (1.26)$$

where Γ is the linewidth of the cooling transition. For Ca⁺, the theoretically achievable temperature is: $T_{\min} = 0.5$ mK [61, 64].

Other ion species that are not addressed by the cooling laser can be cooled sympathetically. Due to the Coulomb interaction between all ions, energy is transferred easily and laser-cooled Ca⁺ ions act as a cooling bath for the other species. Laser- and sympathetically-cooled ions in traps form ordered structures termed Coulomb crystals [58]. These Coulomb crystals are useful tools for ion-molecule reaction studies. Rate constants for molecules reacting with the laser cooled or sympathetically cooled ions can easily be determined by observing changes in the crystal structure [58, 61, 70–72].

In this work we make use of the fact that Coulomb crystals are highly localized structures and use them as stationary reaction targets for deflected molecular beams.

1. Introduction and concepts

1.3.2 Molecular dynamics simulations

Coulomb crystals were simulated by solving the classical Newtonian equations of motion of all ions inside the trap. The force experienced by an ion i is given by:

$$\mathbf{F}_i = \mathbf{F}_{\text{trap}} + \mathbf{F}_{\text{Coul}} + \mathbf{F}_{\text{lc}} + \mathbf{F}_{\text{heat}}. \quad (1.27)$$

\mathbf{F}_{trap} is the force generated by the trapping potential and is defined as:

$$\begin{aligned} \mathbf{F}_{\text{trap}}(x, y, z, t) = \nabla \left(V_{\text{rf}} \cos(\Omega_{\text{rf}} t) \sum_{k,l,m} C_{\text{rf}(k,l,m)} (x - x_0)^k (y - y_0)^l (z - z_0)^m \right. \\ \left. + U_{\text{DC}} \sum_{k,l,m} C_{\text{DC}(k,l,m)} (x - x_0)^k (y - y_0)^l (z - z_0)^m \right). \end{aligned} \quad (1.28)$$

$C_{\text{rf}(k,l,m)}$ and $C_{\text{DC}(k,l,m)}$ are coefficients obtained from three-dimensional fourth-order polynomial fits to the potentials Φ_{rf} and Φ_{dc} [68].

\mathbf{F}_{Coul} is the force generated by the Coulomb interaction with all other ions in the trap and is defined as:

$$\mathbf{F}_{\text{Coul}} = \frac{q_i}{4\pi\epsilon_0} \nabla_i \sum_{i \neq j} \frac{q_j}{\mathbf{r}_{ij}}, \quad (1.29)$$

where q is the charge of the respective ion and \mathbf{r}_{ij} is the distance between ion i and j [61, 73]. \mathbf{F}_{lc} is the force generated by the laser cooling and is implemented as a constant friction term that reduces the kinetic energy of the ion. \mathbf{F}_{heat} is a random kick imparted on the ion to simulate heating from experimental imperfections.

The equations of motion were solved using a leapfrog algorithm in an adapted version of the Protomol software [74]. A three dimensional histogram of the ion positions averaged over many timesteps is generated and crystal images are simulated by taking slices of this histogram and applying different amounts of Gaussian blur depending on the distance of the slice to the crystal center. By adding up all blurred slices, a two dimensional image is created that can be compared with the camera images taken in the experiment.

1.4 Ion - molecule reactions

Ion-molecule reactions are important for the rich chemistry happening in the interstellar medium at temperatures of ~ 10 K and have therefore been studied extensively experimentally and theoretically [75–77]. Some of the experimental techniques to study gas phase ion-molecule reactions are the selective ion flow tube (SIFT) [78], the CRESU apparatus [34, 79, 80] and ion traps [48, 61, 81]. Many ion-molecule reactions are exothermic reactions that do not have any barriers along the reaction pathway. These reactions are mostly dependent on the long-range intermolecular potential and can adequately be described by capture models in which one assumes that the reaction probability is unity if the collision energy is large enough to surpass the centrifugal barrier in the entrance channel [82–84]. For collisions with angular momenta that are too large, the centrifugal barrier is too high and a reaction will not happen. The total energy E of two colliding particles is the sum of their kinetic energy, the centrifugal energy and the potential energy:

$$E = \frac{1}{2}\mu v^2 + \frac{L^2}{2\mu R^2} + V(R), \quad (1.30)$$

with $L = \mu v b$ being the angular momentum, μ is the reduced mass, R is the distance, $v = \dot{R}$ is the relative velocity of the two particles, and b denotes the impact parameter.

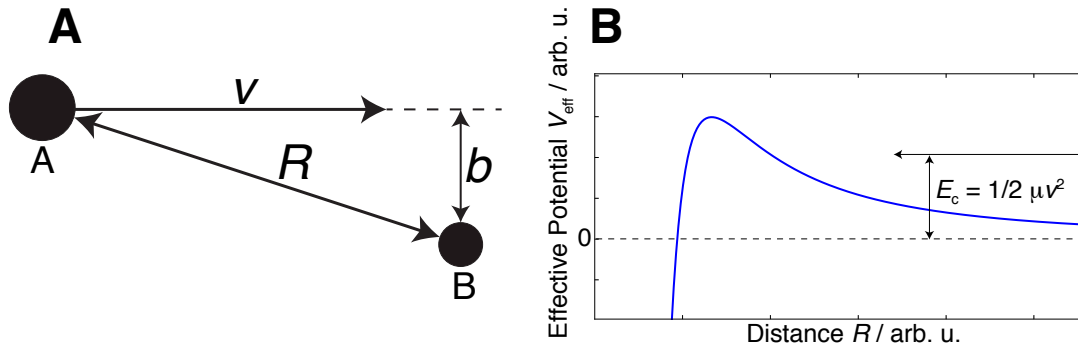


Figure 1.4: **A** Diagram to show the distance parameter R , the relative velocity v and the impact parameter b for two particles A and B. **B** Effective potential with centrifugal barrier.

1. Introduction and concepts

Figure 1.4B schematically shows the centrifugal barrier of the effective potential,

$$V_{eff} = \frac{L^2}{2\mu R^2} + V(R). \quad (1.31)$$

The angular momentum for this particular collision is too large, the centrifugal barrier is higher than the collision energy and the effective potential is repulsive. For every collision energy, there exists a maximum impact parameter b_{\max} for which the centrifugal barrier is equal to the collision energy. The capture cross section is then given by:

$$\sigma = \pi b_{\max}^2 \quad (1.32)$$

and the capture rate constant is:

$$k = \sigma v. \quad (1.33)$$

The intermolecular potential $V(R)$ for an ion reacting with a polar molecule is given by:

$$V(R, \beta) = -\frac{\alpha q^2}{2R^4} - q\mu_D \frac{\cos(\beta)}{R^2} \quad (1.34)$$

where R is the distance from the ion to the center of mass of the molecule, μ_D and α denote the dipole moment and the isotropic polarizability of the molecule, q is the charge of the ion and β is the angle between R and the direction of the dipole.

1.4.1 Adiabatic dipole capture theory

All ion-molecule capture rates reported in this work have been calculated using the adiabatic capture theory developed by Clary *et al.* [84–86]. In the following section, the method will be explained for the case of an ion reacting with a symmetric top molecule [85]. For asymmetric top molecules an extension of the theory, developed by Stoecklin *et al.* was used [86].

The attractive ion-molecule long-range potential is given by equation 1.34. The

Hamiltonian for the capture of a symmetric top by an ion is:

$$\mathcal{H} = \mathcal{H}_{\mathcal{R}} + \frac{[j^2 - 2\hbar^2\Omega^2]}{2\mu R^2} + V(R, \beta).^1 \quad (1.35)$$

The Schrödinger equation can be solved by diagonalizing the coupling matrix with the following matrix elements:

$$V_{jj'} = \left\{ E(j, K) + \frac{[j(j+1)\hbar^2 - 2\Omega^2\hbar^2]}{2\mu R^2} - \frac{\alpha q^2}{2R^4} \right\} \delta_{jj'} - \frac{q\mu_{\text{D}} \{C(jj'1 - KK0)C(jj'1 - \Omega\Omega 0)[(2j+1)(2j'+1)]^{1/2}\}}{3R^2}, \quad (1.36)$$

where Ω is the projection of the molecular angular momentum j onto R , K is the projection of j onto the molecular symmetry axis, $E(j, K)$ are the eigenvalues of $\mathcal{H}_{\mathcal{R}}$ and are given in equation 1.7, $C(jj'1 - KK0)$ and $C(jj'1 - \Omega\Omega 0)$ are Clebsch-Gordan coefficients. Diagonalizing this coupling matrix for specific K, Ω and R values gives rotationally adiabatic potential-energy curves that are denoted $\varepsilon_{jK\Omega}(R)$. For a given total angular momentum J the effective ion-dipole interaction potential can then be calculated from:

$$V_{JjK\Omega}(R) = \varepsilon_{jK\Omega}(R) + \frac{\hbar^2 J(J+1)}{2\mu R^2} - E(j, K). \quad (1.37)$$

To find the maximum total angular momentum $J_{\text{max}}(j, K, \Omega)$ for which the molecule will be captured by the ion, one has to solve

$$V_{JjK\Omega}(R) \leq \frac{1}{2}\mu v^2 \quad (1.38)$$

for J . The right hand side of this inequality is the collision energy E_c and the capture probability is naught if the collision energy is lower than the centrifugal barrier (the maximum of $V_{JjK\Omega}(R)$). Since the molecules in the molecular beam are cold and only the low lying rotational states are populated, $J_{\text{max}}(j, K, \Omega) \gg j$

¹From here on the molecular rotational angular momentum is denoted with a lower case j while the total collision angular momentum is denoted with a capital J .

1. Introduction and concepts

and the capture cross-section is well approximated by:

$$\sigma(j, K, E_c) = \frac{\pi}{[(\frac{2\mu E_c}{\hbar^2})(2j + 1)]} \sum_{\Omega} [J_{\max}(j, K, \Omega) + 1]^2, \quad (1.39)$$

where E_c denotes the collision energy. Rotational state dependent capture rates were calculated by multiplying the cross-section with the collision velocity:

$$k(j, K) = \sigma(j, K, E_c)v. \quad (1.40)$$

To get effective capture rate constants for an ion-molecule reaction, one has to know the rotational state population of the molecules in the beam and sum over all state dependent rates and weight them by the according state population factor. The rotational state populations were obtained from Monte-Carlo trajectory simulations of the deflected molecular beam.

1.4.2 Monte-Carlo trajectory simulations

Trajectory simulations of molecules flying through the deflector were performed either using libcoldmol [87] or BaselFly. In both programs the initial position and velocity of the molecules are Monte-Carlo sampled using a random number generator. The molecule trajectories are then solved with standard molecular dynamics techniques by solving the Newtonian equations of motion. BaselFly is a homebuilt Fortran program that allows to simulate large particle numbers in a short amount of time. A trajectory simulation of 10^6 molecules needs ~ 80 s of computation time per quantum state on a regular desktop computer. For each quantum state, a sample of molecules is generated at the position of the valve. A random number generator is used to sample the start position and velocity for each molecule from a circular uniform distribution in x and y , and normal velocity distributions in x , y and z . The direction of the molecular beam is oriented along the z axis and the molecules are all initialized at the same z starting position. Intermolecular interactions are neglected and each molecule is propagated in free flight to the deflector position. It is checked whether the molecule collides with any of the skimmers in front of the deflector and whether

it can enter the deflector. The molecule is then propagated through the deflector where it experiences a force $\vec{F} = -\nabla W_{\text{Stark}}(\varepsilon)$ and the 3D equations of motion are integrated using a fifth order Runge-Kutta method. While the molecule is flying through the deflector it is checked regularly if it hits one of the deflector electrodes. After exiting the deflector, the molecule is propagated in free flight to the position of the ion trap.

To simulate a deflection profile of the molecular beam all relevant quantum states have to be simulated and deflection profiles I_s are generated for each quantum state from all molecules that did not hit a skimmer or the deflector. The final deflection profile $I(y, T_{\text{rot}})$ is a sum of these deflection profiles weighted by their population in the molecular beam:

$$I(y, T_{\text{rot}}) = \sum_s w_s(T_{\text{rot}}) I_s(y). \quad (1.41)$$

The population weight $w_s(T_{\text{rot}})$ is given by:

$$w_s(T_{\text{rot}}) = g_M g_{ns} e^{(W_0 - W_s)/(k_B T_{\text{rot}})}, \quad (1.42)$$

where W_0 and W_s denote the field-free rotational energy of the ground state and state s , $g_M = 1$ for $M = 0$ and $g_M = 2$ for all other values of M , g_{ns} is the nuclear spin statistical weight and k_B is the Boltzmann constant.

The rotational temperature of the molecular beam in the experiment was determined from varying the rotational temperature in the simulated deflection profiles until the best agreement with the experimentally observed deflection profiles was achieved.

1.5 Mass spectrometry

In the reactions reported in this work, only the ionic reaction products remain trapped in the ion trap and can be further investigated. In order to analyze the products and understand the reaction mechanisms, mass spectrometry (MS) was utilized. MS yields the mass-to-charge ratio (m/q) of the investigated species. In this work, two different MS techniques have been employed and the general

1. Introduction and concepts

concepts are explained here.

1.5.1 Resonant excitation mass spectrometry

The mass-to-charge ratio of the ionic reaction products can be determined by resonant-excitation mass spectrometry (REMS) [61, 62, 88]. This non-destructive technique was first demonstrated by Baba *et al.* [89]. In REMS, an additional low amplitude drive frequency is applied to one of the trap electrode rods. If this drive frequency is resonant with the secular frequency of an ion, the ion motion is amplified. The kinetic energy of the excited ions is transferred to all other ions in the Coulomb crystal due to the coupling by the Coulomb interaction. This leads to an increase in kinetic energy of the laser-cooled ions which changes their Doppler shift and leads to a change in the laser-induced fluorescence (LIF) yield. By scanning the excitation frequency and measuring the LIF, the secular frequencies of the trapped ionic species can be determined. Since the secular frequencies are dependent on the ion mass (see equation 1.21), the masses of the trapped ion species can be determined.

For small Coulomb crystals, consisting of one single atomic or molecular ion that is sympathetically cooled by one laser-cooled ion, this method is very precise, enabling the distinction of isotopes that differ by only one atomic mass unit (u) [62, 90].

For larger mixed-species Coulomb crystals the REMS spectra become very complex due to Coulomb coupling. This leads to a shift and broadening of the observed frequencies. Also, the frequency shifts are highly dependent on experimental conditions like drive amplitude, scan direction and asymmetries in the trapping potential [61, 91].

1.5.2 Time of flight mass spectrometry

In time of flight mass spectrometry (TOF-MS), ions are accelerated over a short distance and then fly through a field-free drift tube before they are detected. The flight time is dependent on the ion mass-to-charge ratio. The kinetic energy

imparted on an ion during the acceleration is:

$$\frac{1}{2}mv^2 = qEd \quad (1.43)$$

where q is the charge on the ion, E is the electric field strength and d is the distance over which the ion is accelerated. After the initial acceleration the ion passes a grounded grid and enters a field free drift tube with the velocity:

$$v = \sqrt{\frac{2qEd}{m}}. \quad (1.44)$$

The ion arrives at the detector after the drift time:

$$t_D = \frac{D}{\sqrt{\frac{2qEd}{m}}}, \quad (1.45)$$

with D being the length of the drift tube. For two ions with different masses, the ratio of their flight times is:

$$\frac{t_2}{t_1} = \sqrt{\frac{m_2}{m_1}}. \quad (1.46)$$

The resolution of a TOF-MS is given by:

$$\frac{m}{\Delta m} = \frac{t}{2\Delta t}, \quad (1.47)$$

where Δm is a distinguishable mass difference and Δt is the full-width at half maximum (FWHM) of the detected signal [92]. The resolution is limited by two concurring mechanisms, space and energy resolution [93]. Space resolution depends on the initial size of the ion cloud in the source of the TOF-MS. Ions that are closer to the drift tube will gain less kinetic energy and arrive later at the detector than ions which are accelerated over a longer distance d . Energy resolution is dependent on the initial ion velocities before acceleration. Consider two ions with equal velocity starting at the same position in the source but with opposite movement directions at the time the acceleration fields are switched on. The ion with a velocity vector pointing away from the detector will be

1. Introduction and concepts

slowed down, turn around and then be accelerated to the same velocity, but will arrive slightly later than the ion that was already moving towards the detector. Energy resolution can be improved by letting the ions travel in the source for some time before switching on the acceleration fields, but this obviously reduces the space resolution. Both effects lead to signal broadening and the resolution in TOF-MS in the early days was quite limited.

In 1955, Wiley and McLaren presented a TOF-MS with a two-stage acceleration region that greatly improved the achievable resolution in TOF-MS [92, 93]. Figure 1.5 shows a sketch of a Wiley-McLaren TOF-MS. Both electrodes of the

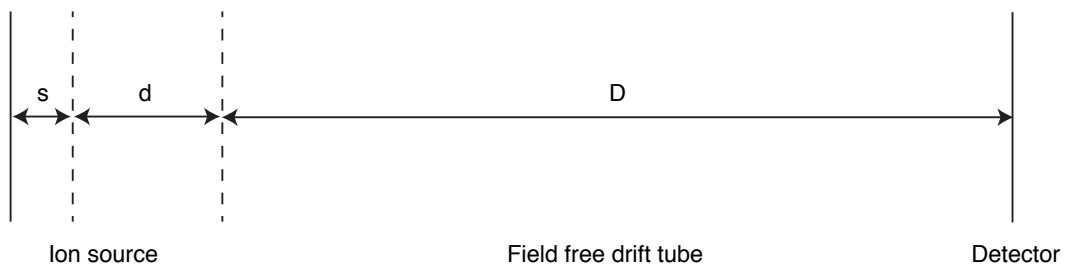


Figure 1.5: Schematic of a Wiley-McLaren TOF-MS.

source region are floated on a common high potential. The third grid separating the acceleration region d from the field free drift tube D is grounded. Ions are created in the source region denoted s . To accelerate the ions, the Source backing plate is pulsed to a slightly higher potential, pushing the ions into the acceleration region where they are accelerated by the much stronger field gradient. Space focusing is achieved by adjusting the field strengths in the source and the acceleration region.

The kinetic energy of an ion in the TOF-MS is:

$$U = U_0 + qs_0E_s + qdE_d, \quad (1.48)$$

with U_0 being the initial kinetic energy, s_0 is the distance of the ion to the first grid and E_s and E_d are the electric field strengths in the source and acceleration region. The total time of flight is the sum of the acceleration time and the drift time [93]:

$$t = t_s + t_d + t_D, \quad (1.49)$$

with

$$t_s = \frac{\sqrt{2m}}{qE_s} [\sqrt{U_0 + qs_0E_s} \pm \sqrt{U_0}], \quad (1.50)$$

$$t_d = \frac{\sqrt{2m}}{qE_d} [\sqrt{U} - \sqrt{U_0 + qs_0E_s}], \quad (1.51)$$

$$t_D = \frac{\sqrt{2m}D}{2\sqrt{U}}. \quad (1.52)$$

Energy focusing can be achieved by introducing a time delay between ion creation and extraction. Since only a small field is used to push the ions into the acceleration region, the space focus is not worsened significantly [93].

Chapter 2

Reactions of spatially separated conformers of 3-Aminophenol with Ca^+ ¹

2.1 Introduction

Based on the methods and concepts discussed in Chapter 1, a new experimental technique was developed for studying ion-molecule reaction rates of specific molecular conformations with cold Coulomb crystallized ions. A molecular beam machine with an electrostatic deflector, for the separation of molecular conformations was coupled to an ion trap to investigate the chemical reactivities, i. e., rate constants, of specific conformers in the prototypical bimolecular reactions of 3-aminophenol (3AP) and Ca^+ [94]. 3AP has two stable conformers (denoted *cis* and *trans*) which differ in the orientation of the OH group and have significantly different dipole moments (2.33 D and 0.77 D for the *cis*- and *trans*-

¹Based on: Chemical-reactions of conformationally selected 3-aminophenol molecules in a beam with Coulomb-crystallized Ca^+ ions. D. Rösch, S. Willitsch, Y-P. Chang and J. Küpper, J. Chem. Phys., 140, 124202 (2014)

Yuan-Pin Chang contributed significantly to the work presented in this chapter. Namely, the simulations of 3-AP deflection curves in sections 2.3.4 and 2.4, as well as the analysis and fitting of the experimental data in section 2.4.3, the determination of the 3-AP density in the molecular beam in section 2.4.2 and the measurement and analysis of the dependence of the reaction rate on the Ca^+ electronic state, reported in section 2.4.4.

species, respectively). 3AP was entrained in a molecular beam and spatially separated using the electrostatic deflector [50]. The dispersed molecular beam was directed at a stationary reaction target consisting of a Coulomb crystal of Ca^+ ions, i. e., an ordered structure of translationally cold ions at a temperature of a few millikelvins in a trap [95]. Singly ionized Ca^+ ions were chosen as a co-reactant because they can easily be Coulomb-crystallized by laser cooling. Ca^+ is also known for its reactivity with organic molecules acting as a catalyst for the activation of inert chemical bonds such as C-F and C-O [96–98].

Sections 2.2 and 2.3 describe the experimental setup and theoretical procedures employed. In Section 2.4, a characterization of the electrostatic deflection of the conformers, their reaction profiles, conformer-specific reaction rate constants as well as mass spectra of the reaction products are presented. An analysis of the results based on theoretical calculations follows in Section 2.5.

2.2 Experimental Setup

The experimental setup consists of two main parts: a molecular beam deflection apparatus for the separation of 3AP conformers and an ion trap apparatus for the generation and storage of Coulomb crystals of laser cooled Ca^+ ions. The individual experimental procedures have been reported previously [50, 87, 94, 95, 99]. In the following, the details of the combined apparatus and the methodology for conformer-specific reaction experiments will be explained.

2.2.1 Conformer deflection setup

The molecular beam machine for conformer deflection consisted of a series of differentially pumped vacuum chambers. The source chamber housing a pulsed valve was pumped by two 1650 l/s turbomolecular pumps. The deflector chamber containing the electrostatic deflector was pumped by a 500 l/s turbomolecular pump, as shown in Figure 2.1 (a). A solid sample of 3AP (Sigma-Aldrich, 98 %) was placed in a reservoir cartridge and vaporized at 145 °C inside a high-temperature Even-Lavie valve [100]. The valve was operated at a backing pressure of 35 bar of neon at a repetition rate of 600 Hz. The typical rotational

2. Reactions of spatially separated conformers of 3-Aminophenol with Ca^+

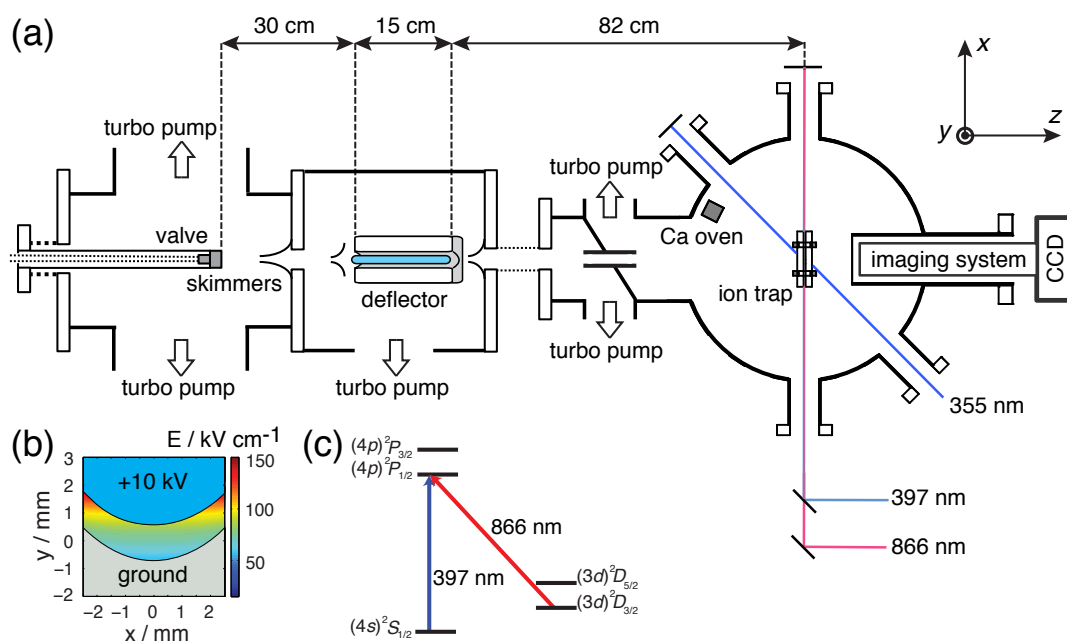


Figure 2.1: (a) Schematic top view of the experimental setup for studying conformer-selected chemical reactions. See text for details. (b) Electric field strength E along a cut through the electrostatic deflector. (c) Diagram of energy levels accessed during Doppler laser cooling of $^{40}\text{Ca}^+$.

temperature of 3AP in our experiments was about 1 K. Two skimmers with diameters of 2 mm and 1 mm were placed 15 cm and 27 cm downstream from the nozzle, respectively. After skimming, the collimated molecular beam entered the 15 cm long electrostatic deflector [101–104]. A cut through the electrodes of the deflector including a contour plot of the generated electric field is shown in Figure 2.1. The vertical gap between the deflector electrodes perpendicular to the molecular beam axis was 1.4 mm. The shape of the electrodes was designed to generate a strong inhomogeneous electric field with a nearly constant gradient along the y axis [101, 102]. The molecular beam passed a third skimmer with a diameter of 1.5 mm for differential pumping into a chamber pumped by a 345 l/s turbomolecular pump. Subsequently, the beam entered the reaction chamber, pumped by a 550 l/s turbomolecular pump, through another differential pumping aperture formed by a 3.5 cm long, 10-mm-diameter tube. Typical pressures during the experiments were $7 \cdot 10^{-6}$ mbar, $9 \cdot 10^{-8}$ mbar, and $2 \cdot 10^{-9}$ mbar in the source, deflector and reaction chambers.

2.2.2 Ion trap setup

In the reaction chamber, Coulomb crystals of laser-cooled Ca^+ ions were generated and trapped in a linear radiofrequency (RF) ion trap [95, 99]. Ca^+ ions were produced by non-resonant multi-photon ionization of a beam of Ca atoms evaporated from an oven and passing through the center of the ion trap [95, 105], see Figure 2.1 (a). The ion trap consisted of four segmented cylindrical electrodes with a radius $r = 4.0$ mm arranged in a quadrupolar configuration. To confine the ions in the plane perpendicular to the trap symmetry axis, RF voltages with amplitudes $V_{0,\text{RF}} = 350$ V and frequencies $\Omega = 2\pi \times 3.1$ MHz were applied with opposite polarities across adjacent electrodes. To confine the ions along the axis, static voltages in the range of $V_{\text{end}} = 1\text{--}10$ V were applied to the endcap electrodes. The atomic beam was ionized using the third harmonic (355 nm) of a Nd:YAG laser close to the center of the ion trap. The Ca^+ ions were laser-cooled with beams produced by two external cavity enhanced diode lasers operating at wavelengths of 397 nm and 866 nm to pump the $(4s) \ ^2S_{1/2} \rightarrow (4p) \ ^2P_{1/2}$ and $(3d) \ ^2D_{3/2} \rightarrow (4p) \ ^2P_{1/2}$ transitions, respectively [95], see Figure 2.1 (c).

2. Reactions of spatially separated conformers of 3-Aminophenol with Ca^+

The frequencies of the two laser beams were simultaneously monitored using an automated fiber-switcher coupled to a wavemeter and stabilized by a computer-controlled voltage feedback loop. The resulting laser linewidths were on the order of a few MHz. The laser powers employed were about $600 \mu\text{W}$ and $200 \mu\text{W}$ for the 397 nm and 866 nm beams, respectively. Upon laser cooling, the ions localized in space and formed three dimensional spheroidal Coulomb crystals [95, 99] with a radius $r \approx 200 \mu\text{m}$ and a width $z \approx 550 \mu\text{m}$ typically consisting of ~ 700 ions. The secular kinetic energy of the laser cooled ions amounted to $E_{\text{sec}} \approx k_{\text{B}} \cdot 10 \text{ mK}$. Two-dimensional cuts of the central plane of the Coulomb crystals were imaged by collecting a solid angle of the atomic fluorescence generated during laser cooling using an enhanced CCD camera coupled to a microscope with ten-fold magnification.

2.2.3 Reaction rate measurements

The first step in each reaction experiment consisted of the formation of a Coulomb crystal. Subsequently, the molecular beam valve was switched on to admit pulse trains of deflected 3AP molecules to collide and react with the spatially localized ions. Different parts of the deflected molecular beam were directed at the stationary Coulomb crystal reaction target by tilting the molecular beam setup in the y direction using a translational stage with a precision of $10 \mu\text{m}$. The width of deflection coordinates sampled by the ion cloud was defined by the y extension of the Coulomb crystals, i.e., $200 \mu\text{m}$. Ions that reacted with 3AP formed product ions which remained trapped, but were not laser cooled and, therefore, did not fluoresce [106]. These product ions were sympathetically cooled by the remaining Ca^+ ions to form a dark shell around the crystal. The progress of the reaction was monitored by observing the shrinking of the bright fluorescing Ca^+ core of the Coulomb crystals as a function of time. Images of the crystals were recorded every 30 s with a camera shutter time of 0.4 s over reaction times of typically 8 to 15 min. From the recorded images, the number of unreacted Ca^+ ions as a function of time was determined from the crystal volumes [106]. Note that the 3AP molecules in the reaction volume were replenished with each gas pulse. Therefore, their number density was essentially constant during the mea-

surement time and the decrease of the number $N(t)$ of Ca^+ ions in the crystal as a function of time t followed pseudo-first-order kinetics. Pseudo-first-order reaction rate constants k_1 were determined at specific deflection voltages and deflection coordinates y according to the rate law

$$\ln \frac{N(y, t)}{N(y, t = 0)} = -k_1(y)t. \quad (2.1)$$

The deflection coordinate y is defined as the offset of the deflected from the nominally undeflected beam at the position of the Coulomb crystal. All measurements were performed with the same power and detuning of the cooling laser from resonance to ensure a constant and well-defined population of all three electronic levels of Ca^+ accessed during laser cooling (see Figure 2.1 (c)). The populations of the relevant Ca^+ states were determined from a calibrated eight-level optical Bloch equation treatment including the effects of magnetic fields [107].

Reactions with residual background H_2 gas in the ion trap chamber also contributed to a removal of Ca^+ ions from the trap. The corresponding loss rates were measured for each set of experiments following the same procedures described as above but without admitting the molecular beam. The resulting values for the background loss rates were subtracted from the measured rates in the actual reaction experiments. Collisions with the Ne carrier gas of the molecular beam did not lead to any observable loss of Ca^+ ions from the trap, as was confirmed by control experiments with pure Ne beams.

2.2.4 Mass spectrometry of trapped ions

The ionic reaction products were analyzed using resonant-excitation mass spectrometry (REMS) of the Coulomb crystals [99, 107]. Here, the motion of specific ion species was resonantly excited by scanning the frequency of an additional RF drive voltage (0.2–0.3 V) applied to one of the trap electrodes. When the RF field was resonant with the motional frequency of a trapped ion species, the Coulomb crystal heated up. This led to a dislocation of the Ca^+ ions from their equilibrium position. REMS were recorded by slowly scanning the

2. Reactions of spatially separated conformers of 3-Aminophenol with Ca^+

excitation frequency while monitoring the increase of the fluorescence yield in a region close to but outside the normal extent of the Coulomb crystal. REMS of multi-component crystals generally show broad peaks that are shifted with respect to single-species crystals [108]. The exact intensity and position of the features depends on the scan speed, the drive amplitude, the scan direction and the crystal composition. Therefore, RE mass spectrometry only allows for an approximate determination of the masses of the species present in a multi-component Coulomb crystal [107].

2.2.5 Molecular beam profile measurements

Spatial deflection profiles of 3AP were recorded in a time-of-flight (TOF) mass spectrometer that replaced the ion-trap apparatus. 3AP molecules were ionized at the same distance from the deflector as the ion trap via resonance-enhanced two-photon ionization (R2PI) by a frequency-doubled pulsed dye laser pumped by a Nd:YAG laser with a repetition rate of 20 Hz. Pulses of 10 ns duration with an energy of approximately 0.4 mJ were focused to a spot size of 240 μm in the interaction volume. The molecular ions were mass-selectively detected by their arrival time on a multi-channel-plate (MCP) detector. *cis*- and *trans*-3AP were differentiated through their distinct excitation wavenumbers of 34109 cm^{-1} and 34467 cm^{-1} , respectively [109].

2.3 Theoretical and computational methods

2.3.1 DFT calculations of reaction paths on the ground-state potential energy surface

Short-range ion-molecule interactions were investigated computationally using density functional theory (DFT) calculations. Stationary points along reaction paths to two possible products were computed at the DFT MPW1K/cc-pVTZ level of theory, using the Gaussian 09 software suite [110–112]. Transition state structures were calculated by a quadratic-singular-transit approach (QST-3) [113, 114], from energy-minimized Ca^+ -3AP and Ca^+ -product-radical

complexes and an initial transition state guess. To verify convergence to a saddle point, the resulting transition state structure was distorted and resubmitted as a starting point in a new QST-3 calculation for the transition state search. Basis set superposition errors were corrected using the counterpoise routine provided in Gaussian 09.

2.3.2 Adiabatic capture theory

Long-range ion-molecule capture kinetics were modeled using the adiabatic capture theory developed by Clary and co-workers [86, 115]. The long-range interaction potential V between an ion and a polar molecule was approximated by the sum of the dominant charge-permanent dipole² and charge-induced dipole interactions

$$V(R, \beta) = -\frac{q\mu_D \cos \beta}{R^2} - \frac{q^2\alpha}{2R^4}, \quad (2.2)$$

where R is the distance between the ion and the center of mass of the 3AP molecule, μ_D is its permanent electric dipole moment, β the orientation angle of the molecular dipole moment with the ion-molecule axis, q the charge of the ion and α the scalar polarizability of 3AP. Using the methods described in ref. [86], centrifugally corrected and rotationally adiabatic potential energy curves for the system $\text{Ca}^+ + \text{cis-}/\text{trans-3AP}$ were calculated for 3AP rotational states with quantum numbers ranging from $j = 0$ to $j = 100$ for R between 2 and 48 a_0 . The dipole moments of 3AP were taken from ref. [117], the isotropic polarizabilities were calculated at the DFT B3LYP/aug-cc-pVTZ level of theory. Rotational-state-specific reaction cross sections for $j = 0$ up to $j = 15$ were calculated from a summation over all partial waves for which the maximum of the centrifugally corrected potential energy curve did not exceed the experimental collision energy. Effective capture rate constants were calculated by multiplying the state-specific cross sections with the velocity and the relevant state populations at the rotational temperature of 3AP in the molecular beam.

²Here, “permanent dipole” refers to the dipole moment of 3AP in its molecular frame [116].

2. Reactions of spatially separated conformers of 3-Aminophenol with Ca^+

2.3.3 Molecular-dynamics simulations of Coulomb crystals

Fluorescence images and REMS of the multi-component Coulomb crystals were simulated using molecular dynamics (MD) methods. MD simulations were performed using a modified version of the Protomol program package [118]. Fluorescence images were simulated from ion trajectories calculated by solving the classical three-dimensional equations of motion of the ions in the trap under the influence of laser cooling [99, 119]. To minimize computer time, an isotropic friction force to emulate laser cooling and the pseudopotential approximation for the ion trap was used [95]. REMS were simulated following the methods described in refs. [107, 108]. Briefly, the Coulomb crystals were offset from the central trap axis by $20 \mu\text{m}$ at the beginning of the simulation and allowed to relax. The Fourier transform of the time-dependent total kinetic energy of the ions yielded the frequency spectrum of the Coulomb crystal which is also the experimental observable. The frequencies obtained by this method were calibrated using a comparison of a measured and calculated REMS of a pure Ca^+ crystal. A correction factor of 0.92 was applied to the calculated frequencies of each spectrum to achieve optimal agreement with the experiment.

2.3.4 Monte-Carlo simulations of molecular beam profiles

The simulation of spatial deflection profiles has been described in detail previously [87, 120]. Briefly, the electric field E and its gradient ($\vec{\nabla}E$) were calculated using finite element methods implemented in the COMSOL Multiphysics program. Stark energy curves $W(E)$ of the 3AP quantum states and their effective dipole moments μ_{eff} were calculated using CMISTark [39] (see Figure 2.2). From the electric fields and Stark energy curves, the molecular beam deflection profiles were calculated with libcoldmol [87]. Trajectories for molecules in individual rotational quantum states were obtained by numerical integration of the 3D equations of motion using a Runge-Kutta algorithm. The initial conditions according to the parameters of the molecular beam were sampled by a Monte-Carlo approach, and every individual molecule was propagated through

2.3 Theoretical and computational methods

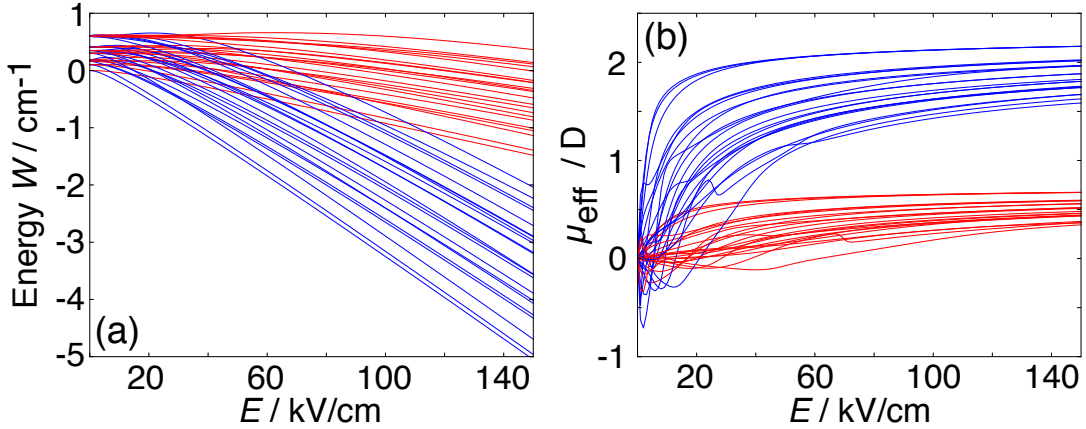


Figure 2.2: (a) Stark energies W for the lowest rotational quantum states $j = 0-2$ of (blue) *cis*- and (red) *trans*-3AP as a function of the electric field strength E . (b) Effective dipole moments μ_{eff} for $j = 0-2$ of *cis*- (blue) and *trans*- (red) 3AP.

a simulated beamline that includes all mechanical apertures of the experimental setup.

The spatial deflection profile $I(y, T_{\text{rot}})$ for an ensemble of molecules at a rotational temperature T_{rot} was calculated from the single-quantum-state deflection profiles $I_s(y)$ using

$$I(y, T_{\text{rot}}) = \frac{1}{w} \sum_{s=1}^N w_s(T_{\text{rot}}) I_s(y). \quad (2.3)$$

Here, N is the number of quantum states included in the simulation and $w_s(T_{\text{rot}}) = g_M g_{\text{ns}} e^{(W_0 - W_s)/(k_B T_{\text{rot}})}$ is the population weight for a given quantum state. W_0 is the field-free energy of the ground state and W_s the field-free energy of state s . $g_M = 1$ for $M = 0$ and $g_M = 2$ otherwise. g_{ns} accounts for nuclear spin statistical weight of the current state with $g_{\text{ns}} = 1$ for all rotational states of 3AP. The normalization constant is given by $w = \sum_{s=1}^N w_s$.

2. Reactions of spatially separated conformers of 3-Aminophenol with Ca^+

2.4 Experimental Results

2.4.1 Deflection curves of 3AP

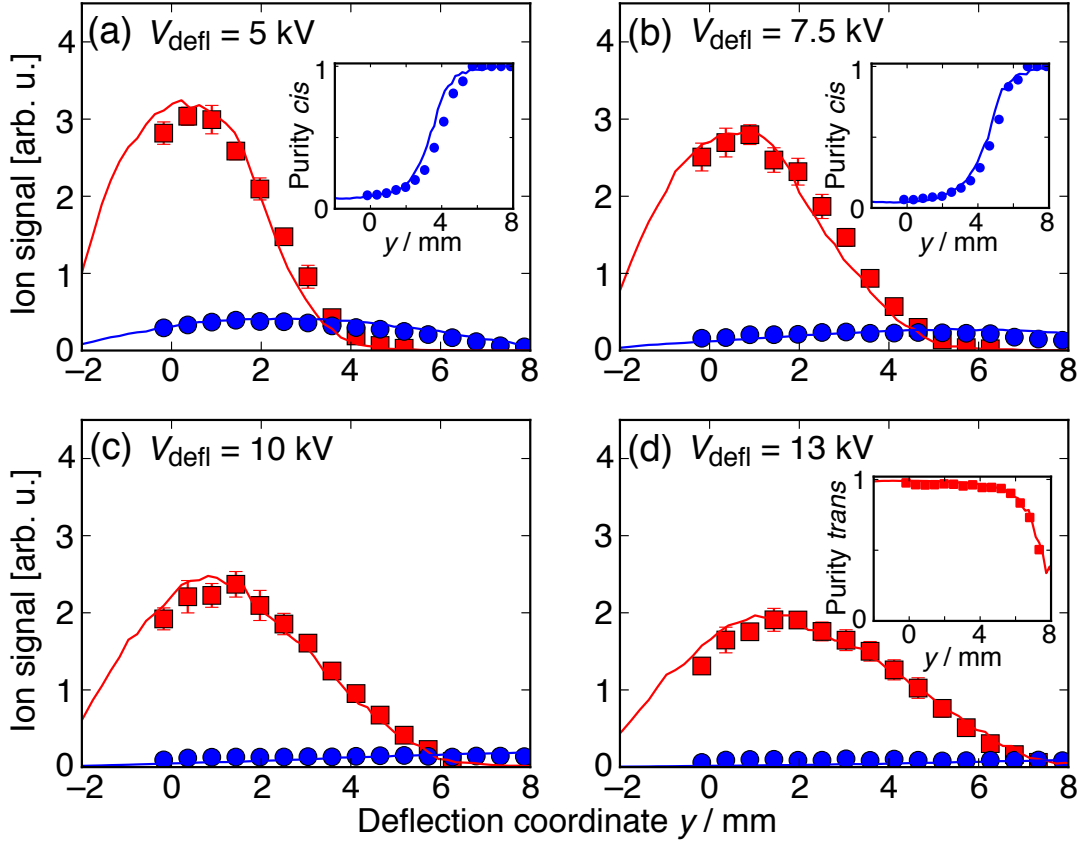


Figure 2.3: Density profiles of the deflected beam of *cis*- (blue) and *trans*-3AP (red) at deflector voltages $V_{\text{defl}} =$ (a) 5 kV, (b) 7.5 kV, (c) 10 kV and (d) 13 kV. These data were measured by conformer-specific multi-photon ionization as a function of the molecular-beam deflection coordinate y . Solid lines: corresponding Monte-Carlo trajectory simulations. In the insets, purities of (a) and (b) *cis* and (d) *trans* conformers are given, as obtained by dividing the relevant conformer density profile by the sum of the *cis* and *trans* profiles. Error bars indicate the statistical 95% confidence interval of the data points.

The density of each conformer in the deflected and dispersed molecular beam was measured by recording the number of R2PI-ionized *cis* and *trans* conformers of 3AP as a function of the deflection coordinate y . The measured conformer-

selective deflection profiles are shown in Figure 2.3, in which each data point represents the signal averaged over 1000 laser shots. When high voltages were applied to the deflector, both conformers were deflected upwards. The deflection was considerably larger for the more polar *cis*-3AP. For instance, for a deflector voltage of 7.5 kV above $y = 6$ mm a pure sample of *cis* conformers was obtained (see Figure 2.3 (b)). The insets in Figure 2.3 show that the fraction of *cis*-3AP in the probed sample can be continuously tuned as a function of y . At heights above the cut-off of the *trans*-3AP beam profile, the density of the *cis* conformers is still comparable to its density in the free jet, i. e., it is only decreased to one fourth. When increasing the voltages to 13 kV (Figure 2.3 (d)), *cis*-3AP was deflected so strongly that it was essentially depleted from the detection region. As a consequence, an almost clean sample of *trans*-3AP was obtained.

Monte Carlo simulations of the deflection curves are shown as solid lines in Figure 2.3. The simulations at an initial rotational temperature of 1.1 K agree well with the experimental profiles. In particular, the fractional intensities plotted in the insets were reproduced by the simulations (solid lines). The simulated profiles and the measured population ratios of the two conformers were used for fitting conformer-specific rate constants from measured reaction rate profiles as described in the following sections.

For the simulated deflection profiles shown in Figure 2.3, different rotational states with rotational angular momentum quantum numbers j have different spatial distributions according to their different effective dipole moments μ_{eff} . Figure 2.4 shows the simulated deflection profiles of individual states ranging from $j = 0$ to $j = 8$. For each profile, the contribution of all j_{τ} states weighted with their relative thermal populations at the rotational temperature of 1.1 K and their statistical weights were included. τ denotes the asymmetric top projection quantum number. Thus, the area underneath each j profile in figure 2.4 represents the relative thermal population of each j manifold at 1.1 K as well as their relative contribution to the reactions. Comparing the deflection profiles of individual j states for the two conformers, profiles of low j of *cis*-3AP exhibit significantly stronger spatial deflection than those of *trans*-3AP. However, for high j states both conformers show similar deflection patterns demonstrating the quickly vanishing dipole moment for rotationally excited species and the

2. Reactions of spatially separated conformers of 3-Aminophenol with Ca^+

need for very cold molecular beams [51].

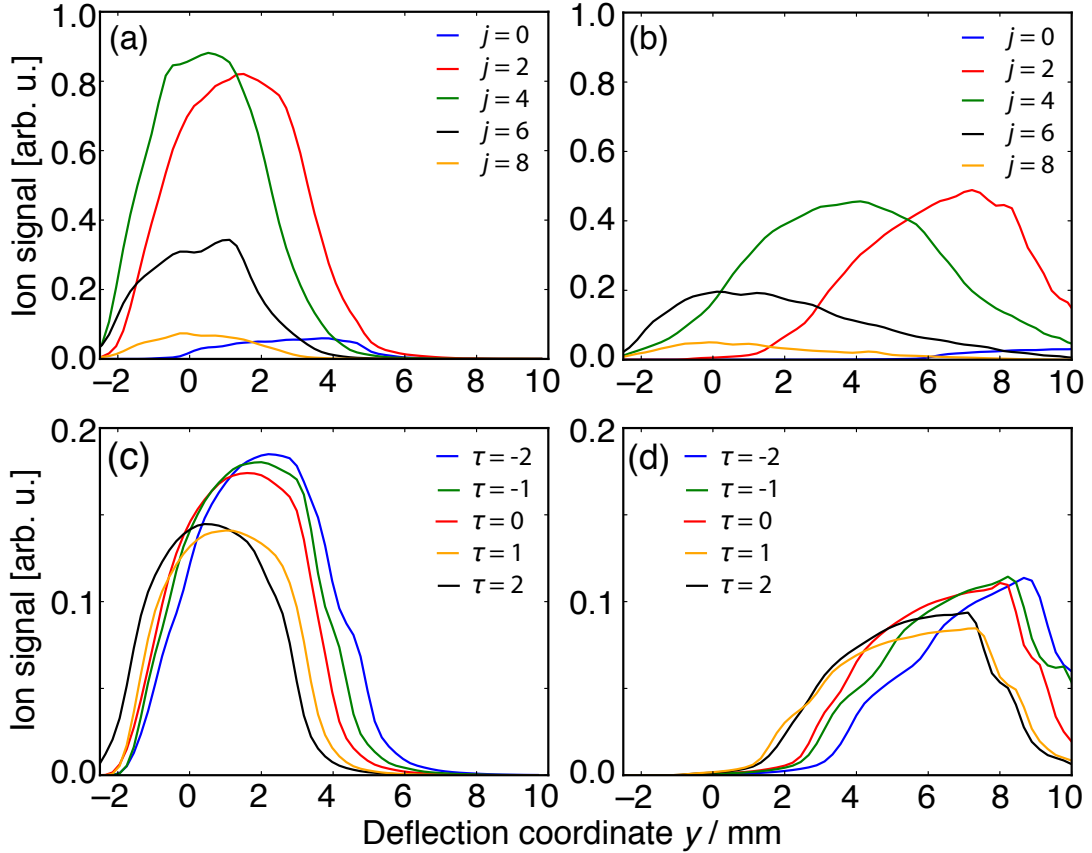


Figure 2.4: Deflection profile simulations at $V_{\text{defl}} = 7.5$ kV for even $j = 0$ to $j = 8$ for specific rotational states j of (a) *trans*- and (b) *cis*-3AP, and for specific asymmetric-top quantum numbers τ at $j = 2$ of (c) *trans*- and (d) *cis*-3AP. See text for details.

2.4.2 Number density of 3AP

The absolute number density of 3AP in the molecular beam was derived by calibration against the reaction $\text{N}_2\text{O} + \text{Ca}^+ \rightarrow \text{CaO}^+ + \text{N}_2$. From measurements of the pseudo-first-order rate constants for this reaction and the reported value for the second-order-rate constant [121], the density of N_2O molecules in the beam was determined. The ratio of the experimentally determined first order rate constant to the known second order rate constant was equivalent

to the time-averaged number density n_{avg} . For $k_1 = 4.30(4) \times 10^{-3} \text{ s}^{-1}$, measured with a beam of 50 mbar of N_2O seeded in 30 bar of Ne we obtained $n_{\text{avg}}(\text{N}_2\text{O}) = 3.84(62) \times 10^7 \text{ cm}^{-3}$. Assuming that the number densities in the beam were proportional to the partial pressures before expansion (for 3AP at 145 °C approximately 10 mbar [[122]]), the 3AP density was estimated to be $n_{\text{avg}} = 7.7(12) \times 10^6 \text{ cm}^{-3}$.³

2.4.3 Reaction profiles and conformer-specific rate constants of $\text{Ca}^+ + 3\text{AP}$

In Figure 2.5, the experimentally determined pseudo-first-order rate constants $k_{1,\text{total}}$ are shown as a function of deflection coordinate y for four deflector voltages $V_{\text{defl}} = 5, 7.5, 10$ and 13 kV. Each data point in Figure 2.5 represents the mean of at least four individual reaction measurements. The measured rate constants $k_{1,\text{total}}(y)$ reflect both, the density distributions of conformers in the deflected molecular beam $n_{\text{trans}/\text{cis}}$ and the conformer-specific second-order rate constants $k_{2,\text{trans}/\text{cis}}$ of the reaction:

$$k_{1,\text{total}}(y) = k_{2,\text{cis}} n_{\text{cis}}(y) + k_{2,\text{trans}} n_{\text{trans}}(y) \quad (2.4)$$

$n_{\text{trans}}(y)$ and $n_{\text{cis}}(y)$ were determined as described in Section 2.4.1. The population weighted-rate constants $k_{2,\text{cis}}$ and $k_{2,\text{trans}}$ were determined from a global fit of Equation (2.4) to the reaction-rate profiles in Figure 2.5. The fit yielded the conformer-specific rate constants $k_{2,\text{cis}} = 2.3(9) \times 10^{-10} \text{ cm}^3 \text{ s}^{-1}$, $k_{2,\text{trans}} = 1.1(4) \times 10^{-10} \text{ cm}^3 \text{ s}^{-1}$ (both values are Ca^+ electronic state averaged) and the ratio $k_{2,\text{cis}}/k_{2,\text{trans}} = 2.1(5)$ within a 95% confidence interval. This fit also yielded the rotational temperature of the molecules in the beam to be 1.1 K.

³For 3AP, the number density in each gas pulse n_{pulse} is equal to $2.56(41) \times 10^8 \text{ cm}^{-3}$. n_{avg} equals to a product of the gas pulse duration (50 μs), the repetition rate (600 Hz), and n_{pulse} .

2. Reactions of spatially separated conformers of 3-Aminophenol with Ca^+

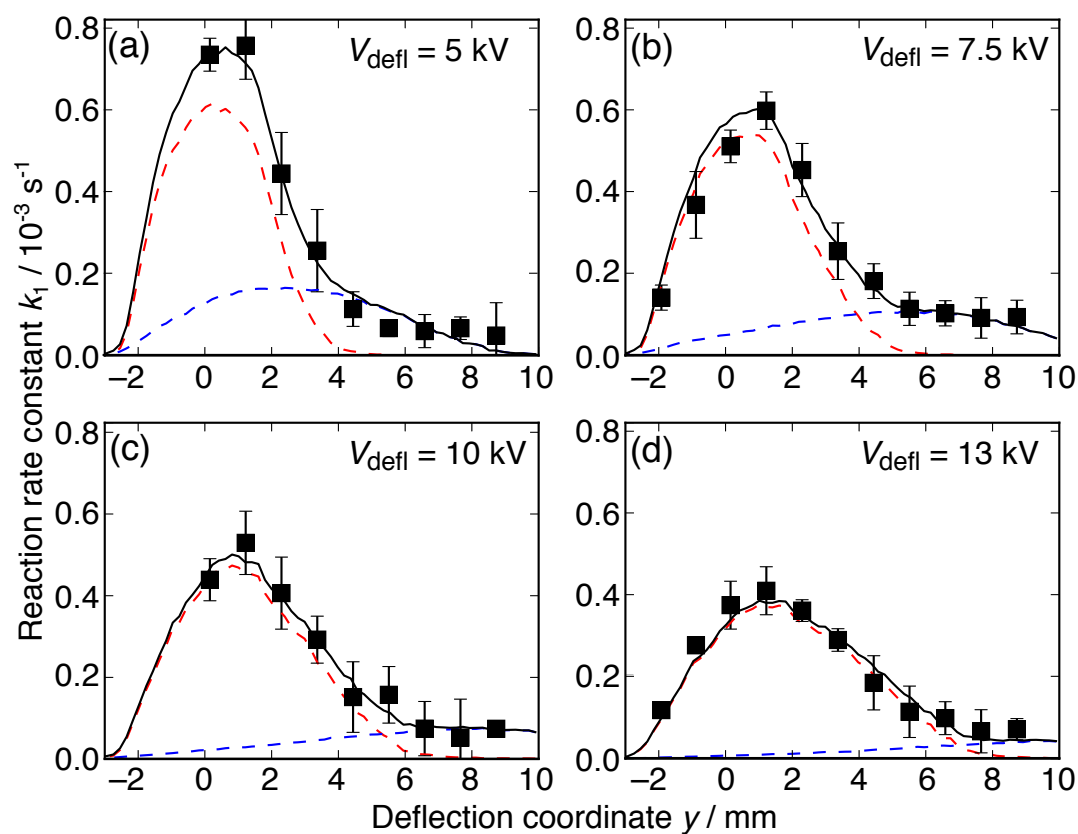


Figure 2.5: Reaction profiles (symbols) and their fits (lines) at (a) 5 kV, (b) 7.5 kV, (c) 10 kV and (d) 13 kV. The solid black lines represent the calculated total contributions of both conformers. Dashed lines represent individual contributions of the *trans* (red) and *cis* (blue) conformers. Error bars indicate the statistical 95% confidence interval of the data points.

2.4.4 Variation of Ca^+ electronic state populations

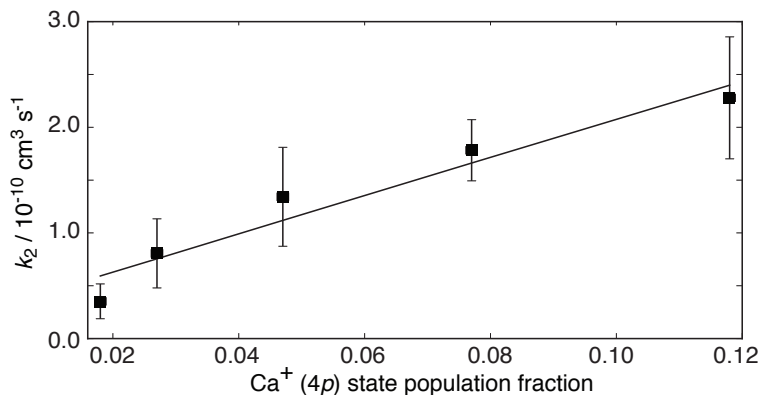


Figure 2.6: Conformer-averaged bimolecular rate constant k_2 as a function of the population in the Ca^+ ($4p$) state. Error bars represent the statistical 95% confidence interval. The line represents a linear regression to the data.

As described in Section 2.2.2, Ca^+ ions were continuously excited during laser cooling so that collisions occurred between 3AP and Ca^+ in the ($4s$) $^2S_{1/2}$, ($3d$) $^2D_{3/2}$ and ($4p$) $^2P_{1/2}$ states. To study the effect of the electronic excitation of Ca^+ on the reaction rates, we varied the Ca^+ state populations by changing the detuning of the cooling laser beam from the ($4s$) \rightarrow ($4p$) resonance while optimizing the ($3d$) \rightarrow ($4p$) repumping laser detuning to achieve the best cooling conditions. Figure 2.6 shows the measured rate constants as a function of the ($4p$) state population using an undeflected molecular beam of 3AP molecules. From this set of measurements, the state-specific rate constants k_2 listed in Table 2.1 were derived following the procedures outlined in refs. [105, 107]. The rate constant for reactions out of the excited ($4p$) state was found to be two to three orders of magnitude larger than the rate coefficients for reactions out of the ($4s$) and ($3d$) states. In the experiments reported in this paper, a detuning of 47-56 MHz was used, yielding a population of the ($4p$) level of 5 – 10%. Because of its large rate constant, this channel dominates the reaction rates observed in the experiment and the contribution of the other channels can be neglected in good approximation. Thus, one can assume that the conformer-specific rate constants determined in 2.4.3 only reflect reactions with Ca^+ ($4p$). Scaled to a state population of 100%, the conformer-specific second-order rate-

2. Reactions of spatially separated conformers of 3-Aminophenol with Ca^+

constants $k_{2,cis} = 3.2(13) \times 10^{-9} \text{ cm}^3 \text{ s}^{-1}$ and $k_{2,trans} = 1.5(6) \times 10^{-9} \text{ cm}^3 \text{ s}^{-1}$ for the reaction of *cis*-3AP and *trans*-3AP, respectively, with Ca^+ ($4p$) were obtained.

Table 2.1: Bimolecular rate constants k_2 for reactions of Ca^+ in its relevant electronic states with 3AP molecules in an undeflected beam.

Reaction channel	$k_2 / \text{cm}^3 \text{ s}^{-1}$
$\text{Ca}^+ (4s) \ ^2S_{1/2} + 3\text{AP}$	$2.66(44) \times 10^{-11}$
$\text{Ca}^+ (3d) \ ^2D_{3/2} + 3\text{AP}$	$2.69(45) \times 10^{-12}$
$\text{Ca}^+ (4p) \ ^2P_{1/2} + 3\text{AP}$	$1.91(32) \times 10^{-9}$

2.4.5 Mass spectra of reaction products

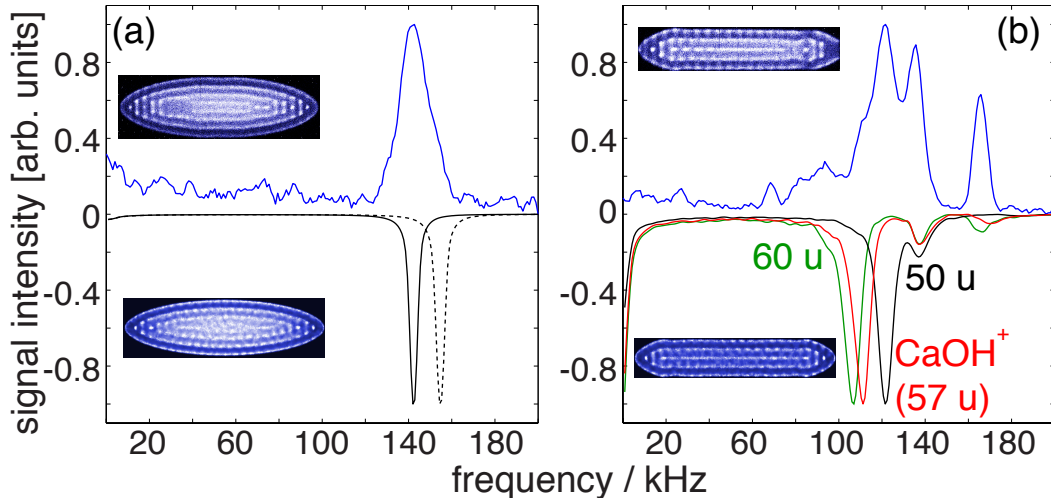


Figure 2.7: Resonance-excitation mass spectra (upper traces) and their molecular dynamics simulations (lower inverted traces). (a) Top: experimental spectrum of a pure Ca^+ crystal. Bottom, dashed line: corresponding simulation using a crystal with 675 ions. Solid line: simulated spectrum scaled by 0.92 along the frequency axis to match the experiment. (b) Top: experimental spectra after a reaction time of 8 min with 3AP. Bottom: scaled simulated spectra of crystals composed of 350 Ca^+ and 325 heavy ions with mass 50 u (black), 57 u (red), and 60 u (green).

Figures 2.7 (a) and (b) show REMS before and after a typical reaction, respectively. In the spectrum of the pure Ca^+ Coulomb crystal, Figure 2.7 (a), a single peak at an excitation frequency of 140 kHz was observed. This feature was also present in the REMS of the multi component crystal after the reaction and could unambiguously be assigned to the excitation of Ca^+ ions with a mass of 40 u. The spectrum of the Coulomb crystal after reaction showed two additional strong peaks at 120 and 165 kHz. The feature at 120 kHz was assigned to product ions. MD simulations for crystals composed of 350 Ca^+ and 325 heavier ions indicate that the product ion mass is in the range of 50 to 60 u, suggesting that the reaction products are CaOH^+ (57 u) or CaNH_2^+ (56 u). As discussed in detail in refs. [107, 108], our approximate simulation approach cannot be expected to perfectly reproduce the observed peak positions and intensities in the spectra as it is not a faithful representation of the complex processes leading to the signal measured in the experiments (see Section 2.3.3). Nonetheless, the MD simulations serve as a useful guide for the interpretation of the mass spectra.

Based on the analysis of the ion trajectories obtained in the MD simulations, the peak at ≈ 165 kHz was assigned to a high-frequency excitation of Ca^+ ions in the combined potential of the trapping fields and the product ions. The weak broad signal in the range from 60–100 kHz is indicative of the presence of even higher masses, possibly arising from consecutive reactions of the primary product ions with 3AP from the molecular beam.

2.5 Reaction mechanisms and kinetics

2.5.1 Reaction pathways on the ground-state potential energy surface

According to Table 2.1, the Ca^+ ($4p$) state rate constant is at least two orders of magnitude larger than those in the ($4s$) and ($3d$) states, suggesting different reaction dynamics for these channels. The large values for the rate constants obtained for reactions in the Ca^+ ($4p$) state are indicative of a capture process [79, 123]. In this case, the reaction rate is limited by the rate of formation of the reaction complex. Afterward, the reaction proceeds with near unit ef-

2. Reactions of spatially separated conformers of 3-Aminophenol with Ca^+

iciency. The kinetics of the reaction are then solely controlled by long-range intermolecular interactions. For reactions with Ca^+ ($4s$) and ($3d$), however, the significantly smaller rate constants compared to the capture limit are indicative of the existence of barriers on the reaction path which limit the reaction rates [124, 125]. In the next paragraphs, the possible roles of the different 3AP conformations in these two types of situations are discussed.

While a high-level *ab initio* calculation for the potential energy surfaces of the excited channels is beyond the scope of the present work, the results of the DFT calculations for the ground-state surface can nonetheless give valuable insights into possible transition-state (TS) structures and reaction pathways.

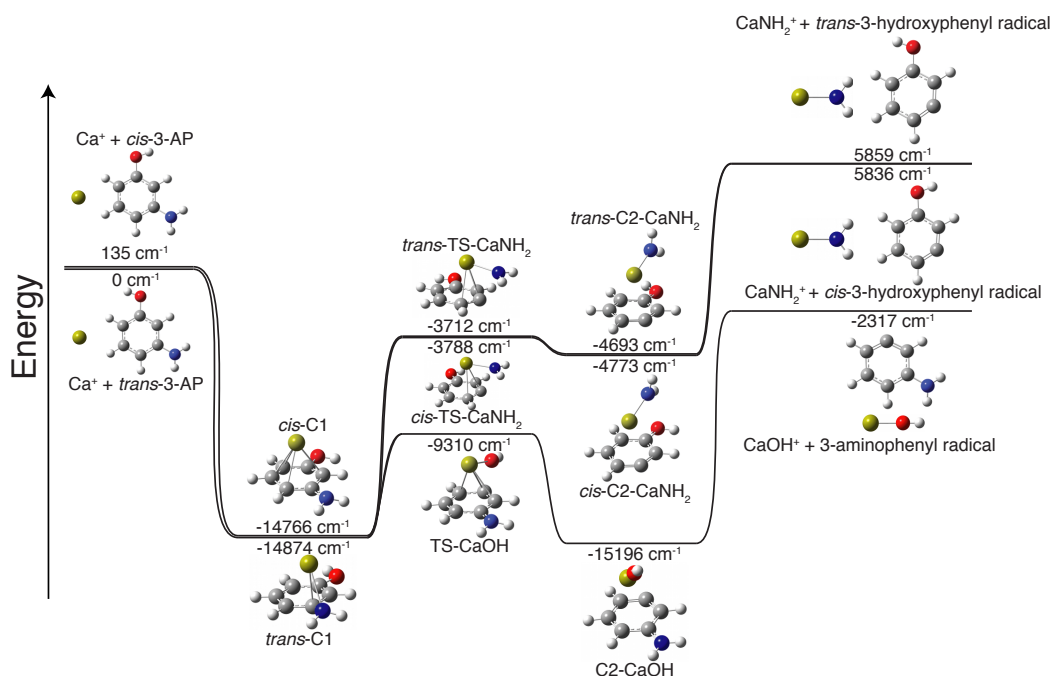


Figure 2.8: Schematic energy diagram of stationary points and transition states on the $\text{Ca}^+(4s) + \text{cis/trans-3AP}$ potential energy surface. See text for details.

Figure 2.8 shows a schematic potential energy diagram of stationary points and TS of the $\text{Ca}^+(4s) + \text{cis/trans-3AP}$ reaction. The reactants form the ion-molecule complex C1 in the entrance channel in which Ca^+ is bound above the aromatic ring. From C1, the reaction proceeds either by abstraction of OH or NH₂, yielding the ionic products CaOH^+ and CaNH_2^+ , respectively. For the

2.5 Reaction mechanisms and kinetics

pathway leading to CaOH^+ + 3-aminophenyl radical, the reaction proceeds through TS-CaOH. This TS was found to be identical for both conformers of 3AP as the OH group is displaced from the aromatic ring towards the Ca^+ ion. The resulting products are identical for both conformers. This pathway is calculated to be exothermic by ≈ 0.3 eV (2320 cm^{-1}).

For the second pathway, leading to CaNH_2^+ and *cis/trans*-3-hydroxyphenyl radical, a TS structure TS-CaNH₂, analogous to TS-CaOH, was found. The Ca^+ ion is coordinated above the aromatic ring and the amino group is displaced out of the plane towards the ion. Two different TS-structures for the two conformers of 3AP exist. They differ by the orientation of the OH-group with respect to the amino group. Their energy difference was calculated to be 76 cm^{-1} . The conformational dependence is preserved throughout the product channel, but the energy difference between the two conformeric pathways is very small. The pathway leading to CaNH_2^+ is calculated to be endothermic by ≈ 0.7 eV (5646 cm^{-1}). Under the present conditions, this second pathway is expected to be thermodynamically accessible only for reactions with Ca^+ in the excited (*4p*) and (*3d*) states.

The present DFT calculations predict that Ca^+ in its ground state reacts with 3AP to CaOH^+ via a submerged transition state, TS-CaOH in Figure 2.8, that is lower in energy than the reagents. The energy profile along the reaction coordinates is reminiscent of the situation in related abstraction reactions, e. g., $\text{Ca}^+ + \text{CH}_3\text{F}$ [96, 106] or the reactions of O atoms with alkenes [124, 126]. The present calculations predict the TS structure to be 1.2 eV lower in energy than the reactants. Comparing with the kinetics in similar type of reactions as observed in refs. [96, 124, 126], it is difficult to see how the low-lying barrier in the present case can lead to a rate constant for the Ca^+ (*4s*) + 3AP channel about two orders of magnitude lower than the capture limit observed (see Section 2.4.4). Possible reasons for this discrepancy could be an underestimation of the barrier height by the current DFT approach or the existence of additional barriers or dynamic constraints that have not been accounted for. Overall, the present calculations give no indication of a short-range reaction mechanism that could explain the factor of 2 difference in the observed rate constants for the reaction of *cis/trans*-3AP with Ca^+ in its ground state.

2. Reactions of spatially separated conformers of 3-Aminophenol with Ca^+

2.5.2 Capture dynamics in the $\text{Ca}^+ (4p) + 3\text{AP}$ excited channel

Figure 2.9 shows centrifugally corrected adiabatic potential energy curves for the reaction of $\text{Ca}^+ (4p)$ with *cis* and *trans*-3AP in their $j = 0$ rotational states. In the case of *cis*-3AP, the centrifugal barrier is more strongly suppressed and reactive collisions proceed up to larger maximum values J_{max} of the total angular momentum. For the collision energy of the present study (0.123 eV), we find $J_{max} = 417$ and 342 for the *cis*- and *trans*-conformers, respectively. Thus, in a classical picture, a larger impact parameter $b_{max} = J_{max}/\mu v$ results for the *cis*-conformer, with μ being the reduced mass and v the collision velocity so that a larger reaction cross section $\sigma = \pi b_{max}^2$ is obtained for the *cis* compared to the *trans* species.

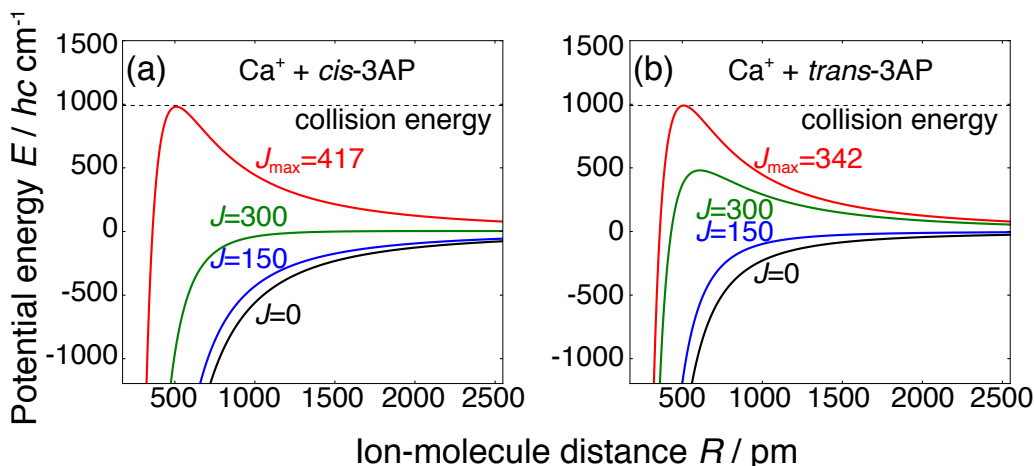


Figure 2.9: Centrifugally corrected long-range interaction potentials for (a) *cis*- and (b) *trans*-3AP in the rotational ground state $j = 0$. From [Chang et al., *Science* **342**, 98 (2013)].

As shown in figure 2.10, the calculated capture rate constants depend on the collision energy. Moreover, the monotonic increase of rate constants with decreasing collision energy is more prominent for the *cis*-species with the larger dipole moment. Therefore, the ratio of the reactivity between the two conformers becomes larger for smaller collisional energies.

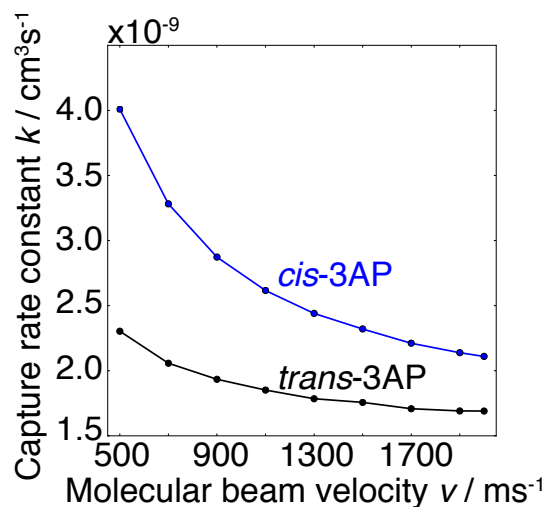


Figure 2.10: Capture rate constants of *cis*- and *trans*-3AP in the rotational quantum state $j = 0$ as a function of the collision velocity. The experimental collision velocity amounted to $v = 900 \text{ ms}^{-1}$.

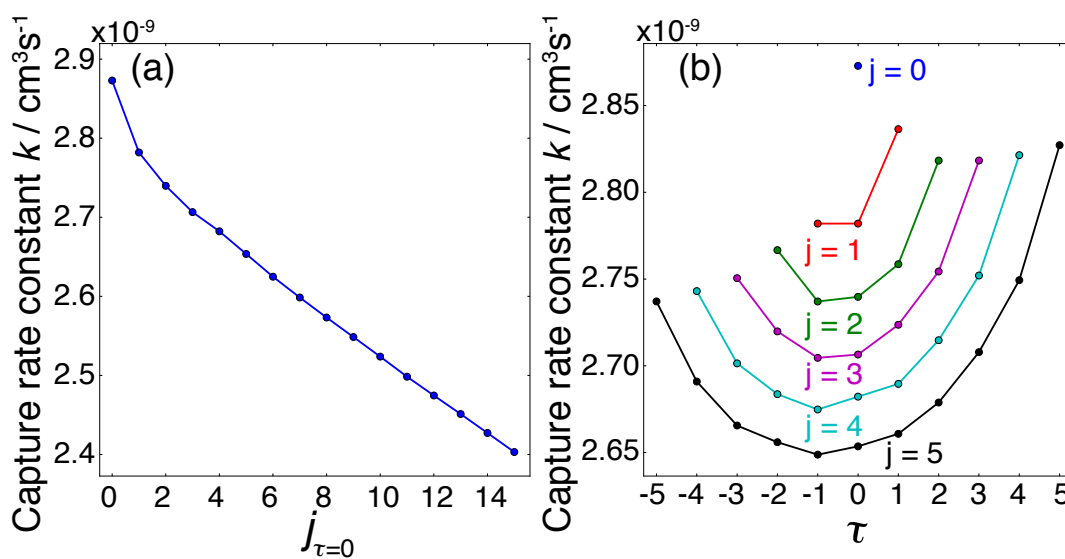


Figure 2.11: State-dependent capture rate constants k for *cis*-3-aminophenol. (a) Dependence on rotational state $j(\tau = 0)$ for $j = 0$ to $j = 15$. (b) Dependence on the asymmetric-top quantum number τ for $j = 0$ to $j = 5$. Lines are drawn to guide the eye. See text for details.

We also investigated the dependence of the capture rate constants on the ro-

2. Reactions of spatially separated conformers of 3-Aminophenol with Ca^+

tational state of 3AP. As exemplified for the *cis*-conformer at the experimental collision energy in Figure 2.11 (a), the capture rates slightly decrease as j increases. Since the rotational temperature is about 1.1 K, about 90 % of the 3AP population is confined to the rotational states $j = 1 - 5$ for which the relative difference of the rate constants is < 10 %. Figure 2.11 (b) shows the dependence of the capture rate constant for the *cis* conformer on the asymmetric-top quantum number τ . The dependence is only weak over the range of states $j = 0 - 5$. By averaging over capture rate constants of all populated rotational states of 3AP at 1.1 K and for a collision energy of 0.123 eV, one obtains the effective capture rate constants $k_{2,cis} = 2.7 \times 10^{-9} \text{ cm}^3 \text{ s}^{-1}$ and $k_{2,trans} = 1.8 \times 10^{-9} \text{ cm}^3 \text{ s}^{-1}$ and their ratio $k_{2,cis}/k_{2,trans} = 1.5$. These values are in good agreement with the experimentally observed second-order rate constants for the reaction with Ca^+ in the excited ($4p$) state, see Section 2.4.4.

2.6 Summary and conclusions

In this chapter a new method for the characterization of conformer-specific chemical reactivities was presented. In a proof-of-concept study, the two conformers of 3AP were spatially separated in a molecular beam using the electrostatic deflector. Subsequently, the separated conformers reacted with a stationary target of Coulomb-crystallized, laser-cooled Ca^+ ions. Second-order rate constants for the reactions of the individual conformers with Ca^+ were obtained. The reaction rate for the *cis* conformer was found to be a factor of two larger than that for the *trans* conformer. A detailed analysis of the rate constants for the individual electronic states of Ca^+ showed that the observed reaction rates are dominated by the reaction of 3AP with electronically excited Ca^+ ($4p$). The reaction rates of 3AP with Ca^+ in its ($4s$) $^2S_{1/2}$ ground and ($3d$) $^2D_{3/2}$ excited states were found to be two to three orders of magnitude smaller. CaOH^+ and CaNH_2^+ were identified as the likely reaction products by resonant-excitation mass spectrometry.

The rate constant observed for the Ca^+ ($4p$) reaction channel was found to be close to the capture limit. The difference in the reactivities of the two conformers could be rationalized in terms of adiabatic-capture theory in very

good agreement with the experimental findings. Within the capture picture, the increased reaction rate for the *cis* conformer compared to the *trans* species is explained by the stronger ion-dipole long-range interaction which results in a larger capture cross section. The small reaction rates with Ca^+ in its ($4s$) and ($3d$) states indicate the existence of dynamic bottlenecks along the reaction path. Preliminary DFT calculations for the reaction of 3AP with Ca^+ on the ground state potential energy surface enabled a first characterization of possible reaction pathways. However, more extensive computations would be necessary to elucidate the short-range dynamics in all three reaction channels probed in the present experiments.

The presented technique of combining electrostatic conformer selection with highly sensitive Coulomb-crystal methods will enable the study of conformational effects in a range of ion-molecule reactions. Electrostatic conformer separation is applicable to a variety of polar molecules as long as their conformers exhibit appreciably different dipole moments. More advanced techniques for the separation of molecular species and individual quantum states using electric field manipulation have been reported and could be implemented in the current methodology [49, 52, 127–129]. For the ionic reaction partners, the generation of Coulomb crystals of sympathetically cooled ions allows the study of a wide range of atomic and molecular ionic species [95]. Moreover, the preparation of Coulomb crystals with molecular ions in selected internal quantum states has been recently accomplished [130, 131] so that simultaneous studies of conformational and state-specific effects are now within reach for a wide range of ion-molecule reactions.

Chapter 3

A new setup for conformer dependent ion-molecule reactions with an ion trap coupled to a time-of-flight mass spectrometer

3.1 Introduction

The development of molecular-beam machines coupled to linear quadrupole radiofrequency (RF) ion traps (LQT) has enabled the study of highly controlled ion-molecule reaction dynamics by allowing to select specific velocities, quantum states and conformations of the neutral molecules [47, 55, 72, 132, 133]. In the previous chapter an experiment to study the conformer-specific effects in the reaction between Coulomb crystals of laser cooled Ca^+ ions and spatially separated 3-aminophenol conformers was presented and discussed. The required resolution of one atomic mass unit (u), to distinguish between the two possible ionic reaction products CaOH^+ and CaNH_2^+ , was not achieved by resonance enhanced mass spectrometry (REMS). Ion-molecule reactions with large organic molecules can have several channels that lead to a multitude of product ion species. Thus, to study reactions of conformationally selected large organic molecules with atomic or molecular ions, a better mass resolution than achiev-

able with the previous setup is necessary.

To improve the resolution of the mass analysis and quantify the number of trapped ions, LQTs have been coupled to time-of-flight (TOF) mass spectrometers (MS) in several recent experiments.

Schowalter *et al.* developed a LQT where the extraction field is applied directly onto the trap electrodes [134]. This mass spectrometer featured a resolution of $m/\Delta m \approx 50$ and an improved version achieved $m/\Delta m \approx 500$ for trapped laser-cooled ions [135]. The trapping RF potential is switched off fast, just before the ions are ejected into the flight tube, requiring custom electronics to combine quickly switchable, high-amplitude RF and DC fields [136].

Deb *et al.* developed a "digital" ion trap from which Coulomb crystals of laser cooled and sympathetically cooled ions are ejected between square wave pulses. With this method, they were able to reach a mass resolution of $m/\Delta m \approx 90$ [137, 138]. Ni *et al.* reported a six-rod ion trap from which ions are ejected radially onto an MCP detector for photodissociation studies of HfF^+ [139]. Jyothi *et al.* developed a wire-electrode trap where the ions are ejected while the RF remains on. They observed a strong dependence of the ion flight time on the RF phase angle at the time of ejection leading to complex mass spectra which are difficult to interpret if more than one ion species are trapped and ejected [140]. In all of these experiments, the ions are ejected radially from the trap. Seck *et al.* coupled a LQT to a TOF-MS in which the ions are accelerated along the trap axis into the TOF-MS by applying a potential gradient using the endcaps of the ion trap [141]. The advantage of this setup is the separation of RF and high-voltage electrodes but the mass resolution seems limited.

For future studies of conformer dependent ion-molecule reactions, a new machine dedicated to these experiments was designed and built with a new LQT that is coupled to a TOF-MS. The ions are ejected radially using additional electrodes inside the trap. The trapping RF can be turned off prior to the ion ejection. Additional electrodes are installed below the trap to accelerate and focus the ions onto a MCP detector thereby greatly enhancing the mass resolution to $m/\Delta m \approx 700$. The new LQT-TOF-MS features a simple design with separate RF and ejection DC electrodes, thereby enabling operation with commercially available RF and DC electronics.

3. A new setup for conformer dependent ion-molecule reactions with an ion trap coupled to a time-of-flight mass spectrometer

Here, the setup of the new apparatus and results from the characterization of the new LQT-TOF-MS are presented. This chapter is split into two parts. In the first part, experiments are discussed in which the RF potential was turned off prior to the ion extraction into the TOF-MS. In the second part, experiments in which the RF potential was kept on during ion extraction are discussed.

3.2 TOF experiments with trapping RF turned off during ion ejection

3.2.1 Experimental setup

The molecular beam machine in the new setup is essentially identical to the one used in the 3-aminophenol experiment. Instead of an Even-Lavie valve a cantilever piezovalve with a 150 μm diameter nozzle was installed in the source chamber [142]. The source chamber is differentially pumped by two 1650 l/s turbomolecular pumps. The deflector chamber is pumped by a 500 l/s pump. The molecular beam is skimmed 15 cm and 27 cm after the nozzle by 2 mm and 1 mm diameter skimmers before entering the 15 cm long deflector and being skimmed again by a 1.5 mm diameter skimmer 1.3 cm after the deflector. The molecular beam machine is connected to the ion trap chamber with a flexible bellow and the distance from the end of the deflector to the ion trap center is 49.4 cm. See Figure 3.1 for a schematic of the beam machine, ion trap and vacuum apparatus.

Our new ion trap is a LQT with additional electrodes embedded for ion ejection into a time-of-flight mass spectrometer. The trap electrodes consist of stainless steel rods that are segmented into three parts with two outer electrodes (endcaps) of 20 mm length and a center segment of $2z_0 = 10$ mm length. The electrode diameter is 8 mm and the diagonal distance between electrode surfaces is $2r_0 = 14.63$ mm. Between the top and bottom pair of cylindrical electrodes two additional rectangular electrodes are mounted. These electrodes consist of two 0.5 mm thick stainless steel parts with a 50 mm long and 3 mm wide gap. A nickel mesh (Precision Eforming) with 90% transmission was clamped in between

3.2 TOF experiments with trapping RF turned off during ion ejection

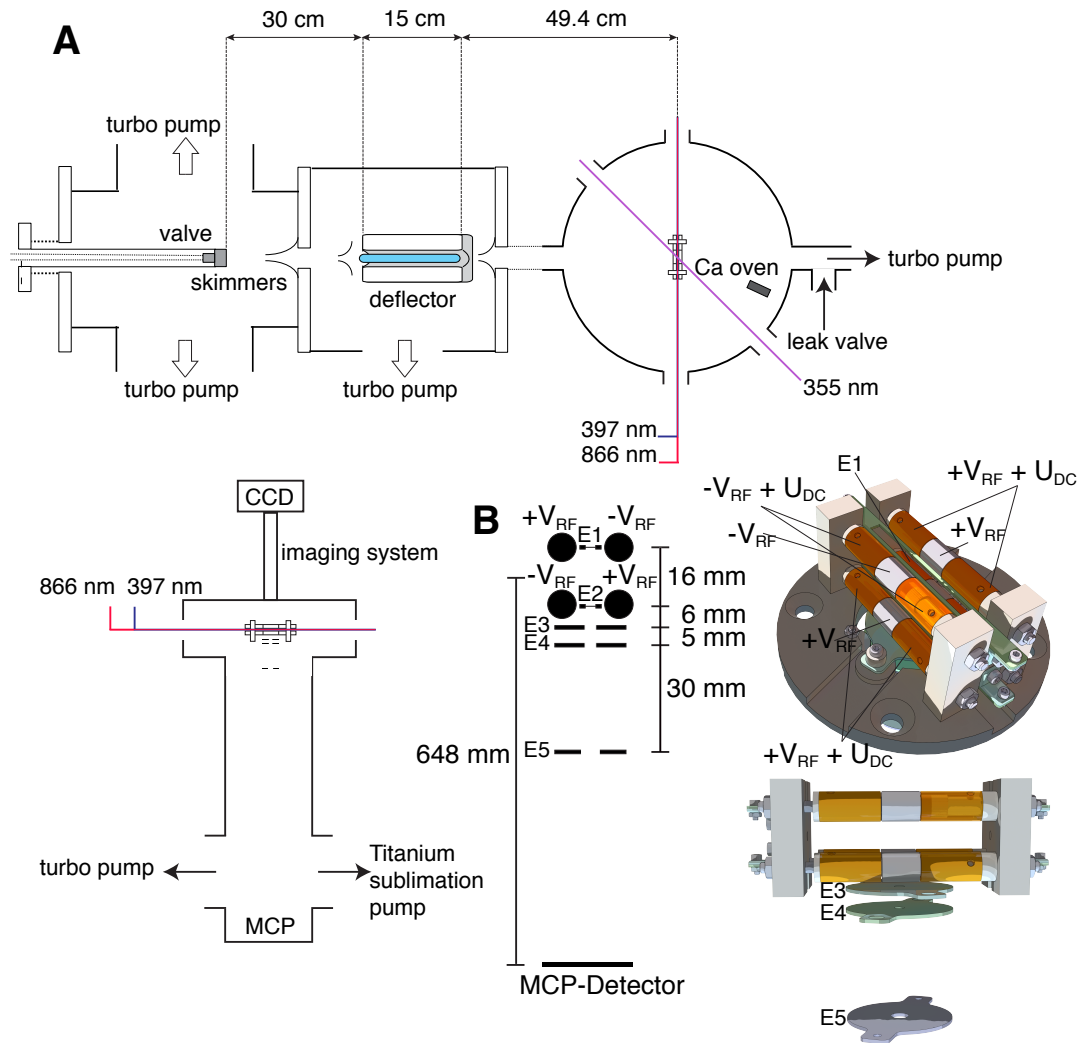


Figure 3.1: **A** Top and side view schematics of the molecular beam machine, the ion trap chamber and the time-of-flight tube. Laser beams at 397 nm, 866 nm and 355 nm used for laser cooling and photoionization of Ca are indicated. **B** Schematic of the ion trap, viewed along the trap axis. $+V_{RF}$ and $-V_{RF}$ denote the RF potentials applied to the electrodes. The static endcap potential is denoted with U_{DC} . E1 and E2 are the ion ejection electrodes. Electrodes E3 to E5 constitute the ion optics for post-ejection-acceleration. In the side-view 3D-drawing, the trap holder is omitted for clarity.

the two pieces and the frame was spot welded together to fix the mesh in place. All electrodes are held in place by two MACOR[®] pieces at both ends of the trap. Beneath the ion trap, three circular, 1 mm thick stainless steel electrodes

3. A new setup for conformer dependent ion-molecule reactions with an ion trap coupled to a time-of-flight mass spectrometer

are suspended from the trap holder to form the ion optics for the TOF-MS. The two top plates are separated vertically by 5 mm having each a 3 mm wide hole in the center and the distance from the trap center to the first plate is 14 mm. The third electrode is 30 mm below the second plate and has a 5 mm diameter hole in the center. The TOF-trap is mounted on a breadboard inside a spherical octagon vacuum chamber (Kimball Physics). A micro-channel-plate (MCP) detector (Photonis APD 2 APTOF) with an active diameter of 40 mm is mounted 648 mm below the trap center. The trap chamber and the flight tube are differentially pumped by 65 l/s and 550 l/s turbomolecular pumps connected to a 16500 l/h foreline pump. To efficiently reduce the hydrogen partial pressure, a titanium sublimation pump is connected to the vacuum system. The base pressure in this setup is $< 5 \times 10^{-10}$ mbar.

$^{40}\text{Ca}^+$ ions are generated by non-resonant multi photon ionisation of an atomic beam of Ca by the third harmonic (355 nm) of a Nd:YAG laser. The Ca beam is generated by a resistively heated Ca oven (Alvatec). The $^{40}\text{Ca}^+$ ions are laser cooled by two laser beams at 397 nm and 866 nm propagating along the trap axis [58]. The 397 and 866 nm light is generated by two external cavity-enhanced diode lasers that are frequency stabilized using a wavemeter (HighFinesse WSU 30) and a computer controlled feedback loop. A leak valve allows for the controlled admission of gas to the trap chamber. Coulomb crystals of $^{40}\text{Ca}^+$ are imaged using an electron multiplier charge coupled device (EMCCD) camera (Andor Luca) mounted on a microscope with a magnification of ~ 12.6 . The trap is driven by a commercially available radio frequency generator (Stahl-Electronics HF-DR 3.5-900 FL) which can be switched off within one RF cycle. The trap is operated on resonance at $\Omega = 2\pi \times 3.275$ MHz and peak-to-peak RF amplitude $V_{\text{RF,pp}} = 800$ V. The RF voltage is applied to all trap segments with opposite phases on adjacent rods and is mixed with typically 5 V DC voltage on the endcap segments. Ion extraction and acceleration potentials are applied by fast high-voltage switches (Behlke HTS 61-01-HB-C) with a 10-90% rise time of ~ 70 ns. The MCP signal is amplified by a homebuilt 26 dB amplifier and recorded on a 600 MHz oscilloscope (LeCroy Wavesurfer 64 MXs). The high-voltage switches and the data acquisition are triggered by a pulse generator (Quantum Composer 9520 series).

3.2 TOF experiments with trapping RF turned off during ion ejection

Our LQT-TOF-MS setup can be operated in two different modes. In low resolution mode, a high voltage pulse is applied only to the top extraction mesh. In high resolution mode, additional focusing potentials are applied to the ion optics below the trap after the ions have left the trap.

3.2.2 Experimental results and discussion

The electrostatic trap potential was modeled numerically in Simion 8.1 [69]. A three dimensional fourth-order polynomial was fitted to the numerical potential inside a $4 \times 4 \times 4$ mm³ cube around the trap center. The fitted potential was used as input for generating a force field in molecular dynamics (MD) simulations using the Protomol software [68, 74]. Figure 3.2 shows the stability diagram [60, 65] for a single $^{40}\text{Ca}^+$ ion in the trap as obtained from MD simulations for an ion at room temperature without laser cooling. If for a specific set of Mathieu a and q parameters [65] the ion was found in a volume of 1 mm³ around the trap center after 1000 RF cycles, it was considered to be stably trapped.

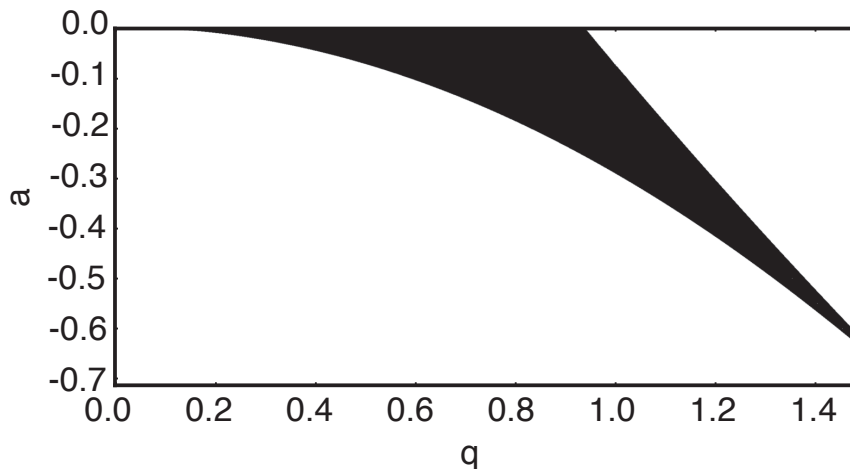


Figure 3.2: Stability diagram generated from MD simulations of a single Ca^+ ion at room temperature inside the ion trap. Trap frequency $\Omega = 2\pi \times 3.275$ MHz.

Figure 3.3 shows a 2D cut through the total time-averaged trapping potential (pseudo-potential [65] and static potentials) at the trap center and 1D cuts

3. A new setup for conformer dependent ion-molecule reactions with an ion trap coupled to a time-of-flight mass spectrometer

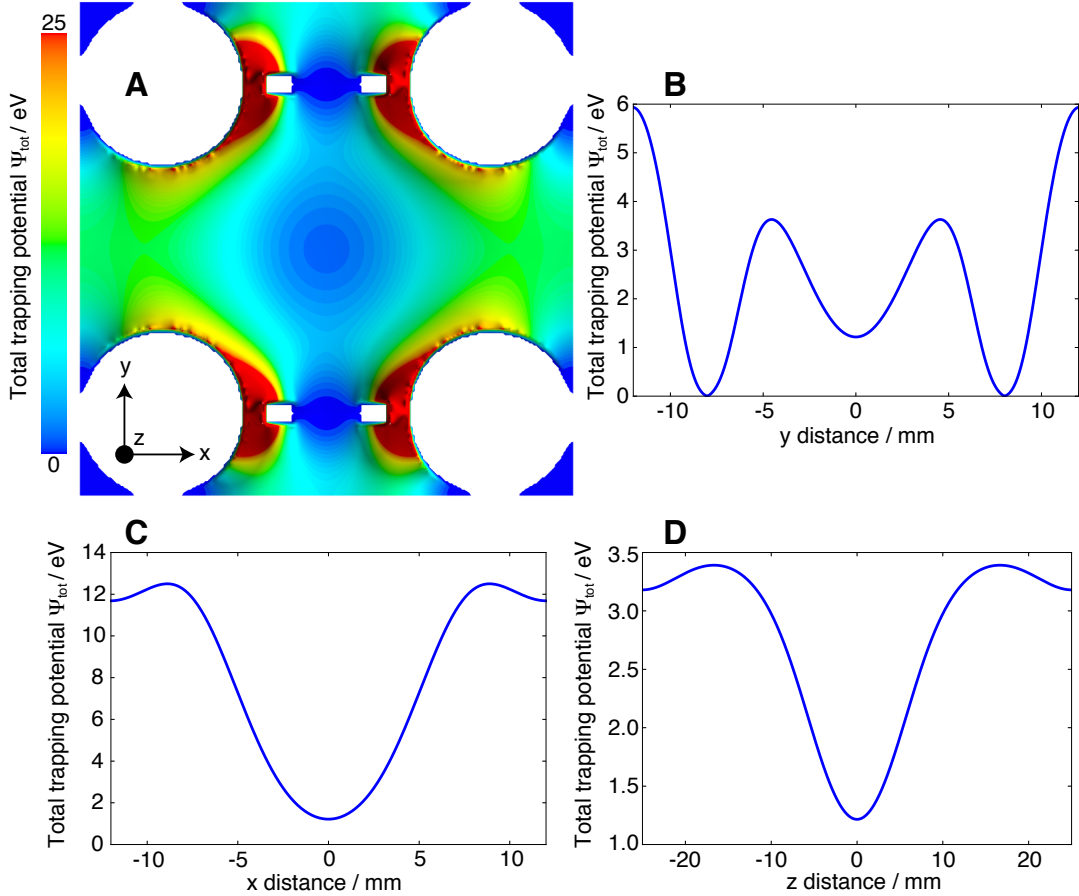


Figure 3.3: **A** Total trapping potential around the trap center for Ca^+ ions. The trap radio frequency is $\Omega = 2\pi \times 3.275$ MHz with $V_{\text{RF,pp}} = 800$ V amplitude and the DC endcap potential is 5 V. The extraction electrodes are grounded. **B** 1D cut through the potential along the y axis. **C** 1D cut through the potential along the x axis. **D** 1D cut through the potential along the z axis.

along the 3 principal axes. Due to the extraction meshes at the top and bottom of the trap, the potential gets distorted such that it becomes weaker along the y axis than along the x axis. The trap depth (defined as the difference between the minimum at the trap center and the maximum of the 1D potential cuts) is 11.29 eV in the x dimension and 2.43 eV in the y dimension at $\Omega = 2\pi \times 3.275$ MHz and $V_{\text{RF,pp}} = 800$ V.

This asymmetry in the potential leads to asymmetric Coulomb crystals. While ions lighter than Ca^+ gather at the trap center, heavier ions form surrounding

3.2 TOF experiments with trapping RF turned off during ion ejection

shells. The latter are more susceptible to the asymmetric trapping potential which results in their distribution being stretched along the y axis. The shape of the crystals can be controlled by applying a DC offset to the top and bottom mesh. Figure 3.4A shows the results of MD simulations of Coulomb crystals consisting of 100 Ca^+ ions and 100 ions with a mass of 80 u at different DC offsets applied to the extraction meshes.

Figure 3.4B shows measured low-resolution time-of-flight (TOF) spectra of mixed species Coulomb crystals consisting of Ca^+ , CaO^+ and CaOH^+ ions at different DC offsets applied to the extraction meshes. CaO^+ ions were created by leaking N_2O into the chamber to react with Ca^+ in the reaction: $\text{Ca}^+ + \text{N}_2\text{O} \rightarrow \text{CaO}^+ + \text{N}_2$ [143–145]. CaOH^+ was formed from Ca^+ reacting with residual water in the background gas [146]. The TOF signal at $12.9 \mu\text{s}$ arises from the $^{40}\text{Ca}^+$ ions. The signal around $15.5 \mu\text{s}$ is caused by CaO^+ and CaOH^+ ions. Changing the DC offset applied to the extraction meshes strongly influences the signal shape, especially for the heavy ions, and confirms the asymmetric crystal shapes predicted by the MD simulations. At -5 V DC offset the heavy ions form two separate distributions above and below the Ca^+ crystal core. These two ion packets arrive at the MCP detector at different times and give rise to two separate TOF signals. At positive offsets the crystal is squeezed along y such that heavy ions preferentially lie in the horizontal plane and reach the detector at the same time. Thus, they produce a single peak in the $+5 \text{ V}$ TOF trace. For the light ions at the center of the crystal, the trap asymmetry does not significantly influence the crystal shape. This is confirmed experimentally for the Ca^+ ions for which the peak width is not so strongly influenced by the DC offset. In conclusion, the trap asymmetry can be corrected by applying an appropriate DC offset to the extraction meshes. In the case of the artificial crystal consisting of 100 $\text{Ca}^+ + 100$ ions of mass 80 u, an offset of 1 V produces rotationally symmetric crystals according to the MD simulations.

The TOF spectra in Figure 3.4 exhibit a very low resolution with $m/\Delta m \approx 30$ for the Ca^+ signal. After turning off the trapping RF and waiting for $0.1 \mu\text{s}$, the ions were ejected from the trap by applying a $1.0 \mu\text{s}$ long 4000 V pulse to the top mesh.

Figure 3.5 shows the extraction potential inside the trap while 4000 V are

3. A new setup for conformer dependent ion-molecule reactions with an ion trap coupled to a time-of-flight mass spectrometer

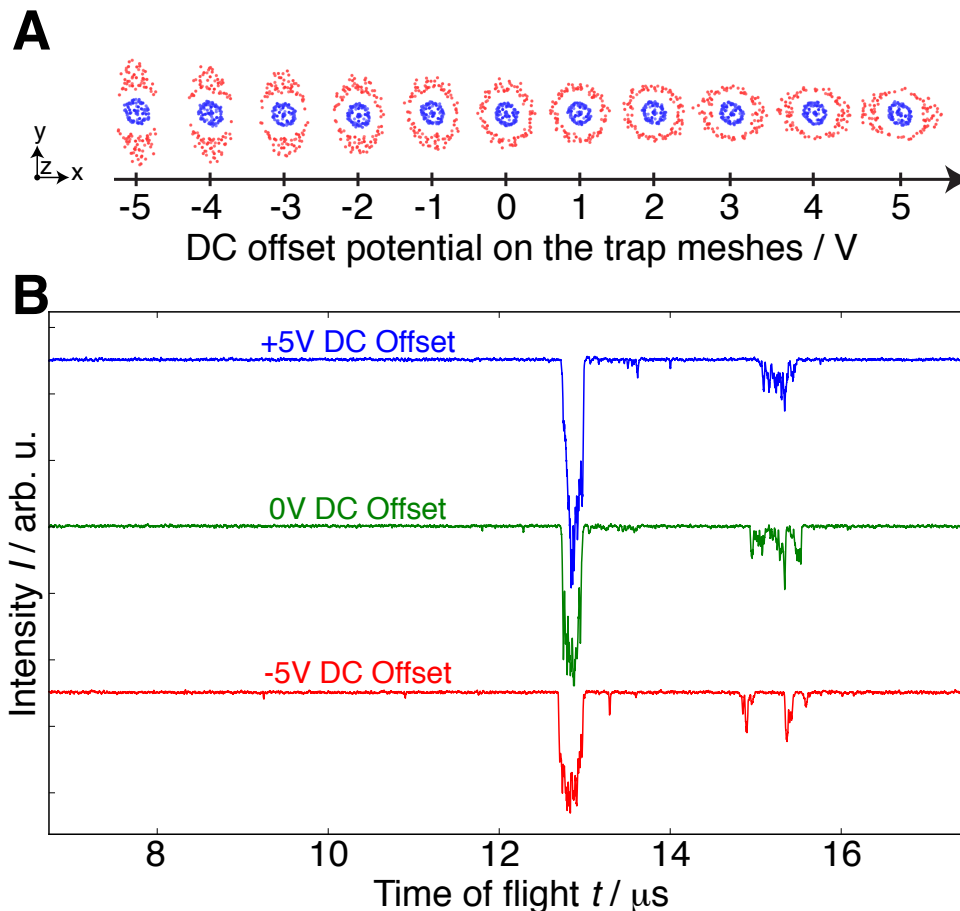


Figure 3.4: Molecular dynamics simulations of 100 Ca⁺ (blue) and 100 ions of mass 80 u (red) at different DC offset potentials applied to the extraction meshes. **B** Time-of-flight traces of Coulomb crystals consisting of Ca⁺, CaO⁺ and CaOH⁺ ions at different DC offset potentials applied to the extraction meshes prior to the ion extraction. Each trace is the average of 5 measurements.

applied to the top mesh. The extraction mesh is partially shielded by the trap electrodes which results in a weakening of the extraction field at the position of the ions. Moreover, the field is inhomogeneous. This leads to long flight times and broad peaks. Ideally, the TOF extraction region should resemble a Wiley-McLaren setup with a two-stage acceleration region for optimised space focusing with high resolution [93, 134, 137]. With the trap electrodes at ground potential during ion extraction, a Wiley-McLaren-type extraction region is not

3.2 TOF experiments with trapping RF turned off during ion ejection

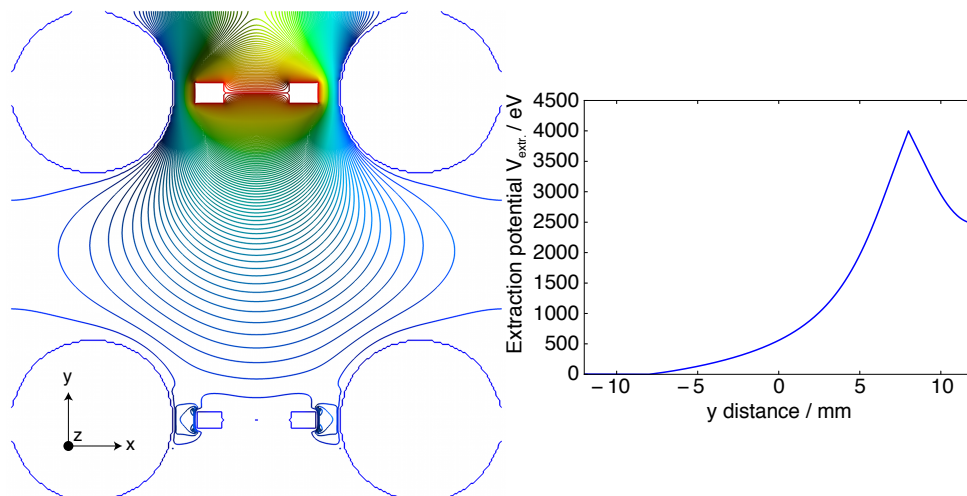


Figure 3.5: Extraction potential when 4000 V are applied to the top extraction mesh with all other electrodes grounded.

feasible. If high voltages are applied to the bottom extraction mesh the ions are lost from the trap along the x axis. For low potentials the ions are strongly defocused and do not reach the detector either.

To improve the resolution of the spectrometer, we employ a post-ejection-acceleration scheme in which the ions experience an additional accelerating potential after they have left the trap. Figure 3.6C shows the pulse sequence used to accelerate the ions. The RF voltage is turned off within one cycle (see Figure 3.6B) and after $0.1 \mu\text{s}$, a voltage of 4000 V is applied to the top extraction mesh. After a delay Δt , a voltage of 4000 V is pulsed to the top accelerator plate (E3) below the trap and a potential of 3200 V is applied to the middle accelerator plate (E4) while the third accelerator plate (E5) is held at ground potential (Fig. 3.6A). The potentials applied to E3 and E4 are generated by a single high voltage pulser with a home made voltage divider. The optimal acceleration delay Δt is highly mass dependent and only one species at a time can be efficiently focused. Accordingly, the delay has to be adjusted in order to optimize the resolution for a certain ion species.

Figure 3.7A shows the results of a scan of the acceleration delay for mixed Coulomb crystals consisting of Ca^+ , CaO^+ and CaOH^+ ions. The experiment

3. A new setup for conformer dependent ion-molecule reactions with an ion trap coupled to a time-of-flight mass spectrometer

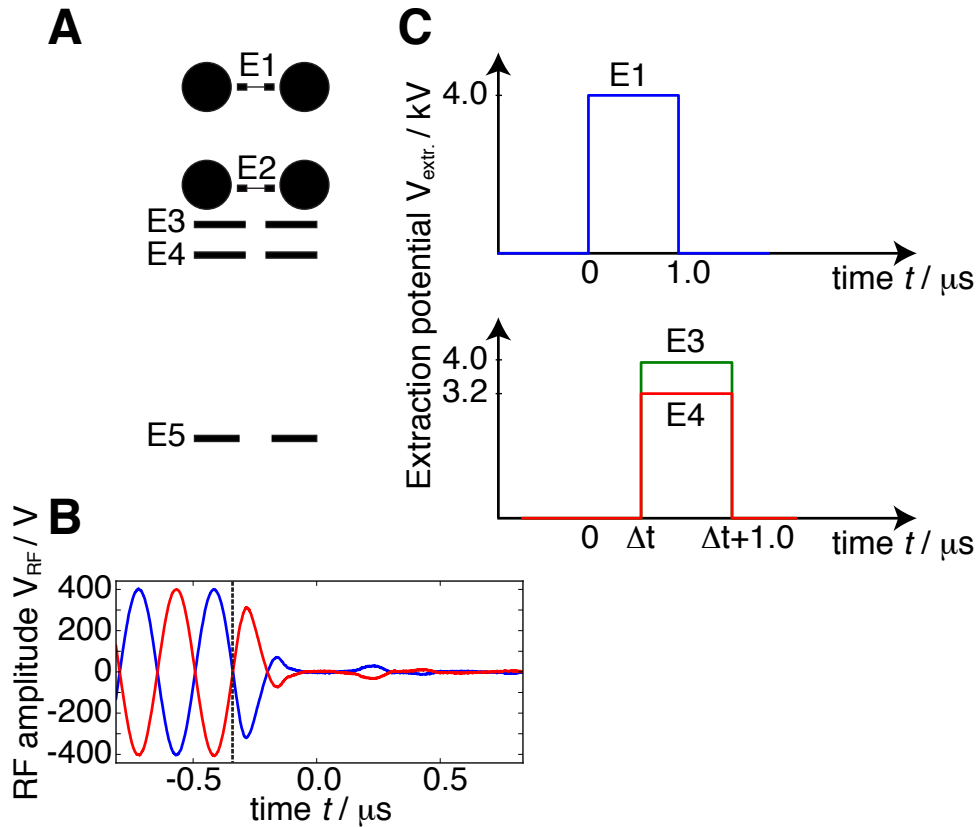


Figure 3.6: **A** Schematic representation of the ion trap with the extraction and acceleration electrodes labeled E1-E5. **B** Oscilloscope traces of both radio frequency phases at the time when the RF generator is switched off. The dashed line indicates the switch-off time. **C** High voltage pulse sequence to eject ions from the trap and accelerate them. The optimal value for Δt is dependent on the ion mass-to-charge ratio. See text for details.

was conducted in the following way: A Ca^+ Coulomb crystal was loaded and cleaned from heavy impurity ions by lowering the RF amplitude allowing all ions with mass > 40 amu to leave the trap. After ramping the RF amplitude back up to $V_{\text{RF,pp}} = 800$ V, N_2O was leaked into the chamber at a partial pressure of $\sim 8 \times 10^{-9}$ mbar to form CaO^+ ions. The CaO^+ ions were sympathetically cooled into the Coulomb crystal and the reaction was monitored by observing the disappearance of Ca^+ ions during the reaction. The reaction was stopped when about half of the Ca^+ crystal had reacted away. The Coulomb crystal

3.2 TOF experiments with trapping RF turned off during ion ejection

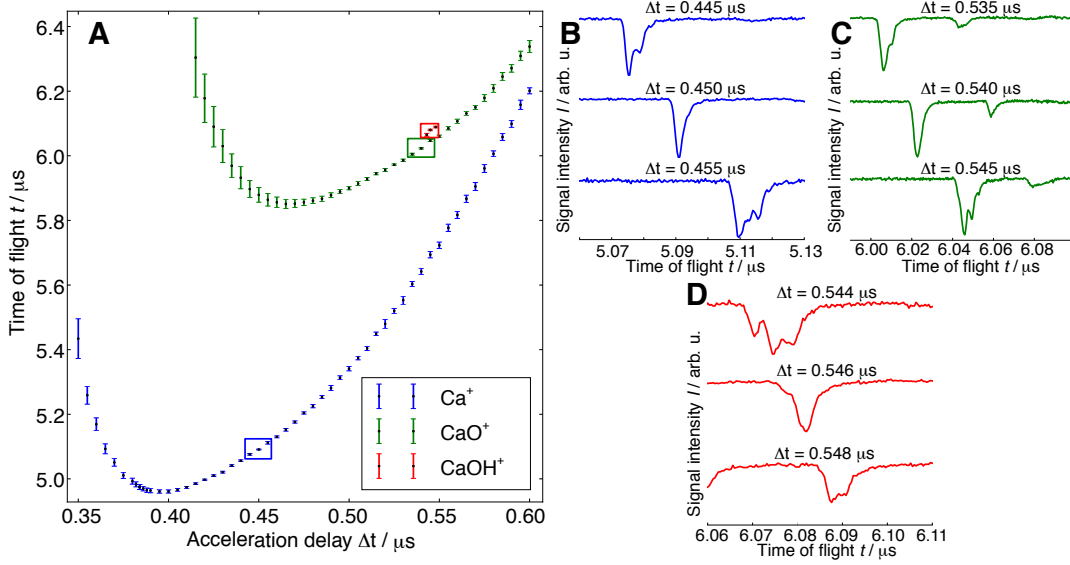


Figure 3.7: **A** Plot of the post-ejection-acceleration time delay versus the ion time-of-flight for 3 different ion species. Each data point corresponds to the peak center of an average over 5 TOF traces. The error bars give the FWHM of the peak from the average. **B** Averaged TOF traces at acceleration delays that produce the sharpest Ca^+ signal. Each trace is an average over 5 experiments. **C** Averaged TOF traces at acceleration delays that produce the sharpest CaO^+ signal. Each trace is an average over 5 experiments. **D** Averaged TOF traces at acceleration delays that produce the sharpest CaOH^+ signal. Each trace is an average over 5 experiments.

was then ejected into the TOF spectrometer and accelerated after a specific post-ejection-acceleration delay. Each data point in Figure 3.7 gives the peak center of an average over 5 TOF traces and the error bars correspond to the full width at half maximum (FWHM) of the averaged signal indicating the TOF resolution. If the post-ejection accelerator is switched on too early, the ions are repelled upwards and do not reach the detector. This is the case for the CaO^+ ions at accelerator delays $< 0.415 \mu\text{s}$. For all measured ions, we observed that the flight time is a convex function of the acceleration delay with a global minimum. The optimal delay that produces the strongest and narrowest signal is usually found slightly after the minimum of the curve. To analyze the TOF spectra and to extract the mass-to-charge (m/q) ratio of the measured ions, one needs to find the acceleration delay with the best focusing condition for each

3. A new setup for conformer dependent ion-molecule reactions with an ion trap coupled to a time-of-flight mass spectrometer

ion species. We assume that the optimal ion position inside the accelerator, at the time when it is switched on, is the same for all ionic species independent of their m/q ratio. This means we can calculate the mass of an unknown species from its flight time at the optimal accelerator delay compared to the TOF of another ionic species which serves as a reference at its own optimal accelerator delay.

To test this assumption, we measured the mass of the CaO^+ ions using $^{40}\text{Ca}^+$ as a reference. Figure 3.7B and 3.7C show the averaged TOF traces around the optimal acceleration delay for the Ca^+ (B) and CaO^+ (C) ions. Acceleration delays of $0.45 \mu\text{s}$ for Ca^+ and $0.54 \mu\text{s}$ for CaO^+ give the narrowest signals. The resolution $m/\Delta m$ is defined as $t/2\Delta t$ with Δt being the FWHM of the peak. At the ideal acceleration delay, the resolution is 878 for the Ca^+ signal and 669 for CaO^+ . The broadening of the signal at non-optimal delays is caused by a temporal jitter between the extraction mesh pulser and the accelerator pulser. Its effect is amplified if the ions are not at the correct position inside the accelerator at the time when the accelerator pulser is switched on.

Using the relation $t_{\text{CaO}^+}/t_{\text{Ca}^+} = \sqrt{m_{\text{CaO}^+}/m_{\text{Ca}^+}}$ with $m_{\text{Ca}^+} = 39.963 \text{ u}$ as the exact mass of ^{40}Ca , we calculate $m_{\text{CaO}^+} = 55.93(11) \text{ u}$ for the CaO^+ signal at the $0.54 \mu\text{s}$ acceleration delay. This mass agrees well with the exact mass of CaO (55.958 u). In figure 3.7C a weak signal at later flight times is observed. This signal is caused by CaOH^+ which is formed from a reaction of Ca^+ ions with water from the background gas [146]. To improve the signal to noise ratio and prove that this signal is from CaOH^+ , we reduced the N_2O pressure to $\sim 2 \times 10^{-9} \text{ mbar}$ and let the crystals react for a longer time which resulted in the formation of a larger amount of CaOH^+ . We scanned the acceleration delay and found the strongest and sharpest signal for a delay of $0.546 \mu\text{s}$. The mass of this signal is $57.04(10) \text{ u}$ which agrees well with the exact mass of CaOH (56.965 u). Table 3.1 gives an overview over all results from the post-ejection-acceleration TOF experiments.

An important application of this setup lies in the determination of the rates of ion-molecule reactions which necessitates quantitatively correct counts of ions. Previously, images of Coulomb crystals were used to calculate the crystal volume assuming that the crystal is rotationally symmetric in a standard LQT. From

3.2 TOF experiments with trapping RF turned off during ion ejection

Table 3.1: TOF post-ejection-acceleration results for Ca^+ , CaO^+ and CaOH^+ ions.

ion species	optimal delay / μs	t / μs	FWHM / ns	m/ Δm	mass / u	exact mass / u
Ca^+	0.450	5.091	2.9	878	-	39.963
CaO^+	0.540	6.023	4.5	669	55.93(11)	55.958
CaOH^+	0.546	6.082	4.2	724	57.04(10)	56.965

the change of the crystal volume over time, reaction rates could be extracted [47, 71, 132, 133]. This method is difficult to use when several ionic species are involved in a reaction and rates have to be determined for all channels. Only the Ca^+ ions are detected by fluorescence imaging and changes in the crystal shape might be very subtle so that even with the help of MD simulations, it might be difficult or impossible to determine which ions and how many have reacted. To improve this situation, we want to use the TOF mass spectrometer to monitor the reaction progress by ejecting the Coulomb crystal after a certain time. The integral over the MS signal of a specific ion is proportional to the number of trapped ions at the time of ejection.

To test whether we can use our spectrometer to quantify the number of ions in the trap, we measured TOF spectra of Ca^+ Coulomb crystals of different sizes and integrated over the Ca^+ signal. The crystal sizes were deduced from the crystal images. Figure 3.8A shows the results of this experiment. The crystal size linearly correlates with the integrated MCP signal for all tested crystal sizes. These experiments were done with the TOF-MS in low resolution mode by only using the top extraction mesh. We repeated this experiment with the post-ejection-acceleration switched on and observed the same linear relationship between the crystal size and the integrated detector signal (Fig. 3.8B).

To show that we can measure rate constants with this setup, we observed the reaction of Ca^+ ions with N_2O and determined the rate constant. Coulomb crystals of Ca^+ were prepared and N_2O was leaked into the vacuum chamber at varying partial pressures. After a certain time, the Coulomb crystal was ejected into the TOF-MS which was operated in low resolution mode. This reaction can be treated with pseudo-first order kinetics since the N_2O is available in large excess. For pseudo-first order kinetics, the integrated rate law

3. A new setup for conformer dependent ion-molecule reactions with an ion trap coupled to a time-of-flight mass spectrometer

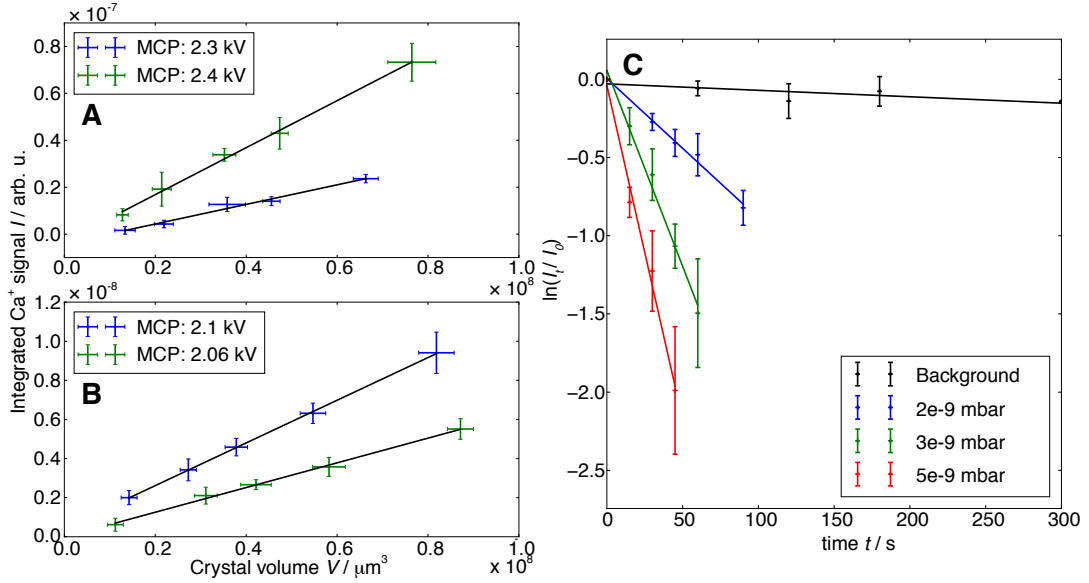


Figure 3.8: **A** Plot of Ca⁺ Coulomb crystal size versus the integrated MCP signal. The TOF-MS was operated in low-resolution mode. The crystal sizes were determined from images of the crystals. Each data point is the average of 5 experiments and the error bars correspond to one standard deviation. **B** Plot of Ca⁺ Coulomb crystal size versus the integrated MCP signal for the TOF-MS operated in high-resolution mode using the post-ejection-acceleration. Each data point is the average of 8-10 experiments and the error bars correspond to one standard deviation. **C** Pseudo-first order rate measurements for the reaction of Ca⁺ with N₂O at different N₂O pressures. Showing the reduction of Ca⁺ ions as measured with the TOF (see text for details). Each data point is an average of at least 5 measurements with the exception of background measurements with $t > 60$ s (3 experiments per point). The error bars correspond to one standard deviation.

$\ln(I_t/I_0) = -kN_{\text{N}_2\text{O}}t$ holds, where I_t and I_0 are the reactant signals at time t and $t = 0$, respectively, k is the bimolecular rate constant and $N_{\text{N}_2\text{O}}$ is the N₂O density. To determine I_t we integrate the Ca⁺ signal of the TOF trace, for I_0 we use the crystal size versus MCP calibration curve in Figure 3.8A and apply it to the image of the Coulomb crystal before the reaction. Figure 3.8C shows $\ln(I_t/I_0)$ versus t for 3 different N₂O partial pressures and a background reaction where no N₂O was admitted into the chamber. The data clearly shows a linear relationship and pseudo-first order rate constants can be obtained from

3.3 TOF experiments with trapping RF turned on during ion ejection

linear fits.

The second order rate constant calculated from this data is $k = 0.42(10) \times 10^{-9} \text{ cm}^3\text{s}^{-1}$ which is a factor of 3 to 10 larger than other values reported in the literature for this reaction [143–145].

To understand this discrepancy, one has to consider that the ions are laser cooled during the reaction. Thus, part of the Ca^+ ions are in electronically excited states from which they can react with different rates than from the ground state [71, 132, 133, 146]. To determine the ground state reaction rate, we repeated the experiment by blocking the 397 nm laser during the reaction to only have Ca^+ ions in the electronic ground state. To stop the reaction, we closed the leak valve and unblocked the 397 nm laser again to recrystallize the Coulomb crystal prior to its ejection into the TOF spectrometer. From this experiment, we determined a second order rate constant for the reaction of Ca^+ with N_2O of $5.49(32) \times 10^{-11} \text{ cm}^3\text{s}^{-1}$ which agrees with the value reported by Spears and Fehsenfeld [144] but is a factor of 2.4 to 2.9 lower than the values reported by Plane *et al.* and Lavrov *et al.* [143, 145].

To test if we lose ions from the trap due to elastic collisions with N_2O , we blocked the 397 nm laser and leaked Argon into the vacuum chamber for 90 seconds at the same partial pressures as in the N_2O experiment. The crystal volume did not shrink more as in a control experiment where no Argon was admitted into the trap chamber. Therefore, we rule out any significant ion loss from elastic collisions.

3.3 TOF experiments with trapping RF turned on during ion ejection

Our ion trap is designed so that the ions can also be ejected while the RF is applied. The results of experiments of the TOF-MS operated in RF-on mode are presented in the following section.

3. A new setup for conformer dependent ion-molecule reactions with an ion trap coupled to a time-of-flight mass spectrometer

3.3.1 Experimental setup

For ion extraction with the RF potential applied, a slightly different setup was used. The molecular beam was not connected and the small 65 l/s turbomolecular pump was also not installed. The trap was identical but the high-voltage cables for the extraction electrodes and ion optics (E1-E4) were fed through a feedthrough in the middle of the ion flight tube. The cables were unshielded Kapton[®] insulated copper wires which necessitated short high-voltage pulses to prevent deflection of the ions perpendicular to the TOF-MS direction. The wiring was optimized later for the experiments in which the RF was turned off prior to ion ejection. The HV wires now consist of Kapton[®] insulated coaxial cables that do not run through the flight tube.

The RF was generated by a homebuilt resonant self oscillating circuit operating at $\Omega = 2\pi \times 3.2$ MHz. To extract the ions in synchronization with the RF potential, an antenna was installed inside the RF generator. The signal generated by the antenna was in phase with one of the RF phases (see Figure 3.9) and was fed into the trigger input of the pulse generator. When the pulse generator was armed, it triggered the high voltage pulse sequence and the data acquisition on the falling edge of the RF antenna signal at a threshold of 0.8 V.

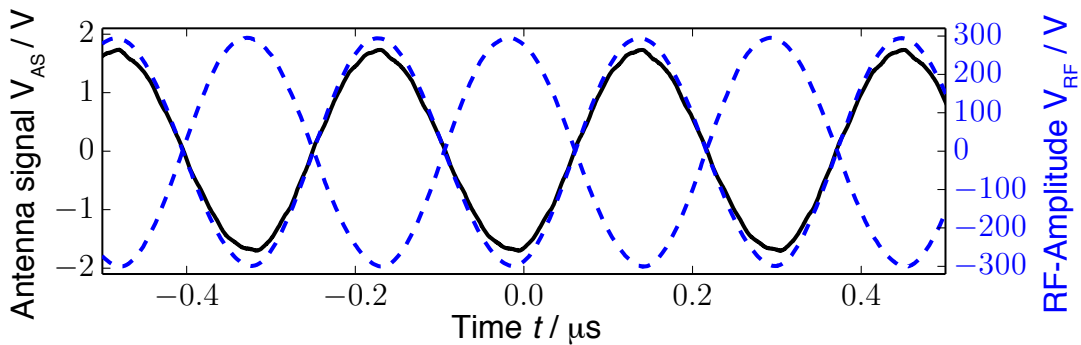


Figure 3.9: Oscilloscope traces of both RF phases and the RF-antenna signal used for triggering the HV pulsers in synchronization with the RF potential

3.3 TOF experiments with trapping RF turned on during ion ejection

3.3.2 Experimental results and discussion

To characterize the time of flight spectrometer, all measurements were done with Coulomb crystals of equal size at $\Omega = 2\pi \times 3.2$ MHz RF frequency and $V_{\text{RF,pp}} = 600$ V RF amplitude. The trap endcap potential was 5 V and the crystals were axialised before ejection into the flight tube. To find the best settings for ion ejection, the HV pulser for the top extraction mesh was set to 4 kV and the time delay between the trigger signal generated by the RF antenna and the HV pulse was scanned to extract the ions at different RF phase angles (Φ_{RF}). The strongest signal was observed for a delay of $0.04 \mu\text{s}$ (see Figure 3.10B).

Each datapoint in Figure 3.10B is the average of 24 traces that were all numerically integrated between $12.5 \mu\text{s}$ and $13.2 \mu\text{s}$. The error bars are large due to the fact that $\sim 50\%$ of all experiments were unsuccessful and did not yield any signal. The best signal and the largest success rate with 15 out of 24 experiments giving a strong signal, was achieved with a delay of $0.04 \mu\text{s}$. This delay corresponds to a RF phase angle close to 0 with $V_{\text{RF}} \approx 0$ V (see Figure 3.10C). With the exception of the RF phase angle dependence measurements, all Coulomb crystals were ejected with an extraction delay of $0.04 \mu\text{s}$. The right panel of Figure 3.10C shows how both RF phases are disturbed by the HV pulse applied to the top extraction mesh. This creates a beat on the RF amplitude V_{RF} which oscillates with a frequency of approximately 1 MHz and a maximum amplitude of ≈ 40 V. The beat decays fast and after 3 to 4 μs the RF is stable again.

Figure 3.11 shows the average of 50 TOF traces of mixed Ca^+/CaO^+ Coulomb crystals, measured with the TOF-MS in low-resolution mode. The TOF spectrum looks very similar to the low-resolution spectra recorded with the RF switched off (see Figure 3.4). The main difference is that if the RF is kept on, not every crystal extraction gives a signal on the MCP and many experiments have to be averaged. As for the spectra recorded with the RF switched off before the ion extraction, the resolution is very limited. The first signal at $\sim 13 \mu\text{s}$ corresponds to the Ca^+ ions with a resolution of $m/\Delta m \approx 30$ and the second signal at $\sim 16 \mu\text{s}$ arises from the CaO^+ ions.

3. A new setup for conformer dependent ion-molecule reactions with an ion trap coupled to a time-of-flight mass spectrometer

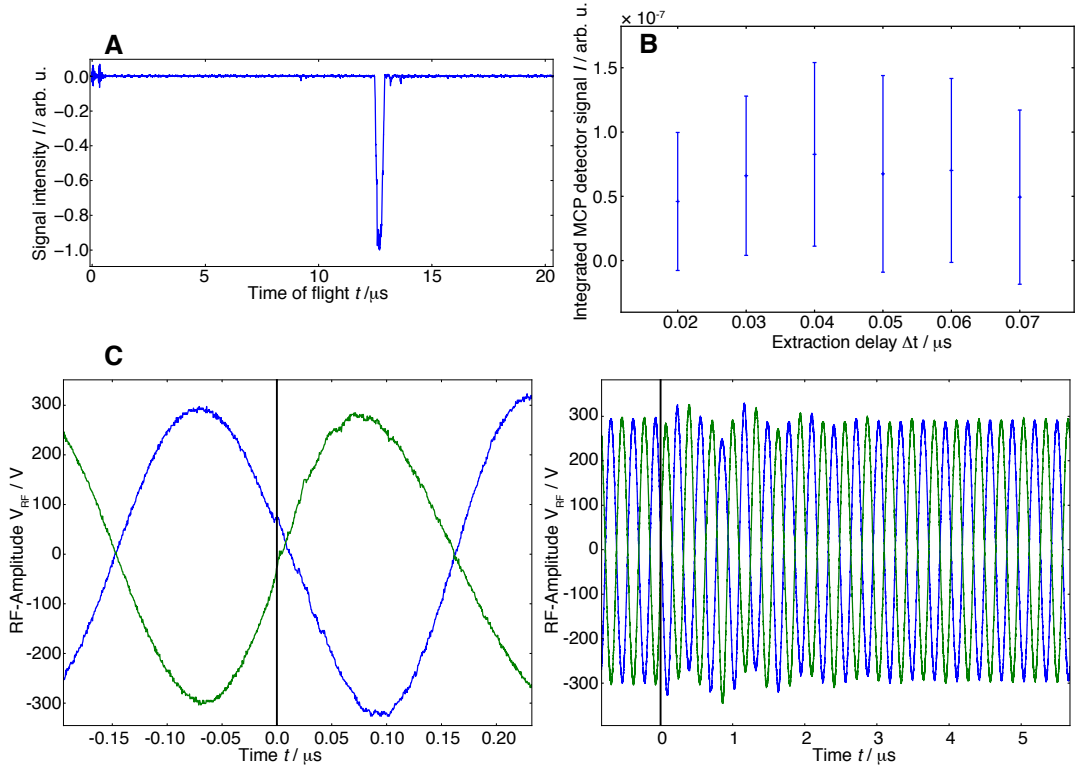


Figure 3.10: **A** Average of 48 TOF traces of Ca^+ Coulomb crystals. **B** Integrated MCP signal versus the delay of the RF antenna signal to the ion extraction. Each data point is the average over 24 measurements. The error bars correspond to one standard deviation. **C** Oscilloscope traces of both RF phases at the time when the HV pulse is applied to the top extraction mesh. The black line marks the time when the HV pulse is applied. The delay between the trigger signal from the RF-antenna and the HV pulse was $0.04 \mu\text{s}$.

To improve the resolution of the spectrometer a similar post-ejection-acceleration method as for the RF-off experiments was used. Due to the requirement for short HV pulses the post-ejection-acceleration pulse was only $0.2 \mu\text{s}$ long (see Figure 3.12). With these settings and a well chosen delay Δt every Coulomb crystal extraction gave a strong MCP signal.

Figure 3.13 shows the results of a post-ejection-acceleration scan. The measurements were done for pure Ca^+ Coulomb crystals (red traces) and mixed species Ca^+/CaO^+ crystals (blue traces). The Ca^+ signal is observable for all

3.3 TOF experiments with trapping RF turned on during ion ejection

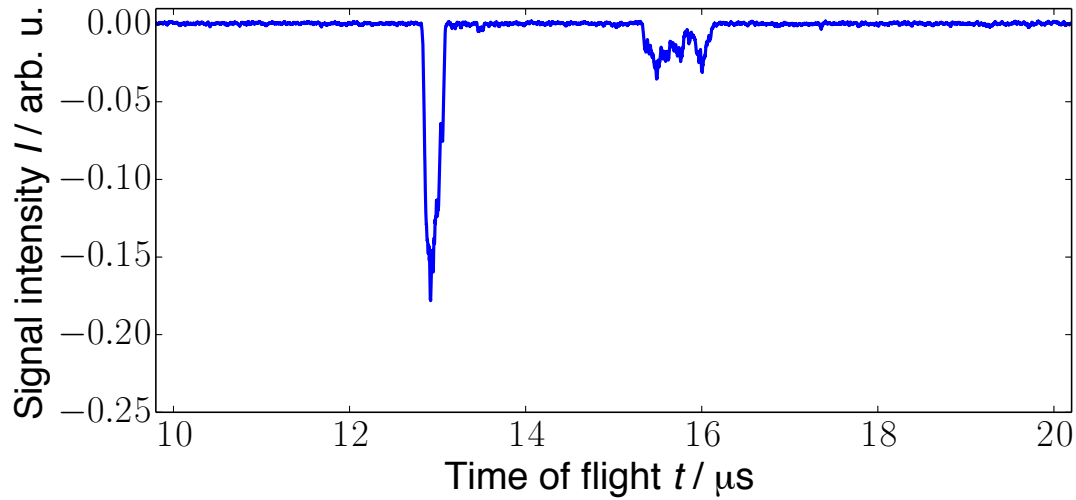


Figure 3.11: Average of 50 TOF traces of mixed Coulomb crystals consisting of Ca^+ and CaO^+ ions.

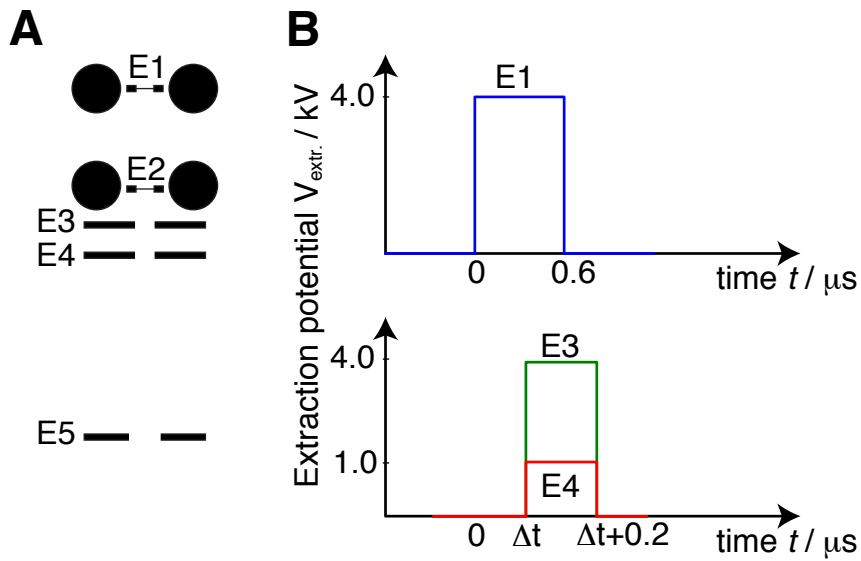


Figure 3.12: **A** Schematic representation of the ion trap with the extraction and acceleration electrodes labeled E1-E5. **B** High voltage pulse sequence to eject ions from the trap and accelerate them.

of the shown acceleration delays (Δt), but is best resolved at $0.38 \mu\text{s}$. With longer delays, the signal arrives at later times and is much broader since the

3. A new setup for conformer dependent ion-molecule reactions with an ion trap coupled to a time-of-flight mass spectrometer

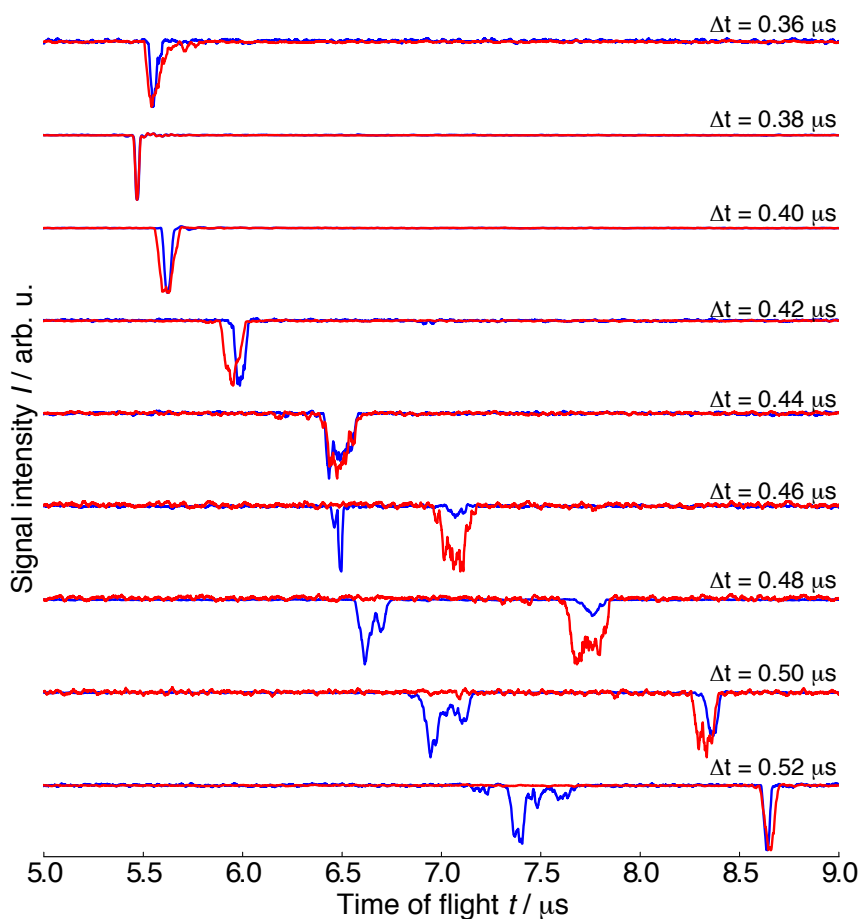


Figure 3.13: Test of the post-extraction acceleration with 4 kV on the first and 1 kV on the second plate. Each trace is an average of 5 measurements. The red traces are from experiments with pure Ca^+ crystals, the blue traces are from Ca^+/CaO^+ crystals. All traces are averages over 5 experiments and were smoothed with a running average over 50 data points. All traces were normalized to their strongest signal.

3.3 TOF experiments with trapping RF turned on during ion ejection

ions are not as efficiently accelerated towards the detector. At $0.42 \mu\text{s}$ a very weak CaO^+ signal can be observed at a flight time of $7 \mu\text{s}$. With a delay of $0.44 \mu\text{s}$ the Ca^+ and the CaO^+ signal overlap and with a $0.46 \mu\text{s}$ acceleration delay the CaO^+ signal arrives before the Ca^+ and is very sharp. The CaO^+ signal consists of two peaks that do not have the same intensity, probably due to asymmetric distribution of CaO^+ in the Coulomb crystal and one of the CaO^+ ion packets being more efficiently accelerated towards the detector. Analogous to the m/q determination explained in the RF-off experiments, the flight times of the signals with the best resolution were used to calculate the CaO^+ mass from the Ca^+ and CaO^+ flight times. The Ca^+ flight time is $5.47 \mu\text{s}$. For the flight time of CaO^+ the average of the two peaks ($6.47 \mu\text{s}$) was used. For the error calculation the full width at the base of the CaO^+ double signal (70 ns) was used, for the Ca^+ signal the FWHM (20 ns) was used. The calculated CaO^+ ion mass is $55.9(1.3) \text{ u}$. The expected value for the mass of CaO^+ is 55.96 u and is well within the error bars of the experimentally determined value. Although this method yields the correct mass, the resolution $m/\Delta m$ is an order of magnitude worse than for the RF-off experiments. The lower resolution partly arises by peak broadening caused by the complex ion extraction dynamics due to the RF potential. Another factor is that the post-ejection-acceleration pulse had to be short and the ideal focusing conditions were not met.

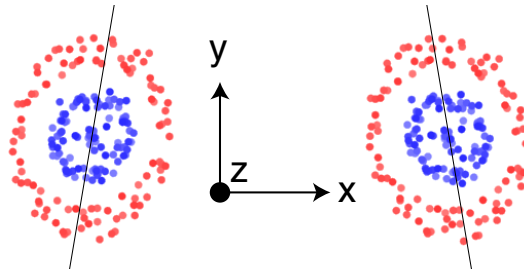


Figure 3.14: MD simulation of 100 Ca^+ and 100 CaO^+ ions, viewed along the trap axis. The two micromotion extrema are shown. The black lines indicate the vertical orientation of the Coulomb crystal.

3. A new setup for conformer dependent ion-molecule reactions with an ion trap coupled to a time-of-flight mass spectrometer

3.3.2.1 Ion extraction dynamics

In the following discussion the ion extraction dynamics for the RF-on ion ejection will be examined. The ions follow the RF phase in their micromotion [64, 65] which leads to a wobbling motion of the Coulomb crystal with two extrema as shown in Figure 3.14. To extract the ions out of the trap into the flight tube, a high potential is applied onto the top extraction mesh. The trapping field asymmetry and inhomogeneous extraction field (see Figures 3.3 and 3.5) will lead to different extraction dynamics for different ion masses. Consider a two component Coulomb crystal consisting of e.g. Ca^+ and another species X with $m(X) = 2 \times m(\text{Ca}^+) = 80 \text{ u}$. This Coulomb crystal will have a distorted structure with three almost separated ion packets. This asymmetric distribution of ions inside the trap leads to different extraction dynamics when the ions are ejected. The extraction potential that the ions feel is strongly position dependent along the y dimension (see Figure 3.5). This leads to different accelerations and flight times for the two ion packets of species X . The ions are most strongly influenced by the RF when they exit the trap, since they are flying close by the bottom trap electrodes. If the ejection pulse timing is optimized for one mass, e.g. for Ca^+ to give the strongest signal with the best resolution, this means that the Ca^+ ions are flying out of the trap when the RF amplitude is close to zero. For multi-species crystals this means that only one ion packet can exit the trap at the ideal conditions with $V_{\text{RF}} \approx 0 \text{ V}$, while all other ion packets experience a stronger deflection by the RF potential.

Ion trajectories in the TOF-MS were simulated using Simion [69]. Typically, Coulomb crystals of 200 ions were simulated in Protomol [74] and the MD simulation was stopped after equilibration at a certain RF phase angle. The ion positions and velocities at the end of the MD simulation were used to generate input files for the Simion simulations. In Simion the RF phase angle at the start of the simulation was matched to the phase angle at the end of the Protomol simulation and the ion extraction was started at time $t = 0 \mu\text{s}$ of the simulation. The trapping RF potential was kept on during the simulation and different extraction and acceleration methods were simulated, according to the settings of the pulse generator in the experiment. The oscillating V_{RF} offset after applying

3.3 TOF experiments with trapping RF turned on during ion ejection

the extraction potential, was not included in the simulations.

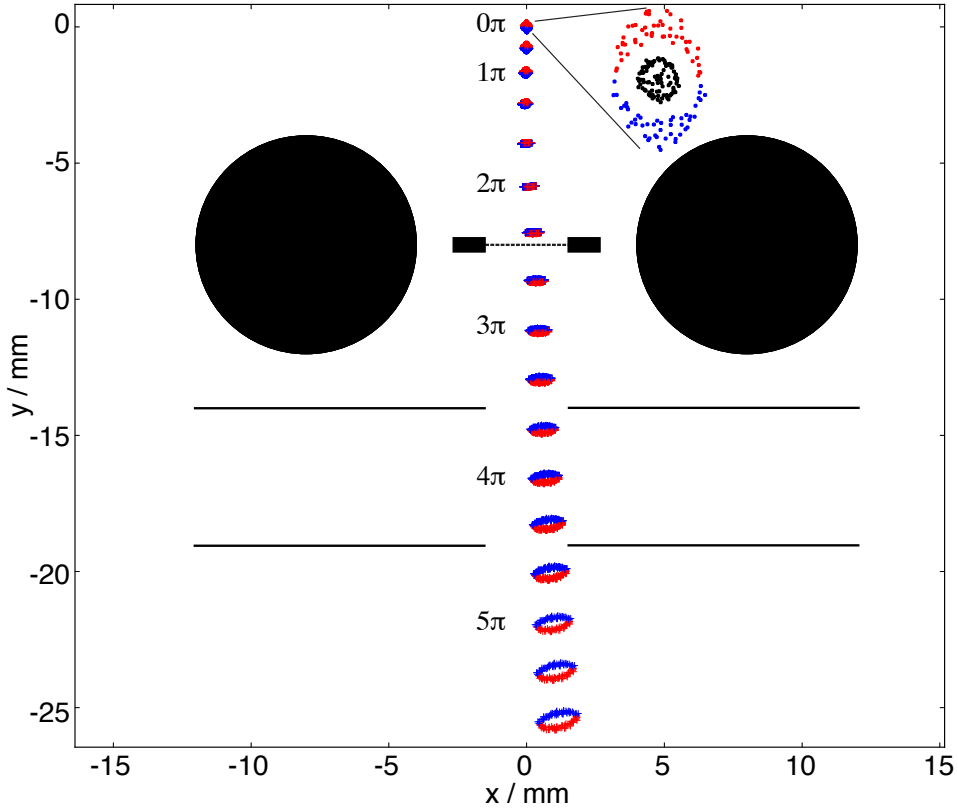


Figure 3.15: Snapshots from simulated ion trajectories for a Coulomb crystal consisting of 100 Ca^+ (black) and 100 ions of mass 80 u (red and blue) ejected from the trap by applying 4000 V on the top mesh at a phase angle of 0π . The Ca^+ ions are only shown in the inset and are omitted in the snapshots for clarity. The labels give the rf phase angle at the time of the snapshot next to it.

Figure 3.15 shows the simulated ion extraction dynamics for a 100 Ca^+ / 100 ions of mass 80 amu Coulomb crystal. The extraction field is switched on at a RF phase angle of 0π . Only the heavy ions are shown and color coded to show their respective position in the crystal at time zero when the extraction potential is switched on. The red ions are at the top of the crystal while the blue ones are at the bottom.

The ions at the top feel a larger extraction potential and are accelerated over a slightly longer distance than the ones at the bottom. The top ions pass the

3. A new setup for conformer dependent ion-molecule reactions with an ion trap coupled to a time-of-flight mass spectrometer

bottom ions after a short time and will arrive at the detector earlier. If the RF would be off, this would lead to a broad bi-modal peak or two separate signals. With the RF on during ion ejection, the signal distribution becomes much more complicated. The ions are influenced by the RF most strongly when they pass the two bottom trap electrode rods. They are deflected radially in the x dimension but also along the TOF dimension y since they feel the RF until they have passed the first electrode of the ion optics. Note that the ion optic electrodes do not have a shielding mesh which means that the ions can still be very weakly influenced by the RF after they have passed the post-ejection-acceleration stage. Due to the different velocities of the top ions with respect to the bottom ions they do experience slightly different deflection and acceleration or deceleration by the RF since they are not influenced by the RF for the same amount of time and experience different RF phase angles at identical positions along y . This results in a rotation of the heavy ion packet in Figure 3.15. These RF effects lead to complex spectra with multiple peaks for the same ionic species and make the interpretation of time of flight spectra difficult.

Figure 3.16 shows the results from Simion trajectory simulations where a Coulomb crystal containing 100 Ca^+ and 100 ions of mass 80 u was ejected from the trap at different RF phase angles. The vertical black lines on the second row symbolize the width of the detector and all trajectories that cross these lines belong to ions that do not reach the MCP. If the ions are extracted at non-optimal phase angles they are strongly deflected radially and most trajectories do not reach the MCP. Except for the simulation at a phase angle of $2/3 \pi$, a small kink in the CaO^+ ion trajectories after 49 mm can be observed. This is caused by trajectories that do not pass the hole of the third electrode (E5) of the post-ejection-acceleration stage.

The bottom panel shows simulated TOF traces for this Coulomb crystal extracted at five different RF phase angles. The time-of-flight for the ions strongly depends on the RF phase angle, which can be easily seen for the Ca^+ ions. For the heavy ions, the flight time also correlates with the phase angle, although, less obvious. Depending on the phase angle almost no heavy ions reach the detector and the signal shape can look dramatically different for different phase angles.

3.3 TOF experiments with trapping RF turned on during ion ejection

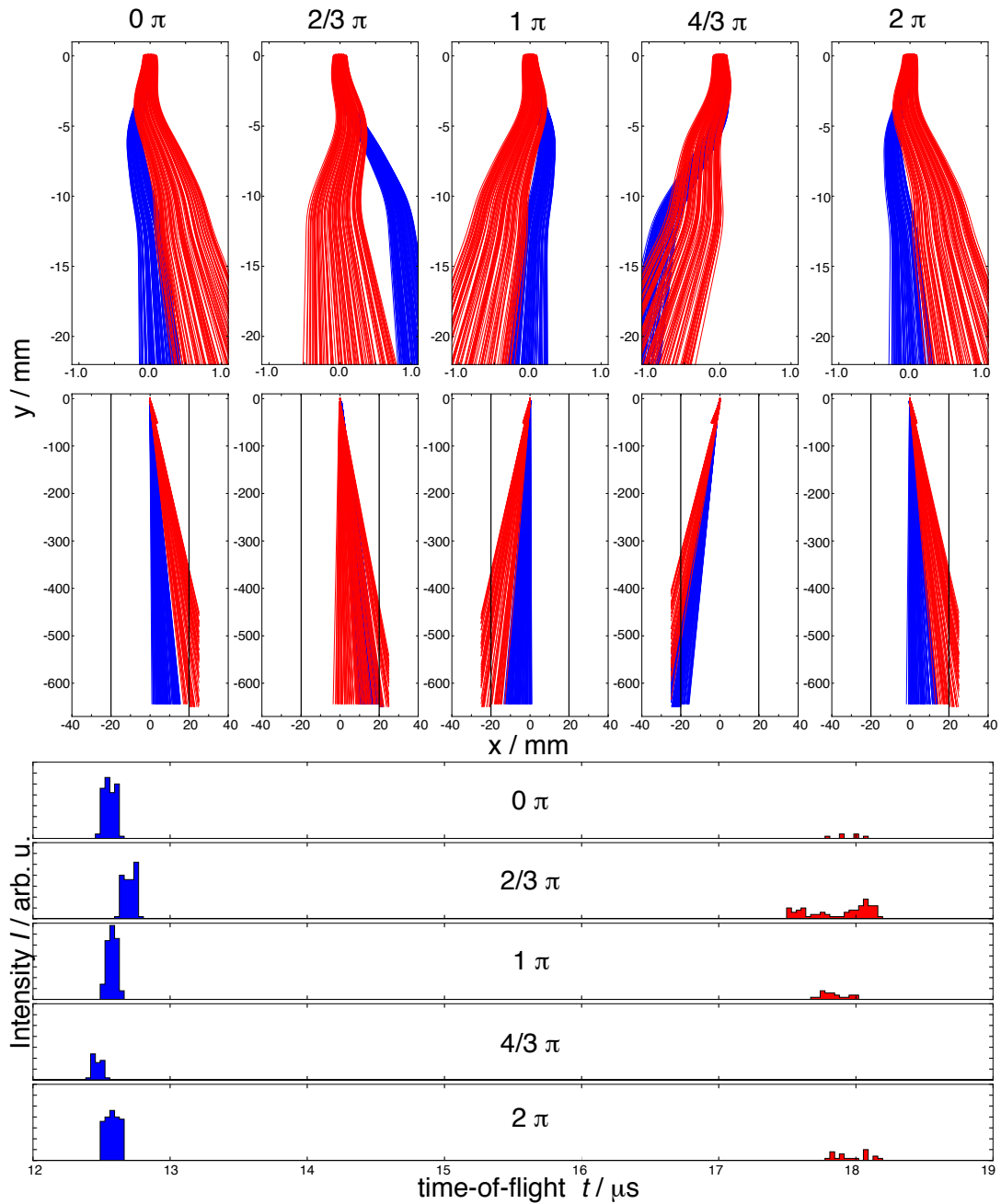


Figure 3.16: Simulated ion trajectories for a Coulomb crystal consisting of 100 Ca^+ (blue) and 100 ions of mass 80 u (red) ejected from the trap by applying 4000 V on the topmesh at different RF phase angles. Top row: trajectories in and close to the ion trap. Second row: trajectories for the whole flight length. The vertical black bars symbolize the width of the MCP detector. Bottom: histograms of the ion arrival time (bin width = 35 ns).

3. A new setup for conformer dependent ion-molecule reactions with an ion trap coupled to a time-of-flight mass spectrometer

The ion yield can be improved significantly by using post-ejection-acceleration. Due to the much larger velocity in the TOF direction y , more ions reach the MCP since the radial velocity component is much smaller and the deflection is not as prominent as in the case where the ions are only accelerated by the top extraction mesh. However, ions on trajectories that can not pass the holes in the ion optics are still lost. This means that the number of ions in the Coulomb crystal can not easily be determined by integration of the ion signal if the phase angle is not chosen carefully.

Figure 3.17 shows the integrated MCP signals for Ca^+ Coulomb crystals of different sizes. The ions were extracted from the trap and further accelerated using a lift post-ejection-acceleration method that will be described in detail later. Unlike in the experiments with the RF turned off, the crystal size does not show a perfect linear relationship with the integrated MCP signal. This is probably caused by ion loss during the ion extraction and post-ejection-acceleration.

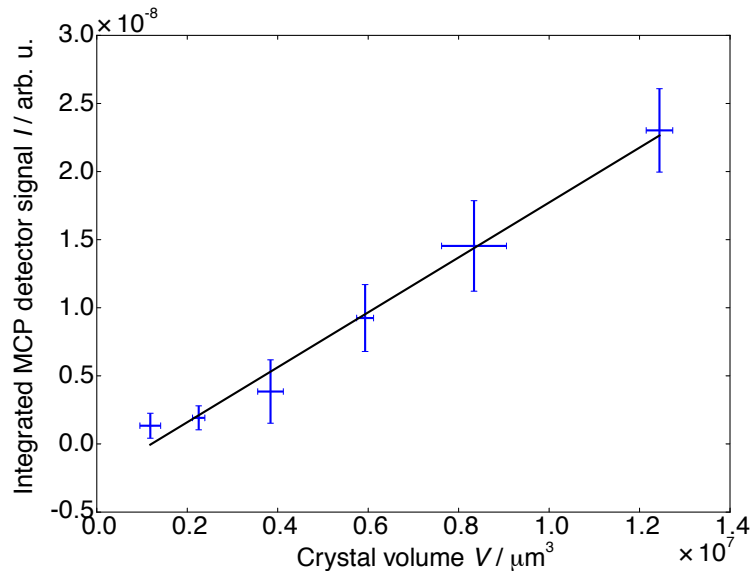


Figure 3.17: Plot of Ca^+ Coulomb crystal size versus the integrated MCP signal. The TOF-MS was operated with post-ejection-acceleration in lift-TOF mode. The crystal sizes were determined from images of the crystals. Each data point is the average of 10 experiments and the error bars correspond to one standard deviation. The black line is a linear fit to the data points.

3.3 TOF experiments with trapping RF turned on during ion ejection

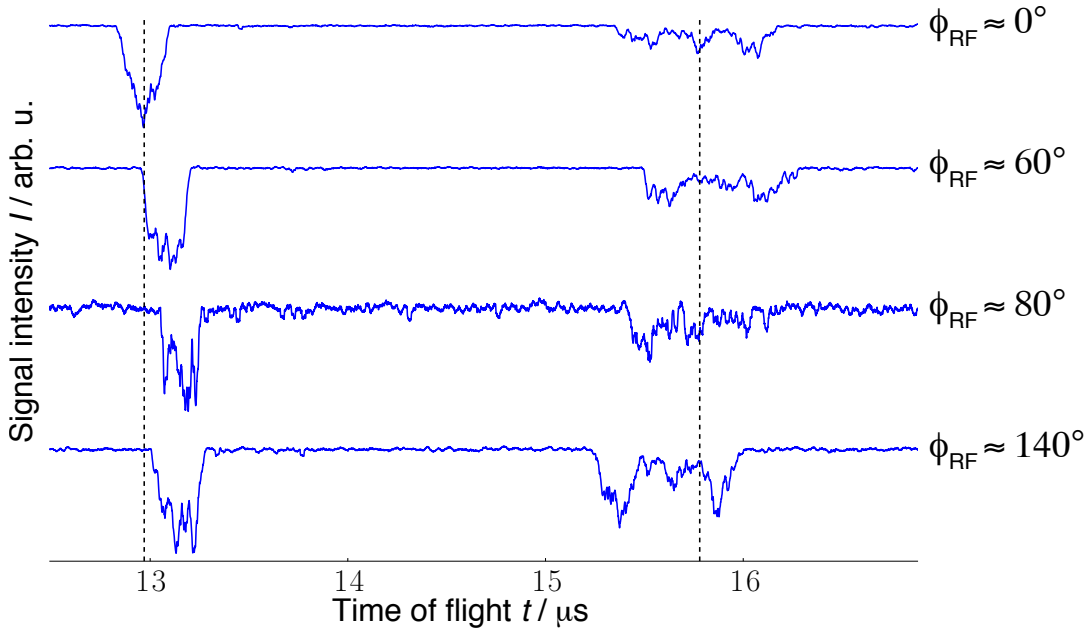


Figure 3.18: TOF spectra of mixed Ca^+/CaO^+ Coulomb crystals that were extracted at different RF phase angles. The TOF-MS was operated in low-resolution mode. Each trace is an average of 15 experiments. The dashed lines are guides for the eye.

Figure 3.18 shows the TOF traces of mixed species Coulomb crystals consisting of Ca^+/CaO^+ ions, extracted at four different RF phase angles. As it was seen in the Simion simulations, the ion arrival time and peak shape strongly correlates with the RF phase angle. At a phase angle of 60° , both species arrive at the detector later compared to the extraction with an angle of 0° . At 80° , the Ca^+ ions arrive even later but the CaO^+ ions arrive at the same time as for the experiment with a phase angle of 0° . At 140° the Ca^+ ions arrive later and the CaO^+ ions arrive earlier than in the case with $\Phi_{\text{RF}} = 0^\circ$. These phase angle dependent extraction dynamics render a straightforward interpretation and mass determination of low-resolution spectra impossible. For high-resolution spectra, the effect of the RF seems not as prominent and a correct m/q determination of CaO^+ ions was still possible for the post-ejection-acceleration experiments. However, to get a phase independent TOF spectrum one has to average over a full RF period.

3. A new setup for conformer dependent ion-molecule reactions with an ion trap coupled to a time-of-flight mass spectrometer

3.3.2.2 Post-ejection-acceleration using a lift-TOF-MS

In the post-ejection-acceleration measurements (Figure 3.13), the CaO^+ ion signal was split into two peaks with unequal intensity. The splitting is caused by the RF effects and the crystal asymmetry. The difference in signal intensity for the two peaks is likely caused by the post-ejection-acceleration only focusing one of the two CaO^+ ion packets well. The post-ejection-acceleration strongly depends on the ion position inside the accelerator at the time the acceleration potential is switched on. This can lead to distorted spectra, since not all ions of one species will gain the same kinetic energy. To improve this situation and to make sure all ions gain the same kinetic energy, a lift-TOF scheme, inspired by the MALDI LIFT-TOF/TOF reported by Suckau *et al.* [147], was tested for post-ejection-acceleration. In the lift-TOF, the potential on two electrodes is raised to the same value when the ions are in between them. The ions are "lifted" up onto a high potential energy and are accelerated and focused by additional electrodes after they have left the region between the lift electrodes. Since all ions are lifted to the same potential energy and later accelerated over the same distance, the gain in additional kinetic energy is equal for all ions and is independent of the ions original position inside the post-ejection-acceleration region. In this setup the potential lift was applied between the bottom extraction mesh (E2) and the first plate of the accelerator (E3). The lift pulse was $0.2 \mu\text{s}$ long and the applied potential was 4 kV. The delay (Δt) between extracting the ions by pulsing a 4 kV potential for $0.3 \mu\text{s}$ onto the top mesh and turning on the lift was varied to accelerate either the Ca^+ or CaO^+ ions. The potential on the second plate can be varied to focus the ions onto the detector but for all experiments this electrode was held at ground potential to get a strong electric field gradient between the two top plates of the accelerator for a maximum gain in kinetic energy. The lift was applied between E2 and E3 to allow for short HV pulses. Due to the two bottom trap electrode rods, the lift potential was inhomogeneous and the ions were disturbed by the RF during the potential lift. Unfortunately, the inhomogeneity of our lift region introduces again a position dependence in the post-ejection-acceleration.

3.3 TOF experiments with trapping RF turned on during ion ejection

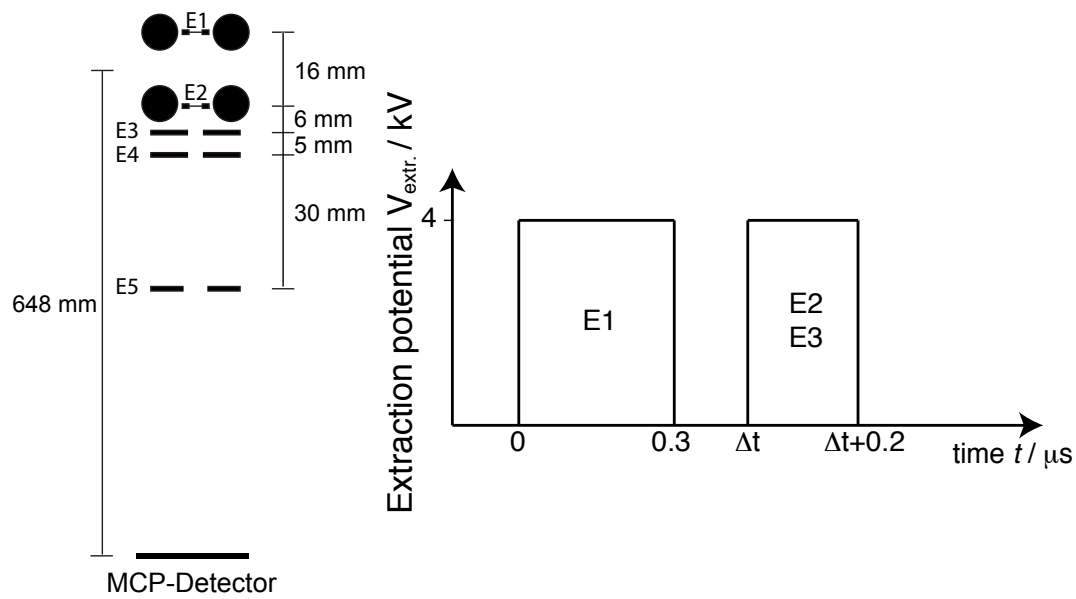


Figure 3.19: High voltage pulse sequence for the lift-TOF-MS.

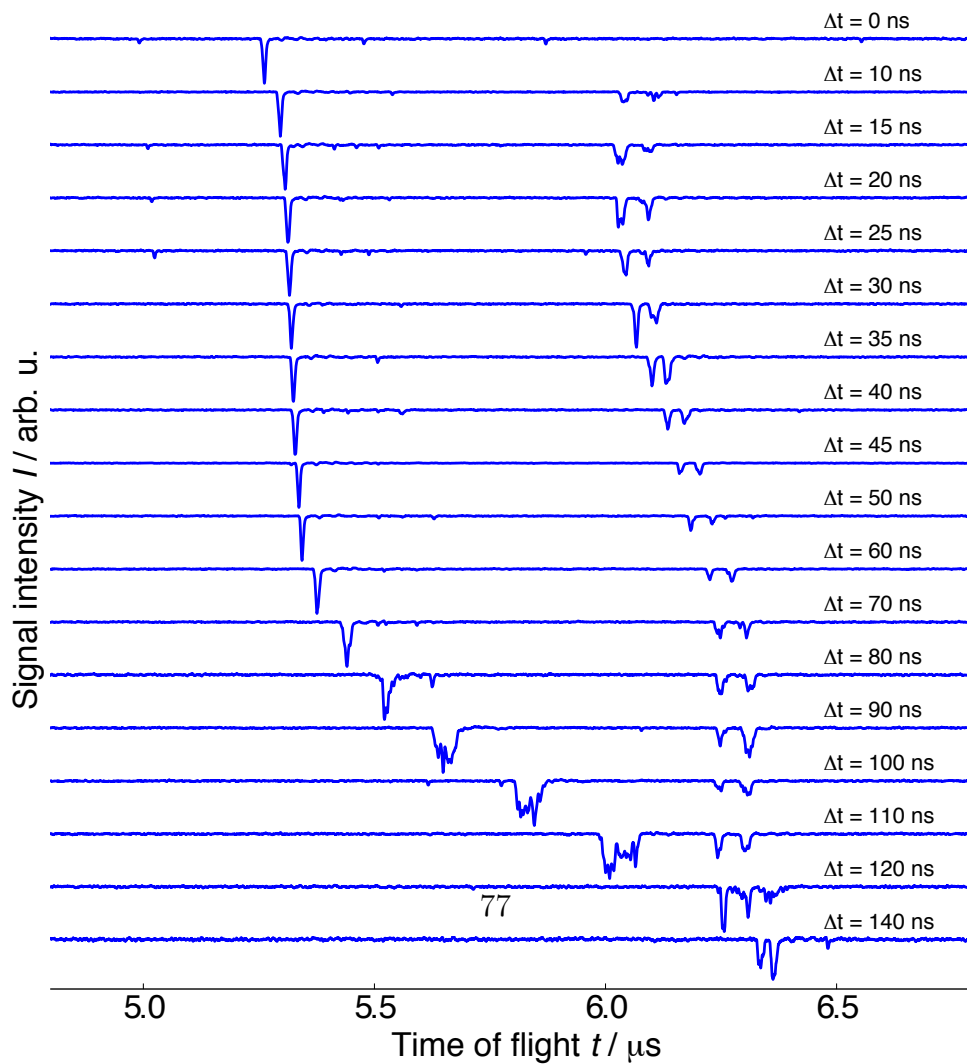


Figure 3.20: Lift-TOF spectra of mixed Ca^+/CaO^+ Coulomb crystals accelerated at different lift delays Δt . Each trace is an average over 3 experiments.

3. A new setup for conformer dependent ion-molecule reactions with an ion trap coupled to a time-of-flight mass spectrometer

Figure 3.20 shows the results of a test run of the lift acceleration for Coulomb crystals consisting of Ca^+ and CaO^+ ions. In an ideal scenario with a homogeneous potential lift region, the flight time of a certain ion species is independent of the lift delay Δt . All ions within a certain window of acceleration delays will have the same flight time since it does not matter for the ion at which point inside the lift region it is at the time when the lift is switched on, it will always gain the same amount of potential energy. Therefore, the gain of kinetic energy is also equal for all ions of one species, provided, the acceleration pulse length is long enough to allow the ions to be accelerated over the full acceleration distance after the lift region. Thus, a short delay and a long delay should give the same flight time if the ion was inside the lift region at the time when the lift was switched on. For Ca^+ this is the case for a delay between $\sim 15 - 50$ ns. The flight time is not perfectly independent of the delay probably due to the inhomogeneities in our potential lift region. For the CaO^+ signal the flight times are almost constant for a delay between 80 to 120 ns. For all experiments a delay of 30 ns was used if the Ca^+ ions were focused and a delay of 100 ns was used for the CaO^+ ions.

To get a RF phase independent TOF spectrum, the lift extraction scheme was used and the delay between the RF-antenna signal and the extraction pulse was scanned to cover one full RF period. The recorded RF phase angle specific traces are given in Figures 3.21 and 3.22.

3.3 TOF experiments with trapping RF turned on during ion ejection

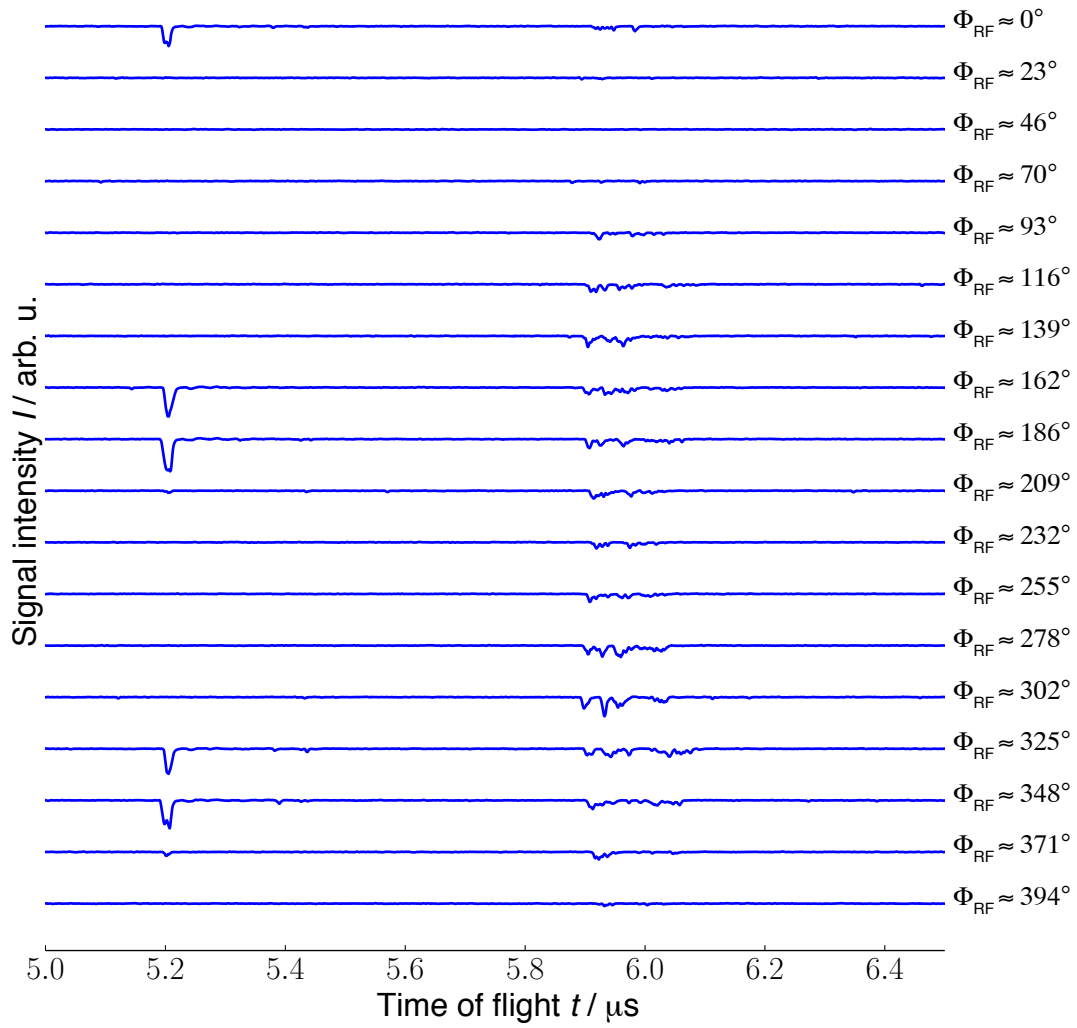


Figure 3.21: RF phase angle (Φ_{RF}) scan of Coulomb crystals consisting of Ca^+ and CaO^+ ions. Lift optimized for Ca^+ ions: delay $\Delta t = 30$ ns. Every trace is an average of 5 experiments

3. A new setup for conformer dependent ion-molecule reactions with an ion trap coupled to a time-of-flight mass spectrometer

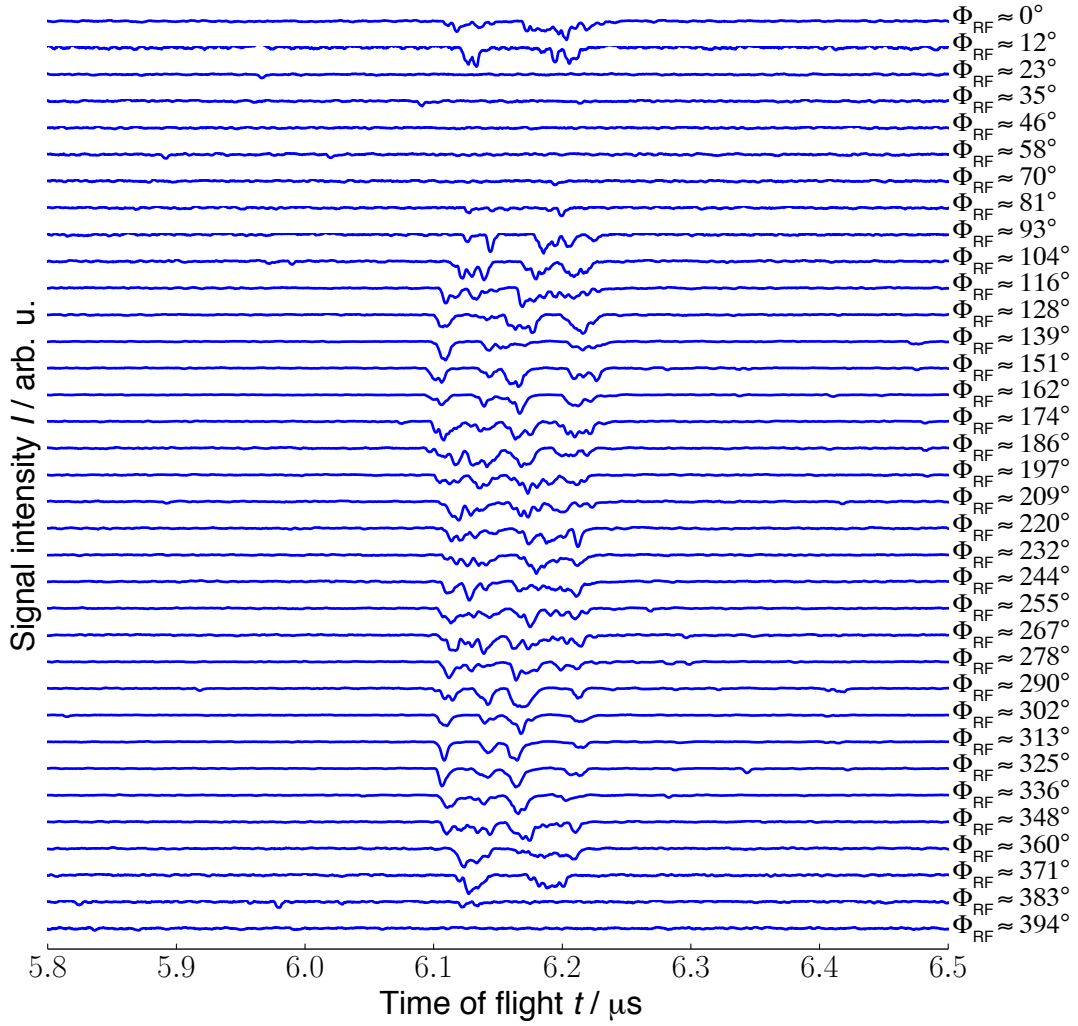


Figure 3.22: RF phase angle (Φ_{RF}) scan of Coulomb crystals consisting of Ca^+ and CaO^+ ions. Lift optimized for CaO^+ ions: delay $\Delta t = 100$ ns. Every trace is an average of 5 experiments

With the lift delay optimized for Ca^+ , a signal was observed only at a few phase angles close to the RF zero crossing. The difference in flight time is not significant, but the peak shape is either a single sharp peak or split into two overlapping peaks depending on the phase angle. In the CaO^+ measurements, the ion transmission is better and a CaO^+ signal can be observed for most phase angles. The signal shape and width strongly depends on Φ_{RF} and varies between a bimodal distribution of arrival times e.g. at $\Phi_{\text{RF}} = 0^\circ$ and 4 separate signals

3.3 TOF experiments with trapping RF turned on during ion ejection

e.g. at $\Phi_{\text{RF}} \approx 300^\circ$. The total flight time of the center of the signal is almost not influenced by Φ_{RF} . To determine the mass of CaO^+ , the following procedure was employed. For the Ca^+ flight time, the average of the flight times (center of the Ca^+ signal) of all successful traces was calculated to be $5.20 \pm 0.02 \mu\text{s}$. For the CaO^+ traces the center of the signal of each trace was determined and the average over all successful traces was calculated to be $6.16 \pm 0.1 \mu\text{s}$. The calculated value for the CaO^+ mass is then $56.1(1.9)$ u. This value is essentially the same as for the post-ejection-acceleration case reported above, although, with even larger error bars. The larger error is a result of the averaging over all RF phase angles where some angles gave a very broad CaO^+ signal. An important thing to note from the lift phase angle scan experiments is that the variation in actual flight time is small and it is not necessary to do a full phase angle scan and average over all angles to get the right result if the ions are accelerated further after the trap.

The lift-TOF scheme was also tested with the improved setup when the RF was turned off with the same settings as for the RF-on experiments. No delay range was found in which the ion flight time was independent of the acceleration delay (see Figure 3.23). This behavior is expected, since the field inside the lift potential region is inhomogeneous due to the presence of the trap electrodes. The field inhomogeneity defeats the purpose of the potential lift and introduces a position dependence, which gives rise to the increasing flight times of the Ca^+ ion signal without any delay range over which the arrival time is constant. In the experiments with the RF on, the potential lift seemed to work, yielding a nearly constant flight time over a certain delay range. This was probably caused by an averaging of the position dependence in the lift region, due to the different phase angles of the RF at the different acceleration delays.

3. A new setup for conformer dependent ion-molecule reactions with an ion trap coupled to a time-of-flight mass spectrometer

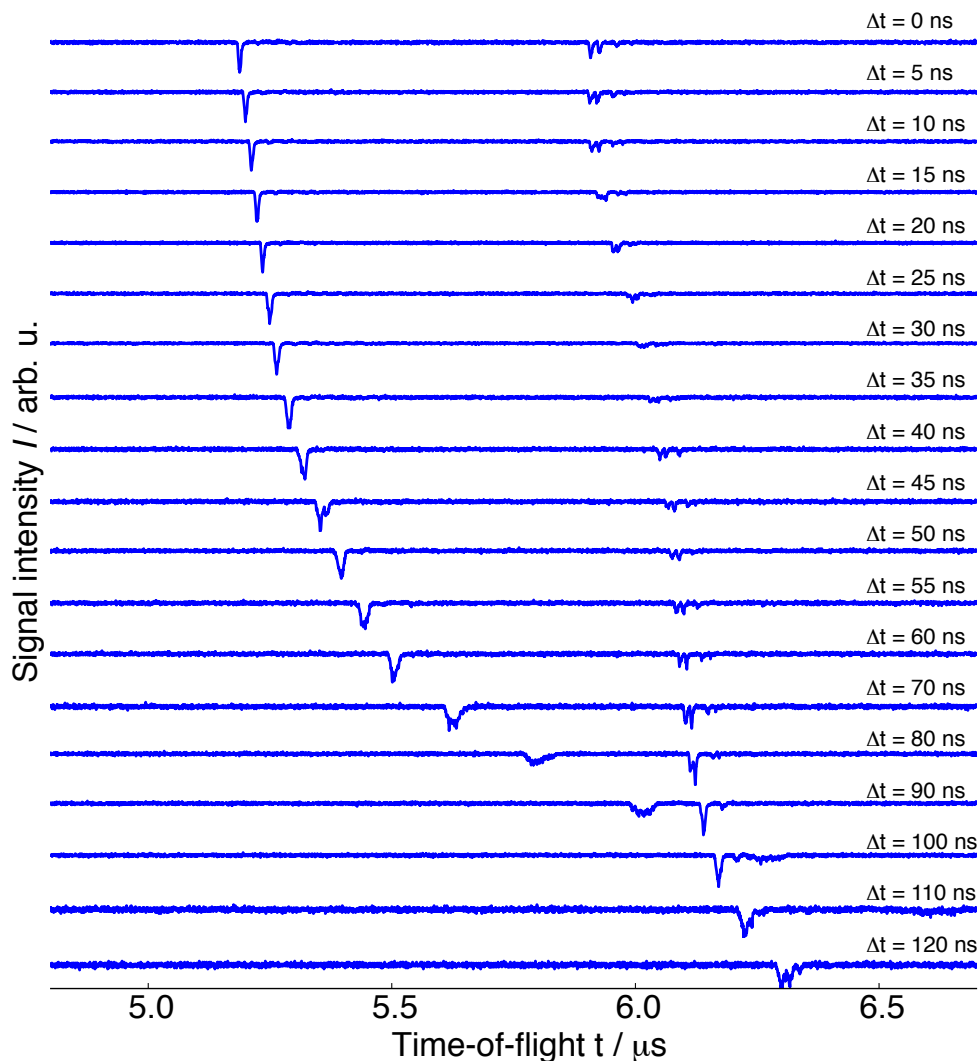


Figure 3.23: Lift-TOF spectra of mixed Ca^+/CaO^+ Coulomb crystals accelerated with the lift at different lift delays Δt . The RF potential was turned off prior to the ion extraction. Each trace is an average over 3 experiments.

3.4 Summary

In the present chapter a new apparatus for conformer dependent ion-molecule reactions was described. We designed and characterized a new linear quadrupole ion trap that is coupled to a time-of-flight mass spectrometer with a post-

ejection-acceleration scheme that produces high resolution mass spectra with $m/\Delta m \approx 700$. Compared to previous LQTs coupled to a TOF mass spectrometer, we achieve a higher resolution at the cost of having to scan the post-ejection-acceleration delay over several experiments. In the TOF traps reported by Schowalter *et al.* and Deb *et al.* [134, 137], all ion masses can be assigned from a single experiment but these setups require much more complicated electronics or trapping techniques which have additional drawbacks like heating of the Coulomb crystals.

The post-ejection-acceleration delay does not have to be scanned over the full range to find the best setting. One can easily estimate the correct delay range from the low resolution TOF spectra and then scan over that range to find the optimal signal, as was done with the CaOH^+ ions in the present study. In this way high-resolution mass spectra for all ion species in the trap can be recorded in a reasonable amount of time.

By measuring the second order rate constant for the reaction: $\text{Ca}^+ + \text{N}_2\text{O} \rightarrow \text{CaO}^+ + \text{N}_2$, we have demonstrated that we can quantify the number of trapped ions. This makes our apparatus a versatile tool to investigate the rates of ion-molecule reactions.

The new TOF-MS can also be operated with the RF potential applied while the ions are ejected. Similar to Jyothi *et al.* [140], we see a strong RF phase angle dependence on the ion ejection efficiency and their flight time. This resulted in very complicated spectra. Post-ejection-acceleration yields the correct mass for CaO^+ , but the mass resolution is an order of magnitude lower compared to the measurements with the RF turned off. A post-ejection-acceleration with a potential lift was tested and in order to unambiguously assign the masses of all ions in a multi component crystal, the TOF spectra were averaged over all RF phases which reduced the resolution even further. A distinction between CaO^+ and CaOH^+ was not possible for any of the measurements in RF-on mode. For high resolution TOF spectra that are easy to analyze it is necessary to switch the RF off before ejecting the ions.

Chapter 4

Rotationally state selected ion-molecule reactions ¹

4.1 Introduction

Rotational effects in ion-molecule reactions have been studied for several systems, with the ion in selected rovibrational quantum states [148–156]. Ions can be prepared in specific rovibrational quantum states by means of state specific ionization techniques like threshold ionization [130, 131]. Rotational excitation can enhance the reactivity. For example, rotationally excited H_2O^+ ions react with larger rate constants with H_2 and D_2 than H_2O^+ ions in the rotational ground state [148, 155, 156]. Rotational excitation does not generally increase the reaction rate. For example, in the charge transfer reaction of $\text{N}_2^+ + \text{Ar} \rightarrow \text{Ar}^+ + \text{N}_2$ and the reaction of $\text{NO}^+ + \text{C}_2\text{H}_5\text{OH} \rightarrow \text{HNO} + \text{C}_2\text{H}_4\text{OH}^+$, the rate constant is independent of the rotational quantum state of the reactant ion [149, 150, 153].

Only a few studies have been performed with neutral molecules in selected rotational states. Liu *et al.* studied the reaction $\text{Cl} + \text{CHD}_3 \rightarrow \text{HCl} + \text{CD}_3$ in a crossed molecular beam experiment [157]. They observed an enhancement of the reaction with increasing rotational angular momentum of CHD_3 . Martinez

¹The experimental data which is presented in this chapter was acquired and analysed by Hong Gao and Ardita Kilaj.

et al. studied the temperature dependence of the reaction $\text{OH}^+ + \text{H}_2/\text{D}_2 \rightarrow \text{H}_2\text{O}^+/\text{HDO}^+$ and did quasi-classical trajectory calculations for this reaction. Their calculations predict a strong enhancement of the reaction rate if the OH^+ ion is rotationally excited, but only a small effect if the neutral H_2 or D_2 is rotationally excited [158].

In the electrostatic deflector, conformers are separated due to their different dipole moments. Since the effective dipole moment is dependent on the rotational state of the molecule, the deflector can be used as a quantum state selector. This has been shown before by Nielsen *et al.* for carbonyl sulfide (OCS) [52]. The effective dipole moments of the rotational ground states of *para* water ($j = 0$) and *ortho* water ($j = 1, \tau = -1$) are different enough so that the two spin isomers of water could be separated using the electrostatic deflector [159].

Based on these results, we had the idea to use this to study rotational state specific effects in ion-molecule reactions with the neutral species in selected rotational quantum states. For a proof of concept experiment, a capture-limited reaction would be useful since we can easily compare the results to theory. A possible candidate reaction is the charge transfer between OCS and O_2^+ . This reaction was studied before at room temperature in a SIFT apparatus and the reported rate constant is $1.0 \times 10^{-9} \text{cm}^3 \text{s}^{-1}$ with an error of $\pm 20\%$. The capture rate constant was calculated using ADO theory [160] to be $1.4 \times 10^{-9} \text{cm}^3 \text{s}^{-1}$ [161].

In the experimental part of this Chapter, we measure deflection profiles of a molecular beam of OCS to characterize the beam and validate the new experimental setup described in chapter 3. As will be shown, OCS proved to be not the ideal molecule to study rotational state specific capture rates, since the differences in the rates for the rotational ground state and the first few excited states are very small. Therefore, a theoretical investigation, to find a suitable system with measurable differences in the state specific capture rates is performed and a new experiment is suggested and simulated.

4.2 Experimental setup

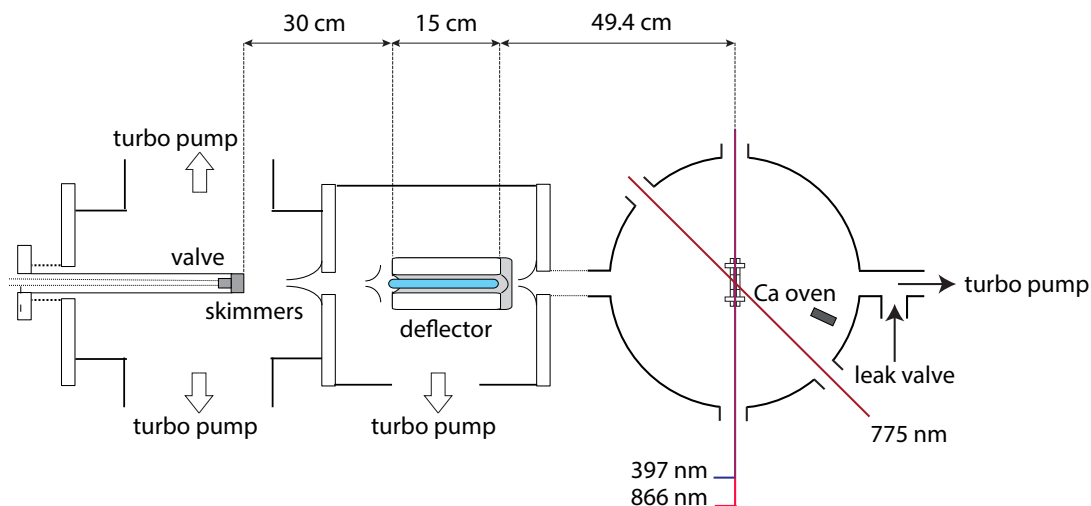


Figure 4.1: Top view schematic of the molecular beam machine with the reaction chamber.

The experimental setup is the same as the one described in Chapter 3. See Figure 4.1 for a schematic of the experimental setup. The only difference to the setup in Chapter 3, is the exchange of the 355 nm laser for a femtosecond laser with a center wavelength at 775 nm. The femtosecond laser (CPA 2110, Clark-MXR, Inc.) can be operated with a repetition rate of 1 kHz and generates ~ 150 fs long pulses with an energy of 1 mJ per pulse. We use the femtosecond laser for strong-field ionization [162–164]. The big advantage of strong-field ionization is that any molecule can be ionized easily, without the need of having to search for a resonant transition. The disadvantage is that the species selectivity of REMPI is lost. This means that for a molecular beam consisting of several conformers, everything would be ionized and conformer specific deflection curves can not be recorded. Also, the high pulse peak power leads to ion fragmentation and multiply charged ions. For measuring deflection profiles, this is not a problem, but if one wants to generate molecular ions to load them into a Coulomb crystal for reaction experiments, this could cause problems.

The molecular beam valve was operated with a backing pressure of 3 or 6 bar with a gas mixture of 1 ‰ OCS in neon. The valve was operated with a repe-

4.2 Experimental setup

tition rate of 20 Hz and 44 μs long opening pulses supplied to the piezo, which generated gas pulses with a FWHM of $\sim 200 \mu\text{s}$ length.

To measure OCS deflection profiles, the molecular beam was ionized by the femtosecond laser in the center of the ion trap and the ions were detected using the TOF-MS. The laser was focused to a spotsize of $\sim 200 \mu\text{m}$. Static voltages were applied to the trap rods to help focus the ions onto the MCP detector. See Figure 4.2 for a schematic of the potentials applied to the electrodes. These potentials were obtained from Simion [69] simulations where a beam of OCS^+ ions with a x -velocity of 900 m/s was generated at the center of the trap.

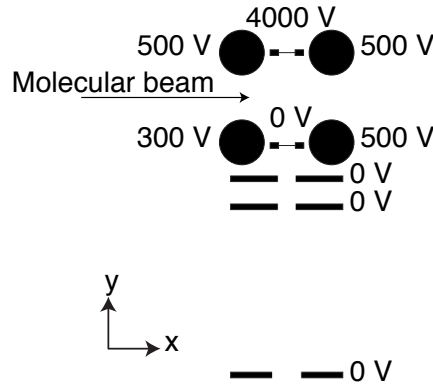


Figure 4.2: Static voltages applied to the trap to focus the OCS^+ ions generated from the molecular beam onto the MCP detector.

The angle of the beam machine was varied by changing the height of the molecular beam machine translation stage in $h_b = 0.5 \text{ mm}$ steps for the control screw further away from the ion trap (back screw) and $h_f = 0.2 \text{ mm}$ steps for the control screw closer to the ion trap (front screw). These step sizes lead to displacements of the undeflected molecular beam at the trap center by $h_t = -0.32 \text{ mm}$ (back screw) and $h_t = +0.33 \text{ mm}$ (front screw), where $+/-$ denote the height displacement along the y dimension with respect to the trap center. Figure 4.3 shows a schematic of how the displacement is determined. The distance between back and front screw is $l_1 = 77 \text{ cm}$ and the distance from the front screw to the trap center is $l_2 = 49.4 \text{ cm}$. The front screw is underneath the end of the deflector. For an increase of the back screw, the beam displacement

4. Rotationally state selected ion-molecule reactions

at the trap center is given by $h_t = -\tan(\alpha) \cdot l_2$, with $\tan(\alpha) = h_b/l_1$. For an increase of the front screw the displacement is given by $h_t = \tan(\beta) \cdot (l_1 + l_2)$, with $\tan(\beta) = h_f/l_1$. If a high voltage is supplied to the deflector, high field seeking states will be deflected upwards and the beam has to be tilted down, by increasing the length of the back screw to overlap the deflected beam with the trap center. For a low field seeking state, the length of the front screw has to be increased to overlap the downward deflected beam with the trap center. To indicate the height of the deflected beam with respect to the trap center we use the deflection coordinate $y = -h_t$.

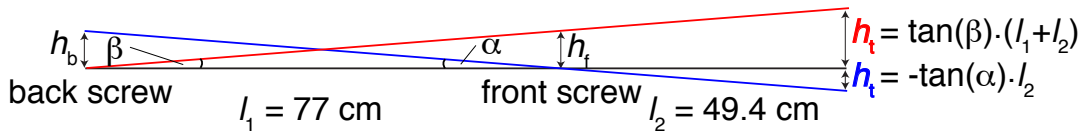


Figure 4.3: Determination of beam displacement height h_t at the trap center.

4.3 Results and discussion

4.3.1 Measurement of OCS deflection profiles

Figure 4.4 shows experimental deflection profiles of OCS measured at 13 kV deflector potential. Each data point is the average over 3 measurements, where each measurement is the integrated OCS⁺ signal of an average of 100 TOF traces. The deflection profile was simulated with Monte-Carlo trajectory simulations of 10⁶ molecules using BaselFly. The simulated molecular beam had a velocity of 900 m/s with a 10 % velocity spread. The experimental profile is best reproduced for a beam with a 3.56 m/s FWHM for the velocity spread in the velocity components perpendicular to the molecular beam axis (see Figure 4.4A). A rotational temperature of 0.7 K yields a simulated deflection profile that agrees well with the experiment (see Figure 4.4B). Figure 4.5 shows simulations at varying beam velocities. Over a range of 100 m/s, the profile does not change significantly, except the width changes slightly. The two simulations with velocities of 900 and 950 m/s both agree well with the experimental data.

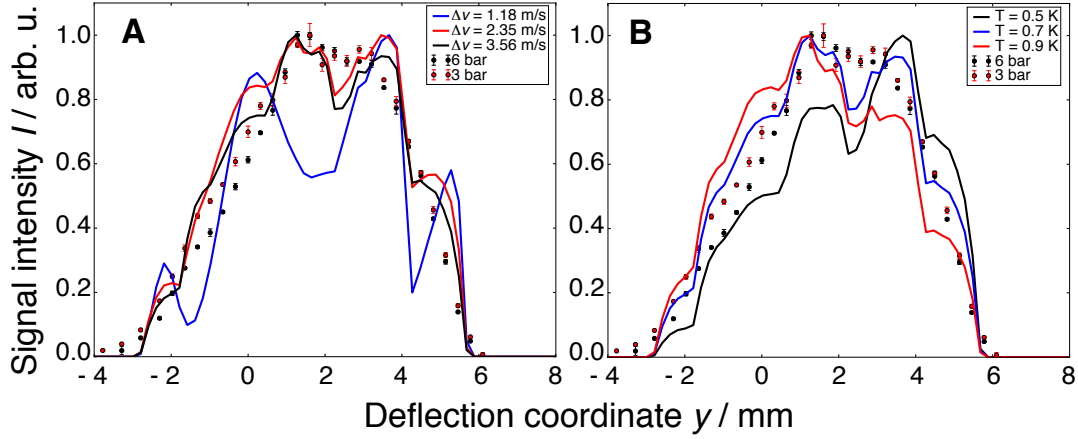


Figure 4.4: **A** Experimental deflection profile of OCS at 13 kV deflector potential and 3 bar (red dots) or 6 bar (black dots) backing pressure. The error bars correspond to one standard deviation. The simulated profiles (solid lines) correspond to a rotational temperature of 0.7 K. Δv is the FWHM of the normal distribution of the velocity components perpendicular to the molecular beam. **B** Same experimental data as in **A**. Simulations are done with $\Delta v = 3.56$ m/s at varying rotational temperatures.

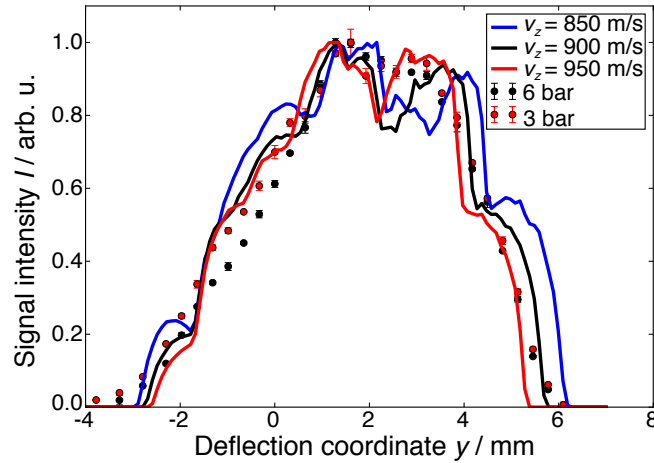


Figure 4.5: Experimental deflection profiles (red and black dots) of OCS at 13 kV deflector potential. The solid lines are simulated deflection profiles for different molecular beam velocities (v_z). The rotational temperature in all simulations was 0.7 K. $\Delta v = 3.56$ m/s in all simulations.

4. Rotationally state selected ion-molecule reactions

For all other simulations and calculations a molecular beam velocity of 900 m/s was used.

Figure 4.6 shows experimental and simulated deflection curves at 0 and 13 kV. The agreement between simulation and experiment at 0 kV is not satisfactory. The wider experimental beam profile suggests that in the experiment the molecular beam is transversally hotter than in the simulations. Increasing the perpendicular velocity spread does not improve the simulations. For the simulation in Figure 4.6A a perpendicular velocity spread with a FWHM of 3.56 m/s was used. With this velocity spread, already only about one third of all simulated molecules reach the ion trap. The sharp edges on the slopes of the simulated beam profile are generated by the deflector blocking part of the molecular beam. Also interesting is the fact that the experimentally measured beam profile at 0 kV does not have a gaussian bell shape as expected for a perfect gas pulse. The slopes of the curve appear gaussian, but the top is flattened out. The MCP detector is operated at a potential where the signal should not be saturated. This could be caused by skimmer interference, limiting the beam density at the center of the beam.

In Figure 4.6B, the simulated rotational state dependent deflection profiles are shown. At a deflection coordinate of ~ 5 mm, a molecular beam of OCS in the rotational ground state is obtained. Below -2 mm all molecules are in $j = 2$. Figure 4.7 shows the M state dependent deflection profiles. This illustrates the complexity of the j -dependent deflection curves which are the sum of the M state deflection curves for a given rotational state j .

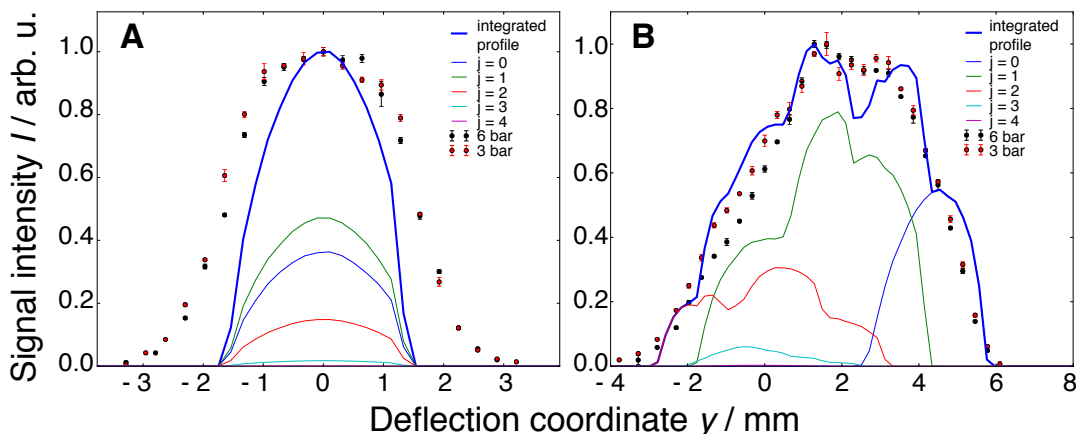


Figure 4.6: Experimental (red and black dots) and simulated (solid lines) OCS deflection profile at 0 kV (**A**) and 13 kV (**B**) deflector potential. The rotational temperature in the simulations was $T = 0.7$ K. The simulated rotational state specific deflection profiles are shown as well.

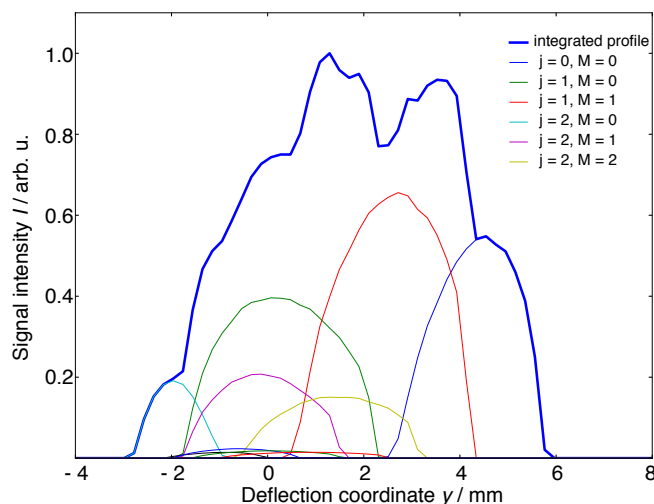


Figure 4.7: Simulated OCS deflection profile at $T = 0.7$ K and 13 kV deflector potential with M state deflection profiles shown for $j = 0 - 2$.

The good spatial separation of the rotational states would in principle allow for the measurement of rotational state specific rate constants for an ion-molecule reaction involving OCS. Possible candidate reactions are the charge transfer with O_2^+ and the reactive collisions with N_2^+ which forms the products

4. Rotationally state selected ion-molecule reactions

OCS⁺ (20 %) and S⁺ (80 %) [161].

Table 4.1: Calculated rotational state dependent capture rate constants for the reactions of OCS with O₂⁺ and N₂⁺ for molecular beam velocities at 900 m/s (Ne as carrier gas) and 470 m/s (Kr as carrier gas). All rate constants are in units of 10⁻⁹cm³s⁻¹.

j	OCS + O ₂ ⁺ 900 m/s	OCS + O ₂ ⁺ 470 m/s	OCS + N ₂ ⁺ 900 m/s	OCS + N ₂ ⁺ 470 m/s
0	1.787	2.404	1.904	2.559
1	1.766	2.340	1.875	2.495
2	1.744	2.274	1.846	2.434
3	1.720	2.223	1.814	2.367

Table 4.1 shows the calculated adiabatic-capture-theory rate constants for the reaction of OCS with O₂⁺ or N₂⁺ ions. The difference in the capture rates for different rotational states is only a few percent even at the lower collision energy when using krypton as a carrier gas. These small differences would be very difficult to resolve experimentally with the current setup.

4.3.2 Estimation of OCS density in the molecular beam

While the OCS + O₂⁺ reaction might not be a suitable candidate for the measurement of rotational state specific capture rates, we can use it for an estimate of the OCS density in the molecular beam. Experiments to determine the reaction rate constant of an undeflected OCS beam reacting with sympathetically cooled O₂⁺ ions inside a Ca⁺ Coulomb crystal are currently ongoing and preliminary results are presented here.

The pseudo-first order rate constant is obtained by measuring the O₂⁺ ion concentration in the Coulomb crystal using the TOF-MS (see Chapter 3 for a discussion of the method). The molecular beam was operated with a repetition rate of 100 Hz and with the same pulse durations as in the deflection measurements. Figure 4.8 shows the measurement of the reduction of O₂⁺ ions in the trap when the molecular beam is operated. To measure the background reaction of impu-

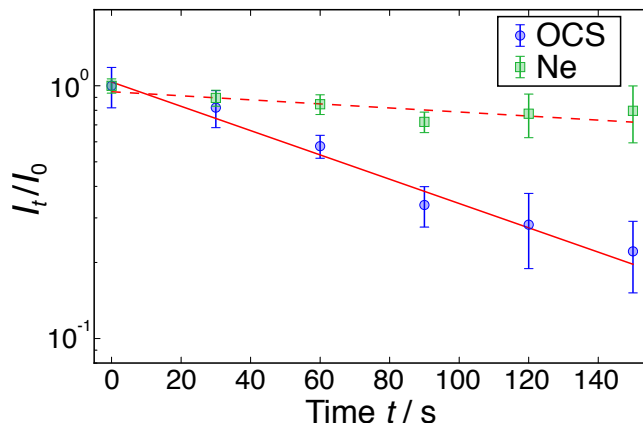


Figure 4.8: Pseudo-first order rate measurement for the reaction of O_2^+ with OCS, showing the reduction of O_2^+ ions (blue symbols). The background reaction (green symbols) was measured with a pure Ne beam. The error bars correspond to one standard deviation.

rities in the molecular beam reacting with O_2^+ , the Coulomb crystal was reacted with a beam of neon gas. We assume that the neon gas has the same amount of impurities as the OCS/Ne mixture. The background-corrected pseudo-first order rate constant is $k' = 0.010(1) \text{ s}^{-1}$.

The reported second order rate constant of $1.0 \times 10^{-9} \text{ cm}^3\text{s}^{-1}$ was measured at room temperature using a SIFT apparatus [161]. The capture rate depends on the collision energy and rotational quantum state of the molecule. The collision energy in our experiment corresponds to a temperature of $\sim 1020 \text{ K}$, but the molecular beam is not in thermal equilibrium and only the first three rotational states are populated. Since the reported experimental value at 300 K is close to the calculated capture rate, we assume that this reaction is capture limited. Therefore, for estimating the OCS density in the molecular beam we will use $k(900 \text{ m/s}) = 1.74 \times 10^{-9} \text{ cm}^3\text{s}^{-1}$ which is obtained from the sum over the calculated capture rates of table 4.1 weighted by their state population in a beam of 0.7 K . With this second order rate constant, the calculated average OCS density is $n_{\text{avg}} = 5.7(6) \times 10^6 \text{ cm}^{-3}$ and the OCS density per pulse is $n_{\text{pulse}} = 2.9(3) \times 10^8 \text{ cm}^{-3}$. Where n_{avg} is the product of n_{pulse} , the repetition rate (100 Hz) and the pulse duration ($200 \mu\text{s}$). The OCS density is similar to the

4. Rotationally state selected ion-molecule reactions

estimated 3-aminophenol densities achieved with the Even-Lavie valve, where $n_{\text{avg}} = 7.7(12) \times 10^6 \text{ cm}^{-3}$ and $n_{\text{pulse}} = 2.56(41) \times 10^8 \text{ cm}^{-3}$. This means that the cantilever piezovalve performs as well as the Even-Lavie valve with comparable beam densities and rotational temperatures.

4.3.3 Theoretical investigation of rotational state specific capture rates

To find out which parameters govern the relative difference in the rotational state dependent capture rates, a systematic parameter scan for an artificial ion-molecule reaction has been performed. The molecule was a generic linear top with a mass of 60 u and an isotropic polarizability of 2 \AA^3 . The ion was singly charged with a mass of 30 u. The dipole moment, rotational constant and the collision energy were varied systematically.

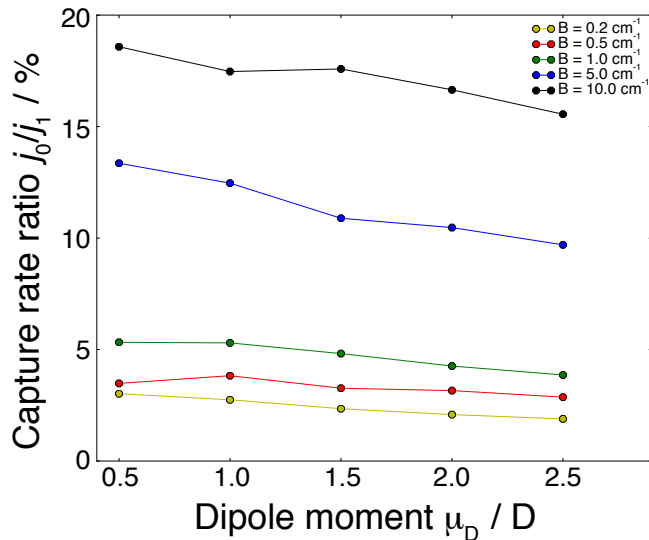


Figure 4.9: Relative rate difference of the rotational ground and first excited state versus the dipole moment for different rotational constants of the neutral. The molecular beam velocity was 470 m/s.

Figure 4.9 shows the results of the parameter scan for a molecular beam velocity of 470 m/s. Table 4.2 shows the results for a molecule with rotational

constant $B = 5 \text{ cm}^{-1}$ at different collision velocities and for two different dipole moments. It is interesting to note that while the absolute capture rate does increase with increasing dipole moment, the relative difference between the first two rotational states actually decreases slightly (see Figure 4.9). The biggest effect on the rotational state dependent capture rates are obtained by increasing the value of the rotational constant. The reason for this is that with increasing rotational constant, the spacing between the rotationally-adiabatic potential energy curves becomes larger, leading to a significant difference in the capture cross sections of adjacent rotational states. Reducing the collision energy also helps in increasing the capture rate difference between adjacent rotational states (see Table 4.2).

Table 4.2: Calculated capture rate constants for a linear top with rotational constant $B = 5 \text{ cm}^{-1}$, isotropic polarizability of 2 \AA^3 , dipole moment μ_D of 1.0 or 2.0 D at different molecular beam velocities, corresponding to the velocities of the carrier gasses: He, Ne, Kr and Xe. The mass of the linear top was 60 u, the mass of the singly charged ion was 30 u. All rate constants are in units of $10^{-9} \text{ cm}^3 \text{ s}^{-1}$.

μ_D / D	j	2000 m/s	900 m/s	470 m/s	365 m/s
1.0	0	1.172	1.673	2.485	2.938
1.0	1	1.146	1.582	2.209	2.541
1.0	2	1.111	1.477	1.919	2.109
1.0	3	1.081	1.373	1.660	1.739
2.0	0	1.622	2.662	4.314	5.295
2.0	1	1.572	2.509	3.905	4.648
2.0	2	1.528	2.355	3.436	3.885
2.0	3	1.483	2.196	2.962	3.184

From this investigation it is evident that the most promising approach to observe differences in rotational state dependent capture rates would be for a molecule with large rotational constants and reactions at low collision energies.

4. Rotationally state selected ion-molecule reactions

Water has large rotational constants with values of: $A = 27.877 \text{ cm}^{-1}$, $B = 14.512 \text{ cm}^{-1}$ and $C = 9.285 \text{ cm}^{-1}$ [86]. A suitable ion-molecule reaction involving water is the capture limited charge transfer reaction: $\text{H}_2\text{O} + \text{N}_2^+ \rightarrow \text{H}_2\text{O}^+ + \text{N}_2$, which has been observed in the artificial atmosphere of space shuttles in low-earth orbits and has been studied by several groups [165–168].

Table 4.3: Calculated rotational state dependent capture rates for the reaction $\text{H}_2\text{O} + \text{N}_2^+ \rightarrow \text{H}_2\text{O}^+ + \text{N}_2$ at different molecular beam velocities, corresponding to the velocities of the carrier gasses: He, Ne, Kr and Xe. All rate constants are in units of $10^{-9} \text{ cm}^3 \text{ s}^{-1}$.

j_τ	2000 m/s	900 m/s	470 m/s	365 m/s
0_0	2.088	3.588	5.889	7.122
1_{-1}	1.897	3.037	4.462	5.113
1_0	1.910	3.027	4.233	4.572
1_1	2.012	3.295	4.939	5.480
2_{-2}	1.797	2.695	3.705	4.116
2_{-1}	1.743	2.521	2.960	2.823
2_0	1.744	2.487	2.703	2.557
2_1	1.793	2.639	3.297	3.494
2_2	1.944	3.070	4.087	4.298

Table 4.3 shows calculated capture rate constants for water reacting with nitrogen ions. With a molecular beam velocity of 470 m/s, there is a $\sim 20 \%$ difference in the rates of $j = 0$ and $j = 1$. The relative rate difference between the τ states of $j = 1$ are 5 – 15 % for a beam velocity of 470 m/s. These differences in the rates should be observable.

Due to the large rotational constants of water, only the rotational ground state of each spin isomer is populated in a molecular beam with a rotational temperature of $\sim 1 \text{ K}$. Therefore, to be able to measure capture rates for different rotational states a warmer beam will be required. Figure 4.10 shows simulated deflection profiles of a 15 K warm molecular beam of water at different deflector potentials.

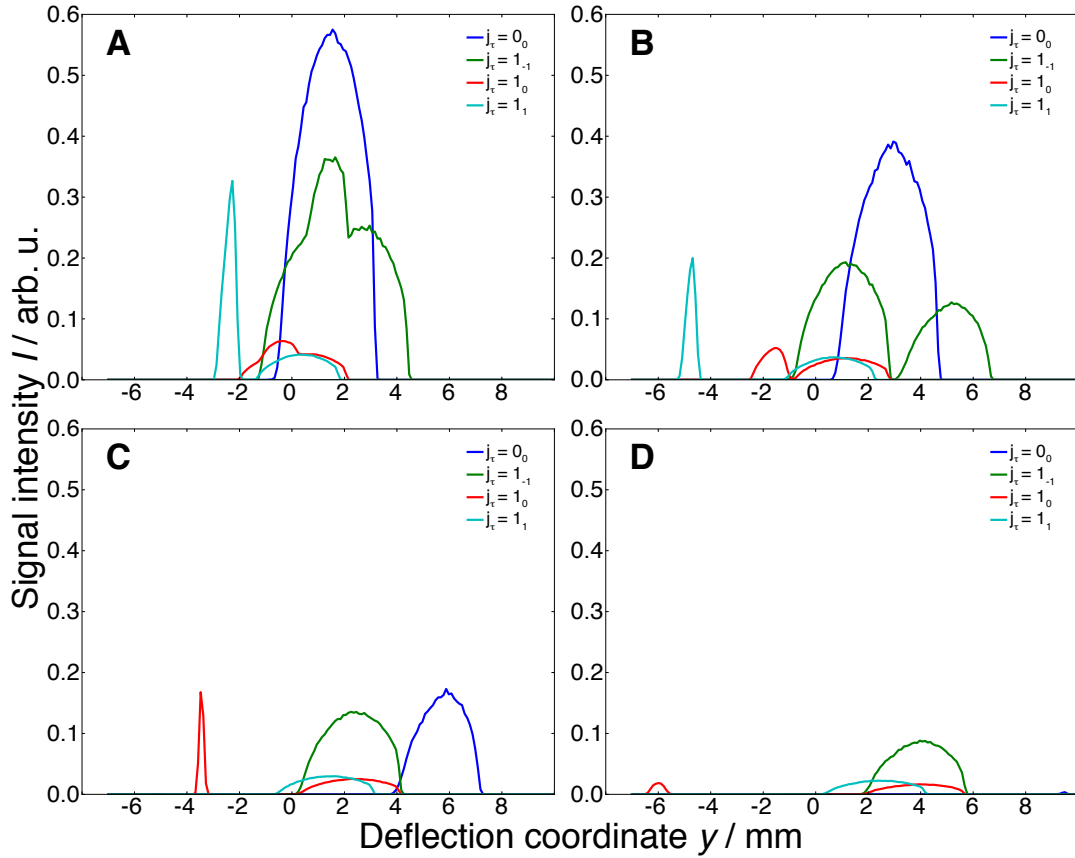


Figure 4.10: Simulated deflection profiles of a molecular beam of water at different deflector potentials with $T_{\text{rot}} = 15$ K. The beam velocity is 470 m/s. **A** Deflector voltage = 5 kV. **B** Deflector voltage = 7 kV. **C** Deflector voltage = 10 kV. **D** Deflector voltage = 13 kV.

For every quantum state, 10^6 molecules were simulated. The simulated velocity spread perpendicular to the molecular beam axis had a FWHM of 1.77 m/s. The deflection profiles do not change if this value is increased. These deflection profiles suggest that it should be possible to not only measure j dependent capture rates but also measure the τ dependent capture rate constants of $j = 1$. Depending on the deflector voltage and angle of the beam machine, molecular beams that purely consist of one τ component can be prepared.

4. Rotationally state selected ion-molecule reactions

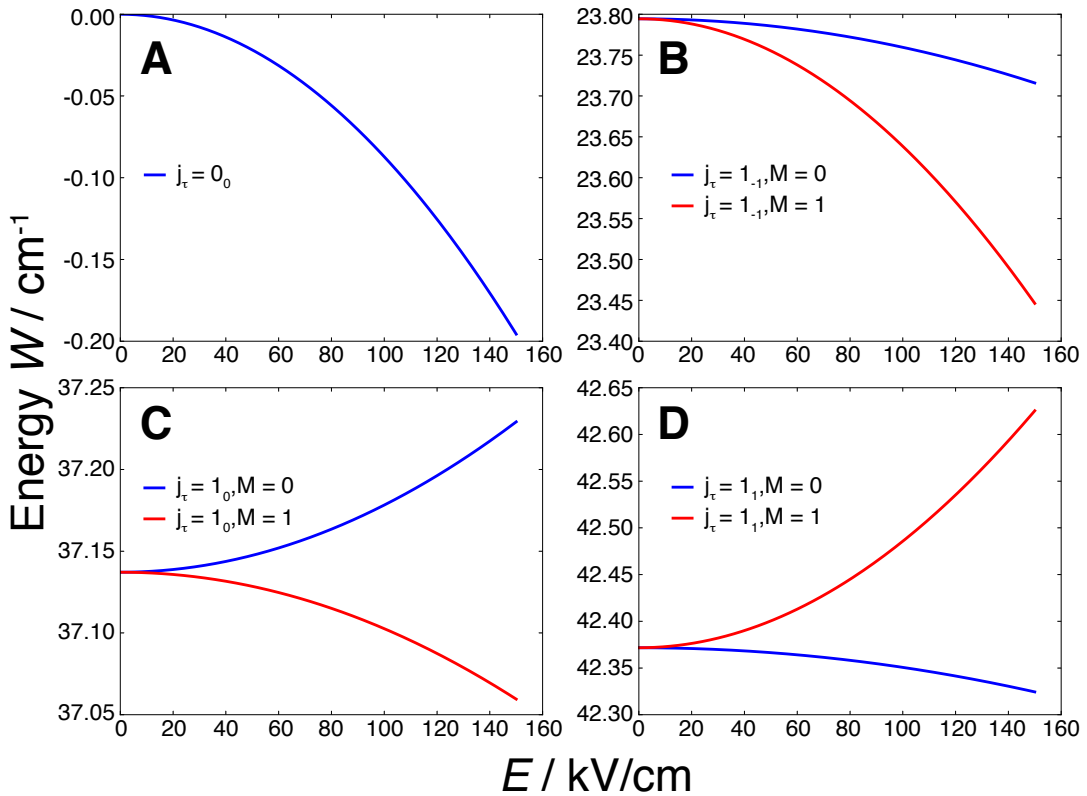


Figure 4.11: Stark energy curves of water. **A** $j_{\tau} = 0_0$, **B** $j_{\tau} = 1_{-1}$, **C** $j_{\tau} = 1_0$, **D** $j_{\tau} = 1_1$.

Figure 4.11 shows Stark energy curves of water for $j = 0$ and $j = 1$. Both M components of $j_{\tau} = 1_{-1}$ are high-field seeking states, but molecules with $M = 1$ will be deflected stronger than those with $M = 0$. This can be seen in the simulated deflection profiles with a deflector potential of 7 kV (Figure 4.10B). The deflection profile of $j_{\tau} = 1_{-1}$ is given by the green curve and the two M components create a bimodal profile, since the $M = 1$ component is deflected more strongly. At a deflection coordinate of $y = 6$ mm, a molecular beam of water in the rotational state $j_{\tau} = 1_{-1}$ is obtained. If the deflector voltage is increased to 10 kV (Figure 4.10C), the $M = 1$ component of $j_{\tau} = 1_{-1}$ is lost from the beam, since these molecules are deflected so much that they collide with the deflector electrode or do not pass the skimmer after the deflector. At 10 kV a beam in the rotational ground state is obtained at a deflection coordinate of $y = 6$ mm. To obtain state pure beams of $j_{\tau} = 1_0$ and $j_{\tau} = 1_1$ we can use the

low-field seeking states $M = 0$ for $j_\tau = 1_0$ and $M = 1$ for $j_\tau = 1_1$. At a deflector voltage of 5 kV (Figure 4.10A), a molecular beam in quantum state $j_\tau = 1_1$ can be obtained with a deflection coordinate of $y \approx 2.5$ mm. A pure beam with state $j_\tau = 1_0$ is obtained at a deflection coordinate of $y \approx 2$ mm at a deflector voltage of 7 kV (Figure 4.10B).

Figure 4.12 shows simulated capture rate profiles, that is the deflection profile weighted by the corresponding state specific capture rate constants (see Table 4.3) and scaled to the maximum of the deflection profile, for two deflector potentials. By measuring reaction profiles for several deflector potentials we should be able to determine j_τ state specific capture rate constants.

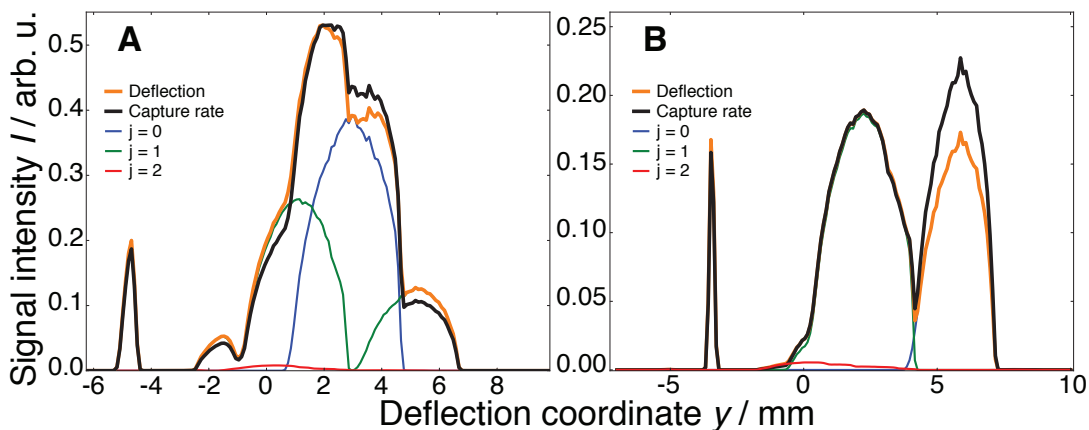


Figure 4.12: Simulated deflection profiles (orange) and capture rate profiles (black) at **A** 7 kV and **B** 10 kV for a molecular beam with 470 m/s velocity and rotational temperature of 15 K.

4.4 Summary

The deflection beam machine was tested with a molecular beam of OCS. The deflection works well and Monte-Carlo simulations for a beam with a rotational temperature of 0.7 K agree well with the experiment. There is some disagreement between experiment and theory for the width and shape of the profile of an undeflected beam, which is not fully understood yet. The reaction of OCS with oxygen ions is used to get an estimate of the molecular beam density and

4. Rotationally state selected ion-molecule reactions

preliminary results were shown. Capture rate calculations of OCS reacting with oxygen or nitrogen ions showed only very small differences in the rotational state specific capture rates. A systematic scan of parameters in adiabatic-dipole capture calculations revealed that the rotational constant and the collision energy have the biggest impact on the relative difference in rotational state dependent capture rates.

The reaction of water with nitrogen ions is suggested as a proof-of-concept experiment to measure τ resolved rotational state dependent capture rate constants. Monte-Carlo trajectory simulations suggest that it should be possible to generate a molecular beam of water in specific τ states for $j = 0 - 1$. Capture rate calculations suggest that for molecular beams with krypton or xenon as carrier gas, the capture rate difference between the τ states should be large enough to be experimentally observable.

Chapter 5

Outlook and Summary

In this work, a new method to study conformer-specific effects in ion-molecule gas phase reactions was developed. In a proof of concept experiment, the two conformers of 3-aminophenol were spatially separated in a molecular beam and reacted with a Coulomb crystal of Ca^+ ions. The reaction dynamics are mainly controlled by the long-range ion-dipole interaction and the measured rate constants are in good agreement with calculated rate constants from adiabatic-capture-theory.

A new experimental apparatus dedicated to conformer specific ion-molecule reactions incorporating a high resolution time-of-flight mass spectrometer was designed and tested successfully. The possibility of using this apparatus for rotationally quantum-state resolved rate measurements has been investigated theoretically for the charge transfer reaction of water with N_2^+ ions. It was found that a τ state resolved experiment for the first rotationally excited state of water should be feasible.

The method of spatially separating conformers or specific quantum states, opens a whole new toolbox for the physical chemist and I will try to give a short outlook on some possible future prospects and developments for conformer-specific and quantum-state controlled chemistry.

At the moment, a crossed molecular beam-machine is being constructed in our lab to expand the method to neutral-neutral collisions. This opens the possibil-

5. Outlook and Summary

ity to investigate a reaction under neutral and ionic conditions.

The Diels-Alder reaction [169] is heavily used in the synthesis of organic compounds [170]. The reaction is generally believed to be concerted, that is the two new sigma bonds between the diene and dienophile are formed at the same time. For polar cyclo-additions, where one of the reaction partners is charged, a stepwise mechanism is also possible [171]. We want to investigate the reaction between 2,3-dibromobutadiene and maleic anhydride. Figure 5.1 shows a schematic of this reaction. Only the reaction of the *cis*-2,3-dibromobutadiene conformer should yield the Diels-Alder product. We will spatially separate the *cis* from the *trans* conformer and react them with neutral or charged maleic anhydride. This will enable us to study the reaction mechanism and determine if the reaction is concerted or following a stepwise mechanism.

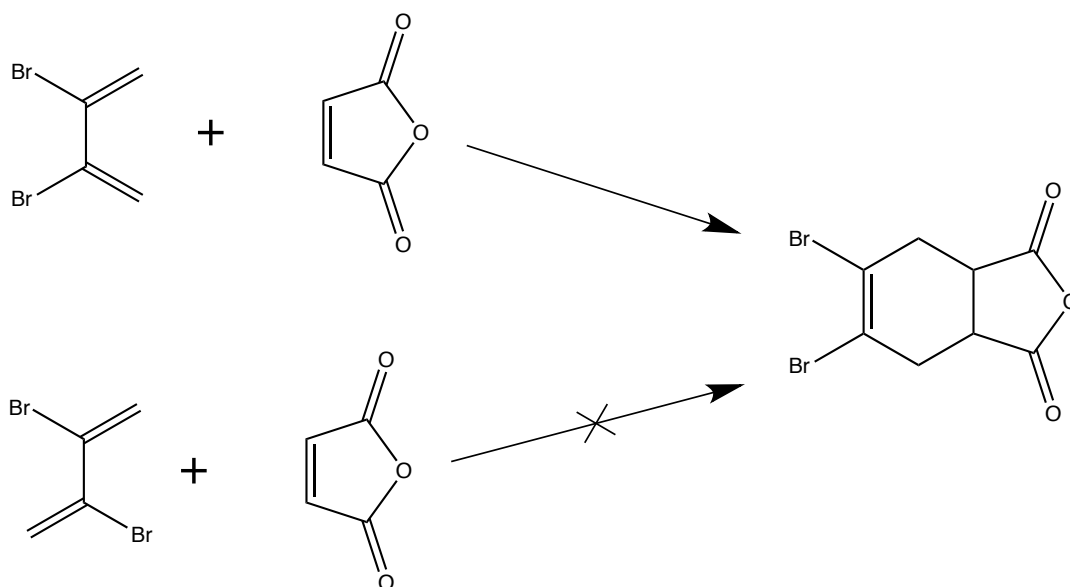


Figure 5.1: Diels-Alder reaction between 2,3-dibromobutadiene and maleic anhydride

At the moment only molecules with conformers that possess similar internal energies are usable. If the energy difference between the different conformations is too large, only the conformer with the lowest internal energy will be populated in the molecular beam. To expand this method to molecules with conformers

that possess a larger energy difference, one could employ a IR laser pulse to excite a normal mode that leads to conversion into another conformer [172].

If the rotational-quantum-state-resolved measurement of the charge transfer reaction between water and nitrogen ions is successful, the next logical step would be to not only prepare the neutral in a single quantum state, but also the ion. This would enable fully rotational and vibrational quantum state resolved ion-molecule reactions. Methods of preparing ions in specific rovibrational quantum states are already well established [130, 131] and could easily be incorporated into the existing experiment.

An interesting question is what effect the orientation of a molecule during a reaction has on the reactivity and reaction mechanism. Therefore, it would be interesting to not only control the conformation and quantum state of a molecule in a reaction, but also its alignment and orientation in the lab frame. This could be achieved by the use of additional electric and optical fields [173]. Such an experiment would certainly be exciting, although experimentally quite challenging.

Bibliography

- [1] E. B. Unal, A. Gursoy, and B. Erman, *Phys. Biol.*, 2009, **6**, 036014.
- [2] D. H. R. Barton, *J. Chem. Soc.*, 1953, **1953**, 1027.
- [3] H. C. Dunathan, L. Davis, P. G. Kury, and M. Kaplan, *Biochemistry*, 1968, **7**, 4532.
- [4] E. L. Eliel and S. H. Wilen, *Stereochemistry of organic compounds*, John Wiley & Sons, New York, US, 1994.
- [5] R. D. Suenram and F. J. Lovas, *J. Am. Chem. Soc.*, 1980, **102**, 7180.
- [6] T. R. Rizzo, Y. D. Park, L. A. Peteanu, and D. H. Levy, *J. Chem. Phys.*, 1986, **84**, 2534.
- [7] E. G. Robertson and J. P. Simons, *Phys. Chem. Chem. Phys.*, 2001, **3**, 1.
- [8] R. Weinkauff, J. Schermann, M. S. de Vries, and K. Kleinermanns, *Eur. Phys. J. D*, 2002, **20**, 309.
- [9] J. P. Simons, R. A. Jockusch, P. Çarçabal, I. Hünig, R. T. Kroemer, N. A. Macleod, and L. C. Snoek, *Int. Rev. Phys. Chem.*, 2005, **24**, 489.
- [10] M. S. de Vries and P. Hobza, *Annu. Rev. Phys. Chem.*, 2007, **58**, 585.
- [11] M. E. Sanz, S. Blanco, J. C. Lopez, and J. L. Alonso, *Angew. Chem. (int. ed. engl.)*, 2008, **47**, 6216.
- [12] T. R. Rizzo, J. A. Stearns, and O. V. Boyarkin, *Int. Rev. Phys. Chem.*, 2009, **28**, 481.

- [13] N. S. Nagornova, T. R. Rizzo, and O. V. Boyarkin, *Science*, 2012, **336**, 320.
- [14] D.-L. Huang, H.-T. Liu, C.-G. Ning, and L.-S. Wang, *J. Phys. Chem. Lett.*, 2015, **6**, 2153.
- [15] S. Lopes, A. V. Domanskaya, M. Räsänen, L. Khriachtchev, and R. Fausto, *J. Phys. Chem.*, 2015, **143**, 104307.
- [16] B. C. Dian, A. Longarte, and T. S. Zwier, *Science*, 2002, **296**, 2369.
- [17] B. C. Dian, J. R. Clarkson, and T. S. Zwier, *Science*, 2004, **303**, 1169.
- [18] B. C. Dian, G. G. Brown, K. O. Douglass, and B. H. Pate, *Science*, 2008, **320**, 924.
- [19] K. Pande, C. D. M. Hutchison, G. Groenhof, A. Aquila, J. S. Robinson, J. Tenboer, S. Basu, S. Boutet, D. P. DePonte, M. Liang, T. A. White, N. A. Zatsepin, O. Yefanov, D. Morozov, D. Oberthuer, C. Gati, G. Subramanian, D. James, Y. Zhao, J. Koralek, J. Brayshaw, C. Kupitz, C. Conrad, S. Roy-Chowdhury, J. D. Coe, M. Metz, P. L. Xavier, T. D. Grant, J. E. Koglin, G. Ketawala, R. Fromme, V. Šrajer, R. Henning, J. C. H. Spence, A. Ourmazd, P. Schwander, U. Weierstall, M. Frank, P. Fromme, A. Barty, H. N. Chapman, K. Moffat, J. J. van Thor, and M. Schmidt, *Science*, 2016, **352**, 725.
- [20] S. T. Park and M. S. Kim, *J. Am. Chem. Soc.*, 2002, **124**, 7614.
- [21] S. T. Park, S. K. Kim, and M. S. Kim, *Nature*, 2002, **415**, 306.
- [22] M. H. Kim, L. Shen, H. Tao, T. J. Martinez, and A. G. Suits, *Science*, 2007, **315**, 1561.
- [23] T. A. A. Oliver, G. A. King, and M. N. R. Ashfold, *Chem. Sci.*, 2010, **1**, 89.
- [24] T. A. A. Oliver, G. A. King, and M. N. R. Ashfold, *J. Chem. Phys.*, 2010, **133**, 194303.

BIBLIOGRAPHY

- [25] D. K. Zaouris, A. M. Wenge, D. Murdock, T. A. A. Oliver, G. Richmond, G. A. D. Ritchie, R. N. Dixon, and M. N. R. Ashfold, *J. Chem. Phys.*, 2011, **135**, 094312.
- [26] C. A. Taatjes, O. Welz, A. J. Eskola, J. D. Savee, A. M. Scheer, D. E. Shallcross, B. Rotavera, E. P. F. Lee, J. M. Dyke, D. K. W. Mok, D. L. Osborn, and C. J. Percival, *Science*, 2013, **340**, 177.
- [27] L. Khriachtchev, A. Domanskaya, K. Marushkevich, M. Räsänen, B. Grigorenko, A. Ermilov, N. Andrijchenko, and A. Nemukhin, *J. Phys. Chem. A*, 2009, **113**, 8143.
- [28] W. Schöllkopf and J. P. Toennies, *Science*, 1994, **266**, 1345.
- [29] D. J. Nesbitt, *Chem. Rev.*, 2012, **112**, 5062.
- [30] S. Chefdeville, Y. Kalugina, S. Y. T. van de Meerakker, Ch. Naulin, F. Lique, and M. Costes, *Science*, 2013, **341**, 1094.
- [31] A. B. Henson, S. Gersten, Y. Shagam, J. Narevicius, and E. Narevicius, *Science*, 2012, **338**, 234.
- [32] S. N. Vogels, J. Onvlee, S. Chefdeville, A. van der Avoird, G. C. Groenenboom, and S. Y. T. van de Meerakker, *Science*, 2015, **350**, 787.
- [33] M. D. Morse in *Atomic, Molecular, and Optical Physics: Atoms and Molecules*, ed. F. Dunning and R. G. Hulet, Vol. 29, Part B of *Experimental Methods in the Physical Sciences*; Academic Press, 1996; p. 21.
- [34] B. R. Rowe, G. Dupeyrat, J. B. Marquette, and P. Gaucherel, *J. Chem. Phys.*, 1984, **80**, 4915.
- [35] D. Irimia, D. Dobrikov, R. Kortekaas, H. Voet, D. A. van den Ende, W. A. Groen, and M. H. M. Janssen, *Rev. Sci. Instrum.*, 2009, **80**, 113303.
- [36] U. Even, *EPJ Tech. Instrum.*, 2015, **2**, 17.
- [37] R. N. Zare, *Angular Momentum*, John Wiley & Sons, New York, 1988.

- [38] P. W. Atkins and R. Friedman, *Molecular quantum mechanics*, Oxford University Press, fifth ed., 2005.
- [39] Y.-P. Chang, F. Filsinger, B. Sartakov, and J. Küpper, *Comput. Phys. Commun.*, 2014, **185**, 339.
- [40] H. L. Bethlem, M. R. Tarbutt, J. Küpper, D. Carty, K. Wohlfart, E. A. Hinds, and G. Meijer, *J. Phys. B: At. Mol. Opt. Phys.*, 2006, **39**, R263.
- [41] O. Stern, *Z. Phys.*, 1921, **7**, 249.
- [42] W. Gerlach and O. Stern, *Z. Phys.*, 1922, **9**, 349.
- [43] H. Kallmann and F. Reiche, *Z. Phys.*, 1921, **6**, 352.
- [44] E. Wrede, *Z. Phys.*, 1927, **44**, 261.
- [45] H. L. Bethlem, G. Berden, and G. Meijer, *Phys. Rev. Lett.*, 1999, **83**, 1558.
- [46] S. Y. T. van de Meerakker, H. L. Bethlem, N. Vanhaecke, and G. Meijer, *Chem. Rev.*, 2012, **112**, 4828.
- [47] S. Willitsch, M. T. Bell, A. D. Gingell, S. R. Procter, and T. P. Softley, *Phys. Rev. Lett.*, 2008, **100**, 043203.
- [48] K. Okada, T. Suganuma, T. Furukawa, T. Takayanagi, M. Wada, and H. A. Schuessler, *Phys. Rev. A*, 2013, **87**, 043427.
- [49] F. Filsinger, U. Erlekam, G. von Helden, J. Küpper, and G. Meijer, *Phys. Rev. Lett.*, 2008, **100**, 133003.
- [50] F. Filsinger, J. Küpper, G. Meijer, J. L. Hansen, J. Maurer, J. H. Nielsen, L. Holmegaard, and H. Stapelfeldt, *Angew. Chem. (int. ed. engl.)*, 2009, **48**, 6900.
- [51] T. Kierspel, D. A. Horke, Y.-P. Chang, and J. Küpper, *Chem. Phys. Lett.*, 2014, **591**, 130.

BIBLIOGRAPHY

- [52] J. H. Nielsen, P. Simesen, C. Z. Bisgaard, H. Stapelfeldt, F. Filsinger, B. Friedrich, G. Meijer, and J. Küpper, *Phys. Chem. Chem. Phys.*, 2011, **13**, 18971.
- [53] M. Germann, X. Tong, and S. Willitsch, *Nature Phys.*, 2014, **10**, 820.
- [54] R. Blatt and D. Wineland, *Nature*, 2008, **453**, 1008.
- [55] X. Tong, T. Nagy, J. Yosa Reyes, M. Germann, M. Meuwly, and S. Willitsch, *Chem. Phys. Lett.*, 2012, **547**, 1.
- [56] F. H. J. Hall, M. Aymar, N. Bouloufa-Maafa, O. Dulieu, and S. Willitsch, *Phys. Rev. Lett.*, 2011, **107**, 243202.
- [57] F. H. J. Hall, M. Aymar, M. Raoult, O. Dulieu, and S. Willitsch, *Mol. Phys.*, 2013, **111**, 1683.
- [58] S. Willitsch, *Int. Rev. Phys. Chem.*, 2012, **31**, 175.
- [59] W. Paul, *Rev. Mod. Phys.*, 1990, **62**, 531.
- [60] M. Drewsen and A. Brøner, *Phys. Rev. A*, 2000, **62**, 045401.
- [61] S. Willitsch, M. T. Bell, A. D. Gingell, and T. P. Softley, *Phys. Chem. Chem. Phys.*, 2008, **10**, 7200.
- [62] M. Drewsen, A. Mortensen, R. Martinussen, P. Staantum, and J. L. Sørensen, *Phys. Rev. Lett.*, 2004, **93**, 243201.
- [63] F. Schmidt-Kaler, H. Häffner, S. Gulde, M. Riebe, G. P. T. Lancaster, T. Deuschle, C. Becher, W. Hänsel, J. Eschner, C. F. Roos, and R. Blatt, *Appl. Phys. B*, 2003, **77**, 789.
- [64] D. J. Berkeland, J. D. Miller, J. C. Bergquist, W. M. Itano, and D. J. Wineland, *J. Appl. Phys.*, 1998, **83**, 5025.
- [65] R. E. March and J. F. Todd, *Quadrupole Ion Trap Mass Spectrometry*, John Wiley & Sons, Hoboken, 2 ed., 2005.

- [66] F. G. Major, V. N. Gheorghe, and G. Werth, *Charged Particle Traps*, Springer, Berlin and Heidelberg, 2005.
- [67] M. G. House, *Phys. Rev. A*, 2008, **78**, 033402.
- [68] A. Mokhberi and S. Willitsch, *New J. Phys.*, 2015, **17**, 045008.
- [69] Simion 8.0/8.1 user manual. D. J. Manura and D. A. Dahl; Scientific Instrument Services, Inc., Ringoes, NJ, rev. 5 ed., 2011.
- [70] B. Roth, P. Blythe, H. Wenz, H. Daerr, and S. Schiller, *Phys. Rev. A*, 2006, **73**, 042712.
- [71] A. D. Gingell, M. T. Bell, J. M. Oldham, T. P. Softley, and J. M. Harvey, *J. Chem. Phys.*, 2010, **133**, 194302.
- [72] B. Heazlewood and T. P. Softley, *Annu. Rev. Phys. Chem.*, 2015, **66**, 475.
- [73] C. B. Zhang, D. Offenbergl, B. Roth, M. A. Wilson, and S. Schiller, *Phys. Rev. A*, 2007, **76**, 012719.
- [74] T. Matthey, T. Cickovski, S. S. Hampton, A. Ko, Q. Ma, M. Nyerges, T. Raeder, T. Slabach, and J. A. Izaguirre, *ACM Trans. Math. Softw.*, 2004, **30**, 237.
- [75] S. S. Prasad and W. T. Huntress, Jr., *Astrophys. J.*, 1980, **239**, 151.
- [76] Woodall, J., Agúndez, M., Markwick-Kemper, A. J., and Millar, T. J., *A&A*, 2007, **466**, 1197.
- [77] V. Wakelam, I. W. M. Smith, E. Herbst, J. Troe, W. Geppert, H. Linnartz, K. Öberg, E. Roueff, M. Agúndez, P. Pernot, H. M. Cuppen, J. C. Loison, and D. Talbi, *Space Sci. Rev.*, 2010, **156**, 13.
- [78] T. P. Snow and V. M. Bierbaum, *Annu. Rev. Anal. Chem.*, 2008, **1**, 229.
- [79] B. R. Rowe and J. B. Marquette, *Int. J. Mass Spectrom. Ion Processes*, 1987, **80**, 239.

BIBLIOGRAPHY

- [80] C. Rebrion, J. Marquette, B. Rowe, and D. Clary, *Chem. Phys. Lett.*, 1988, **143**, 130.
- [81] D. Gerlich and M. Smith, *Phys. Scr.*, 2006, **73**, C25.
- [82] L. Bass, T. Su, W. Chesnavich, and M. Bowers, *Chem. Phys. Lett.*, 1975, **34**, 119.
- [83] J. Troe, *Chem. Phys. Lett.*, 1985, **122**, 425.
- [84] D. Clary, *Mol. Phys.*, 1985, **54**, 605.
- [85] D. C. Clary, *J. Chem. Soc., Faraday Trans. 2*, 1987, **83**, 139.
- [86] T. Stoecklin, D. C. Clary, and A. Palma, *J. Chem. Soc. Faraday Trans.*, 1992, **88**, 901.
- [87] F. Filsinger, J. Küpper, G. Meijer, L. Holmegaard, J. H. Nielsen, I. Nevo, J. L. Hansen, and H. Stapelfeldt, *J. Chem. Phys.*, 2009, **131**, 064309.
- [88] T. Baba and I. Waki, *J. Appl. Phys.*, 2002, **92**, 4109.
- [89] T. Baba and I. Waki, *Jpn. J. Appl. Phys.*, 1996, **35**, L1134.
- [90] P. F. Staantum, K. Højbjerg, R. Wester, and M. Drewsen, *Phys. Rev. Lett.*, 2008, **100**, 243003.
- [91] B. Roth, P. Blythe, and S. Schiller, *Phys. Rev. A*, 2007, **75**, 023402.
- [92] M. Guilhaus, *J. Mass Spectrom.*, 1995, **30**, 1519.
- [93] W. C. Wiley and I. H. McLaren, *Rev. Sci. Instrum.*, 1955, **26**, 1150.
- [94] Y.-P. Chang, K. Długołęcki, J. Küpper, D. Rösch, D. Wild, and S. Willitsch, *Science*, 2013, **342**, 98.
- [95] S. Willitsch, *Int. Rev. Phys. Chem.*, 2012, **31**, 175.
- [96] J. N. Harvey, D. Schröder, W. Koch, D. Danovich, S. Shaik, and H. Schwarz, *Chem. Phys. Lett.*, 1997, **273**, 164.

- [97] X. Zhao, G. K. Koyanagi, and D. K. Bohme, *J. Phys. Chem. A*, 2006, **110**, 10607.
- [98] V. Ryzhov and R. C. Dunbar, *J. Am. Chem. Soc.*, 1999, **121**, 2259.
- [99] S. Willitsch, M. T. Bell, A. D. Gingell, and T. P. Softley, *Phys. Chem. Chem. Phys.*, 2008, **10**, 7200.
- [100] U. Even, J. Jortner, D. Noy, N. Lavie, and N. Cossart-Magos, *J. Chem. Phys.*, 2000, **112**, 8068.
- [101] H. K. Hughes, *Phys. Rev.*, 1947, **72**, 614.
- [102] C. A. Lee, B. P. Fabricand, R. O. Carlson, and I. I. Rabi, *Phys. Rev.*, 1953, **91**, 1395.
- [103] N. F. Ramsey, *Molecular Beams*, The International Series of Monographs on Physics, Oxford University Press, London, GB, 1956.
- [104] L. Holmegaard, J. H. Nielsen, I. Nevo, H. Stapelfeldt, F. Filsinger, J. Küpper, and G. Meijer, *Phys. Rev. Lett.*, 2009, **102**, 023001.
- [105] F. H. J. Hall, M. Aymar, N. Bouloufa-Maafa, O. Dulieu, and S. Willitsch, *Phys. Rev. Lett.*, 2011, **107**, 243202.
- [106] S. Willitsch, M. T. Bell, A. D. Gingell, S. R. Procter, and T. P. Softley, *Phys. Rev. Lett.*, 2008, **100**, 043203.
- [107] F. H. Hall, P. Eberle, G. Hegi, M. Raoult, M. Aymar, O. Dulieu, and S. Willitsch, *Mol. Phys.*, 2013, **111**, 2020.
- [108] B. Roth, P. Blythe, and S. Schiller, *Phys. Rev. A*, 2007, **75**, 023402.
- [109] J. A. Reese, T. V. Nguyen, T. M. Korter, and D. W. Pratt, *J. Am. Chem. Soc.*, 2004, **126**, 11387.
- [110] M. J. Frisch, G. W. Trucks, H. B. Schlegel, G. E. Scuseria, M. A. Robb, J. R. Cheeseman, G. Scalmani, V. Barone, B. Mennucci, G. A. Petersson, H. Nakatsuji, M. Caricato, X. Li, H. P. Hratchian, A. F. Izmaylov,

BIBLIOGRAPHY

- J. Bloino, G. Zheng, J. L. Sonnenberg, M. Hada, M. Ehara, K. Toyota, R. Fukuda, J. Hasegawa, M. Ishida, T. Nakajima, Y. Honda, O. Kitao, H. Nakai, T. Vreven, J. A. Montgomery, Jr., J. E. Peralta, F. Ogliaro, M. Bearpark, J. J. Heyd, E. Brothers, K. N. Kudin, V. N. Staroverov, R. Kobayashi, J. Normand, K. Raghavachari, A. Rendell, J. C. Burant, S. S. Iyengar, J. Tomasi, M. Cossi, N. Rega, J. M. Millam, M. Klene, J. E. Knox, J. B. Cross, V. Bakken, C. Adamo, J. Jaramillo, R. Gomperts, R. E. Stratmann, O. Yazyev, A. J. Austin, R. Cammi, C. Pomelli, J. W. Ochterski, R. L. Martin, K. Morokuma, V. G. Zakrzewski, G. A. Voth, P. Salvador, J. J. Dannenberg, S. Dapprich, A. D. Daniels, Ö. Farkas, J. B. Foresman, J. V. Ortiz, J. Cioslowski, and D. J. Fox, *Gaussian 09 Revision A.02*, 2009.
- [111] B. J. Lynch, P. L. Fast, M. Harris, and D. G. Truhlar, *J. Phys. Chem. A*, 2000, **104**, 4811.
- [112] T. H. Dunning, *J. Chem. Phys.*, 1989, **90**, 1007.
- [113] C. Peng and H. B. Schlegel, *Isr. J. Chem.*, 1993, **33**, 449.
- [114] C. Peng, P. Y. Ayala, H. B. Schlegel, and M. J. Frisch, *J. Comp. Chem.*, 1996, **17**, 49.
- [115] D. C. Clary, *Mol. Phys.*, 1985, **54**, 605.
- [116] W. Klemperer, K. K. Lehmann, J. K. G. Watson, and S. C. Wofsy, *J. Phys. Chem.*, 1993, **97**, 2413.
- [117] F. Filsinger, K. Wohlfart, M. Schnell, J.-U. Grabow, and J. Küpper, *Phys. Chem. Chem. Phys.*, 2008, **10**, 666.
- [118] T. Matthey, T. Cickovski, S. Hampton, A. Ko, Q. Ma, M. Nyerges, T. Raeder, T. Slabach, and J. A. Izaguirre, *ACM Trans. Math. Softw.*, 2004, **30**, 237.
- [119] M. T. Bell, A. D. Gingell, J. Oldham, T. P. Softley, and S. Willitsch, *Faraday Discuss.*, 2009, **142**, 73.

- [120] J. Küpper, F. Filsinger, and G. Meijer, *Faraday Discuss.*, 2009, **142**, 155.
- [121] J. M. C. Plane, T. Vondrak, S. Broadley, B. Cosic, A. Ermoline, and A. Fontijn, *J. Phys. Chem. A*, 2006, **110**, 7874.
- [122] J. S. Chickos and W. E. Acree, *J. Phys. Chem. Ref. Data*, 2002, **31**, 537.
- [123] D. Clary, *Annu. Rev. Phys. Chem.*, 1990, **41**, 61.
- [124] H. Sabbah, L. Biennier, I. R. Sims, Y. Georgievskii, S. J. Klippenstein, and I. W. M. Smith, *Science*, 2007, **317**, 102.
- [125] A. D. Gingell, M. T. Bell, J. M. Oldham, T. P. Softley, and J. N. Harvey, *J. Chem. Phys.*, 2010, **133**, 194302.
- [126] I. W. M. Smith, A. M. Sage, N. M. Donahue, E. Herbst, and D. Quan, *Faraday Discuss.*, 2006, **133**, 137.
- [127] S. Putzke, F. Filsinger, H. Haak, J. Küpper, and G. Meijer, *Phys. Chem. Chem. Phys.*, 2011, **13**, 18962.
- [128] S. Trippel, Y.-P. Chang, S. Stern, T. Mullins, L. Holmegaard, and J. Küpper, *Phys. Rev. A*, 2012, **86**, 033202.
- [129] S. Y. T. van de Meerakker, H. L. Bethlem, N. Vanhaecke, and G. Meijer, *Chem. Rev.*, 2012, **112**, 4828.
- [130] X. Tong, A. H. Winney, and S. Willitsch, *Phys. Rev. Lett.*, 2010, **105**, 143001.
- [131] X. Tong, D. Wild, and S. Willitsch, *Phys. Rev. A*, 2011, **83**, 023415.
- [132] Y.-P. Chang, K. Dlugolecki, J. Küpper, D. Rösch, D. Wild, and S. Willitsch, *Science*, 2013, **342**, 98.
- [133] D. Rösch, S. Willitsch, Y.-P. Chang, and J. Küpper, *J. Chem. Phys.*, 2014, **140**, 124202.
- [134] S. J. Schowalter, K. Chen, W. G. Rellergert, S. T. Sullivan, and E. R. Hudson, *Rev. Sci. Instrum.*, 2012, **83**, 043103.

BIBLIOGRAPHY

- [135] C. Schneider, S. J. Schowalter, K. Chen, S. T. Sullivan, and E. R. Hudson, *Phys. Rev. Applied*, 2014, **2**, 034013.
- [136] C. Schneider, S. J. Schowalter, P. Yu, and E. R. Hudson, *Int. J. Mass Spectrom.*, 2016, **394**, 1.
- [137] N. Deb, L. L. Pollum, A. D. Smith, M. Keller, C. J. Rennick, B. R. Heazlewood, and T. P. Softley, *Phys. Rev. A*, 2015, **91**, 033408.
- [138] K. A. E. Meyer, L. L. Pollum, L. S. Petralia, A. Tauschinsky, C. J. Rennick, T. P. Softley, and B. R. Heazlewood, *J. Phys. Chem. A*, 2015, **119**, 12449.
- [139] K.-K. Ni, H. Loh, M. Grau, K. C. Cossel, J. Ye, and E. A. Cornell, *J. Mol. Spectrosc.*, 2014, **300**, 12.
- [140] S. Jyothi, T. Ray, and S. A. Rangwala, *Appl. Phys. B*, 2015, **118**, 131.
- [141] C. M. Seck, E. G. Hohenstein, C.-Y. Lien, P. R. Stollenwerk, and B. R. Odom, *J. Mol. Spectrosc.*, 2014, **300**, 108.
- [142] D. Irmia, D. Dobrikov, R. Kortekaas, H. Voet, D. A. van den Ende, W. A. Groen, and M. H. M. Janssen, *Rev. Sci. Instrum.*, 2009, **80**, 113303.
- [143] J. M. C. Plane, T. Vondrak, S. Broadley, B. Cosic, A. Ermoline, and A. Fontijn, *J. Phys. Chem. A*, 2006, **110**, 7874.
- [144] K. G. Spears and F. C. Fehsenfeld, *J. Chem. Phys.*, 1972, **56**, 5698.
- [145] V. V. Lavrov, V. Blagojevic, G. K. Koyanagi, G. Orlova, and D. K. Bohme, *J. Phys. Chem. A*, 2004, **108**, 5610.
- [146] K. Okada, M. Wada, L. Boesten, T. Nakamura, I. Katayama, and S. Ohtani, *J. Phys. B: At. Mol. Opt. Phys.*, 2003, **36**, 33.
- [147] D. Suckau, A. Resemann, M. Schuerenberg, P. Hufnagel, J. Franzen, and A. Holle, *Anal. Bioanal. Chem.*, 2003, **376**, 952.
- [148] Y. Xu, B. Xiong, Y. C. Chang, and C. Y. Ng, *J. Chem. Phys.*, 2012, **137**, 241101.

- [149] Y. C. Chang, H. Xu, Y. Xu, Z. Lu, Y.-H. Chiu, D. J. Levandier, and C. Y. Ng, *J. Chem. Phys.*, 2011, **134**, 201105.
- [150] Y. C. Chang, Y. Xu, Z. Lu, H. Xu, and C. Y. Ng, *J. Chem. Phys.*, 2012, **137**, 104202.
- [151] L. Paetow, F. Unger, W. Beichel, G. Frenking, and K.-M. Weitzel, *J. Chem. Phys.*, 2010, **132**, 174305.
- [152] D. Gerlich and T. Rox, *Z. Phys. D*, 1989, **13**, 259.
- [153] R. J. Green, J. Qian, H.-T. Kim, and S. L. Anderson, *J. Chem. Phys.*, 2000, **113**, 3002.
- [154] T. Uhlemann, J. Wallauer, and K.-M. Weitzel, *Phys. Chem. Chem. Phys.*, 2015, **17**, 16454.
- [155] Y. Xu, B. Xiong, Y. C. Chang, and C. Y. Ng, *J. Chem. Phys.*, 2013, **139**, 024203.
- [156] S. G. Ard, A. Li, J. Oscar Martinez, N. S. Shuman, A. A. Viggiano, and H. Guo, *J. Phys. Chem. A*, 2014, **118**, 11485–11489.
- [157] R. Liu, F. Wang, B. Jiang, G. Czakó, M. Yang, K. Liu, and H. Guo, *J. Chem. Phys.*, 2014, **141**, 074310.
- [158] O. Martinez, S. G. Ard, A. Li, N. S. Shuman, H. Guo, and A. A. Viggiano, *J. Chem. Phys.*, 2015, **143**, 114310.
- [159] D. A. Horke, Y.-P. Chang, K. Długołęcki, and J. Küpper, *Angew. Chem. (int. ed. engl.)*, 2014, **53**, 11965.
- [160] T. Su and M. T. Bowers, *International Journal of Mass Spectrometry and Ion Physics*, 1973, **12**, 347.
- [161] D. Smith, N. G. Adams, and T. M. Miller, *J. Chem. Phys.*, 1978, **69**, 308.
- [162] L. V. Keldysh, *Sov. Phys. JETP*, 1964, **20**, 1307.

BIBLIOGRAPHY

- [163] S. Augst, D. Strickland, D. D. Meyerhofer, S. L. Chin, and J. H. Eberly, *Phys. Rev. Lett.*, 1989, **63**, 2212.
- [164] S. Trippel, T. Mullins, N. L. M. Müller, J. S. Kienitz, J. J. Omiste, H. Stapelfeldt, R. González-Férez, and J. Küpper, *Phys. Rev. A*, 2014, **89**, 051401.
- [165] B. R. Turner and J. A. Rutherford, *J. Geophys. Res.*, 1968, **73**, 6751.
- [166] R. A. Dressler, J. A. Gardner, R. H. Salter, F. J. Wodarczyk, and E. Murad, *J. Chem. Phys.*, 1990, **92**, 1117.
- [167] R. A. Dressler, R. H. Salter, and E. Murad, *J. Chem. Phys.*, 1993, **99**, 1159.
- [168] B. Yuan, Z. Scott, G. Tikhonov, D. Gerlich, and M. A. Smith, *J. Phys. Chem. A*, 2011, **115**, 25.
- [169] O. Diels and K. Alder, *Liebigs Ann. Chem.*, 1928, **460**, 98.
- [170] K. C. Nicolaou, S. A. Snyder, T. Montagnon, and G. Vassilikogiannakis, *Angew. Chem. (int. ed. engl.)*, 2002, **41**, 1668.
- [171] M. N. Eberlin, *Int. J. Mass Spectrom.*, 2004, **235**, 263.
- [172] A. Halasa, L. Lapinski, H. Rostkowska, and M. J. Nowak, *J. Phys. Chem. A*, 2015, **119**, 9262.
- [173] J. L. Hansen, J. J. Omiste, J. H. Nielsen, D. Pentlehner, J. Küpper, R. González-Férez, and H. Stapelfeldt, *J. Chem. Phys.*, 2013, **139**, 234313.

Daniel Rösch

Date of birth 1. January 1986
Adress Department of Chemistry
University of Basel
Klingelbergstrasse 80
4056 Basel
e-Mail daniel.roesch@unibas.ch

Education

- 2006 **Abitur**, *Ernährungswissenschaftliches Gymnasium Lörrach*, Germany.
2006–2009 **B.Sc. in Chemistry**, *University of Basel*, Switzerland.
2009–2011 **M.Sc. in Chemistry**, *University of Basel*, Switzerland.
Thesis title: New ligands for functionalization of TiO₂ nano particles using click reactions
Supervisor: Prof. Dr. Edwin C. Constable and Prof. Dr. Catherine E. Housecroft
2011–2016 **PhD in Chemistry**, *University of Basel*, Switzerland.
Thesis title: Reactive collisions with conformationally controlled molecules
Supervisor: Prof. Dr. Stefan Willitsch
currently **Postdoc in the group of Prof. Dr. Stefan Willitsch**, *University of Basel*, Switzerland.

Publications

- Y.-P. Chang*, K. Dlugolecki, J. Küpper, D. Rösch*, D. Wild and S. Willitsch, Specific Chemical Reactivities of Spatially Separated 3-Aminophenol Conformers with Ca⁺ Ions.
* These authors contributed equally to this work.
Science, **342**, 98 (2013)
- D. Rösch, S. Willitsch, Y.-P. Chang and J. Küpper, Chemical reactions of conformationally selected 3-aminophenol molecules in a beam with Coulomb-crystallized Ca⁺ ions.
J. Chem. Phys., **140**, 124202 (2014)
- D. Rösch, H. Gao, A. Kilaj and S. Willitsch, Design and characterization of a linear quadrupole ion trap for high-resolution Coulomb-crystal time-of-flight mass spectrometry.
EPJ Tech. Instr., **3:5**, (2016)

Experience

- Technical:
 - Designing and building experimental apparatuses
 - Ultra-high vacuum technology
 - Molecular beam techniques
 - Laser and optics laboratory techniques
 - Mass spectrometry
 - Ion trapping and laser cooling
- Programming and data analysis:
 - Labview
 - Python
 - Matlab
 - Fortran
- Teaching:
 - Teaching assistant in undergraduate and graduate physical chemistry courses (2012 - 2015)
 - Successfully supervised the research work of one Master student and one project student

Attended Conferences

- Attended Science & Ski Seminar, Diavolezza, Switzerland, 2012
- Poster MOLEC 2012, Oxford, U.K., 2012
- Poster Dynamics of Molecular Collisions, Granlibakken, USA, 2013
- Poster & 2. IOTA Workshop on Cold Molecular Ions, Arosa, Switzerland, 2013
Talk
- Talk PCC Samichlaus Symposium, Basel, Switzerland, 2013
- Poster MOLEC 2014, Gothenburg, Sweden, 2014
- Poster 594. WE-Heraeus-Seminar, Bad Honnef, Germany, 2015
- Poster SASP 2016, Davos, Switzerland, 2016
- Poster ECAMP 12, Frankfurt, Germany, 2016

Languages

- German Mother tongue
- English Fluent
- French Basic knowledge